Near Surface Dynamics of Cross-Linked and Non-Cross-Linked Polymer Architectures at Solid Planar Surfaces

vorgelegt von
M. Sc.
Judith Witte
ORCID: 0000-0003-4780-8675

von der Fakultat II - Mathematik und Naturwissenschaften
der Technischen Universität Berlin
zur Erlangung des akademischen Grades

Doktor der Naturwissenschaften
Dr. rer. nat.

genehmigte Dissertation

Promotionsausschuss:

Vorsitzender: Prof. Dr. Reinhard Schomäcker
Gutachter: Prof. Dr. Michael Gradzielski
Gutachterin: Prof. Dr. Regine von Klitzing

Tag der wissenschaftlichen Aussprache: 15. Juni 2021

Berlin 2021

Acknowledgments

During the creation of this thesis I have received support and assistance from many sides.
First, I thank Dr. Stefan Wellert for providing the topic of this thesis and introducing me to the world of neutron scattering. Thank you for opportunities to travel to conferences and research facilities around the world. To Dr. Olaf Holderer and Dr. Tetyana Kyrey, thank you for the productive collaboration on our joint DFG project.
Special thanks go to Prof. Dr. Michael Gradzielski and Prof. Dr. Regine von Klitzing for the scientific evaluation of this thesis.
In terms of laboratory work, I thank my students Margarethe Dahl and Patrick Krause. Furthermore, thanks to Jana Lutzki who was very helpful in all practical matters.
I further extend thanks to the AK von Klitzing at the TU Darmstadt and especially Matthias Kühnhammer and Marcus U. Witt.
Thank you, Dr. Maren Lehmann and Christoph Brückner, for the fun times in our office and all your scientific advice.
I thank Prof. Dr. Jörg Lahann for the research semester in his laboratory at the University of Michigan. Thanks to Dr. Stephanie Christau for the collaboration in the laboratory. It was a lot of fun "baking" zwitterionic brushes with insane amounts of monomer. Thanks go to all members of the Lahann Lab, especially Dr. Ramya Kumar and Jonathan Gerszberg for their advice on PMEDSAH. Ava Mauser, Nahal Habibi and Laura Saunders, thank you for making my stay a lot of fun! Go blue!
To all instrument responsibles at neutron research facilities around the globe, and especially Dr. Judith Houston, Dr. Alexandros Koutsioubas, Dr. Egor Vezhlev, Dr. Laura Stingaciu, Dr. Piotr Zolnierczuk, Dr. Samantha Micciulla, Dr. Luca Silvi and Dr. Mariano Paulin; thank you for your support.
Furthermore, to Dr. Bernhard V. K. J. Schmidt and Marlies Gräwert, thank you for your support with SEC measurements at the Max Planck Institute of Colloids and Interfaces. To Dr. Maria Schlangen and Marc Griffel thank you for LC-MS measurements and advice on their analysis.
Finally, I want to thank people outside of academia. My parents, Petra Witte and Manfred Kirschner, for their support throughout my studies, and my grandparents, Roswitha and Manfred Plath. Last, but not least, I would like to thank Marvin Klaiber, who held be accountable in our weekly accountability partner meetings and who constantly motivated and encouraged me.

Abstract

The aim of this dissertation was the investigation of the interplay of the inner structure and dynamics of differently cross-linked soft matter systems (microgels, polymer brushes). The thesis focuses on the influence of a solid, planar interface on the dynamics of those systems. First, the influence of the polymerization method (batch vs. continuous monomer feed) and the cross-linker content on the swelling of Poly(*N*-isopropylacrylamide) (PNIPAM)-based microgels was studied with dynamic light scattering (DLS). Moreover, adsorbed microgel particles were imaged with atomic force microscopy (AFM) to identify a suitable system for further neutron scattering experiments. Hence, the inner structure of highly cross-linked PNIPAM microgels (10 mol% cross-linker) was investigated with small angle neutron scattering (SANS). The inner dynamics was investigated with neutron spin echo spectroscopy (NSE) in transmission mode and the collective and Zimm-type diffusion constants of the chain segments were determined on different lengths. The inner dynamics of adsorbed microgel particles was investigated with NSE under grazing incidence (GINSES). This method generates an evanescent field and by variation of the angle of incidence the investigated thickness can be varied. It was shown that the inner dynamics of feeding-microgels was highly suppressed in proximity to the solid-liquid interface. Additional nanoindentation measurements showed the relation of this fact to the soft nature of those particles. In contrast, the inner dynamics of the conventional batch microgel was not influenced by the interface. Furthermore, PNIPAM-based polymer brushes were synthesized by surface-initiated atom transfer radical polymerization (SI ATRP). The polymer volume profile was determined with neutron reflectometry (NR) and resulted in a parabolic brush profile. GINSES measurements showed that the dynamics varies over the brush height. The calculated correlation lengths indicate that the excluded volume increases with increasing distance to the interface. This is explained by the increased flexibility of the chains with increasing distance from the interface. In general, the results are interesting for the design of soft matter systems, e.g. in functional coatings.

Zusammenfassung

Das Ziel der vorliegenden Dissertation war die Untersuchung des Zusammenspiels von innerer Struktur und Dynamik in verschiedentlich quervernetzten Systemen weicher Materie (Mikrogele, Polymerbürsten). Der Hauptfokus lag hierbei auf dem Einfluss einer festen, planen Grenzfläche auf die Dynamik solcher Systeme. Zunächst wurde der Einfluss der Polymerisationsmethode (Batch vs. Kontinuierliche Methode) und dem eingesetzten Gehalt an Quervernetzer auf das Schwellverhalten von Poly(*N*-isopropylacrylamid) (PNIPAM)-basierten Mikrogelen mittels Dynamischer Lichtstreuung (DLS) untersucht. Des Weiteren wurden die adsorbierten Mikrogelpartikel mittels Rasterkraftmikroskopie (AFM) untersucht, um ein geeignetes System zur weiteren Untersuchung mittels Neutronenstreumethoden zu ermitteln. Daraus folgend wurde die innere Struktur hochquervernetzter PNIPAM-Mikrogele (10 mol% Quervernetzer) aus Batch- und kontinuierlicher Polymerisation mittels Neutronenkleinwinkelstreuung (SANS) untersucht. Weiterhin wurde die innere Dynamik mittels Neutronenspinecho-Spektroskopie (NSE) in Transmission über einen weiten Längenbereich untersucht. Hieraus konnten kollektive Diffusionskonstanten, sowie die Diffusionskonstante der Zimm-artigen Dynamik der Kettensegmente bestimmt werden. Die Dynamik im Inneren der adsorbierten PNIPAM-Mikrogelpartikel wurde mittels NSE unter streifendem Einfall (GINSES) untersucht. Diese Methode erzeugt ein evaneszentes Feld, und erlaubt durch Variation des Einfallwinkels die Einstellung der untersuchten Schichtdicke. Hierbei zeigte sich, dass die Dynamik der Mikrogele aus dem kontinuierlichen Prozess in Nähe der Grenzfläche stark gehemmt ist. Durch ergänzende Nanoindentationsmessungen konnte dies in Zusammenhang mit der weichen Natur dieser Mikrogele gebracht werden. Im Gegensatz hierzu wurde die Dynamik der klassischen Batch Mikrogele kaum durch die Grenzfläche beeinflusst. Im Weiteren wurden PNIPAM-basierte Polymerbürsten unterschiedlicher Ankerdichten durch oberflächen-initiierte radikalische Atomtransfer Polymerisation (SI ATRP) erzeugt. Das Polymervolumenprofil der Polymerbürsten wurde mittels Neutronenreflektometrie (NR) ermittelt und ergab ein parabolisches Bürstenprofil. GINSES Messungen zeigten, dass die Dynamik über die Dicke der Polymerbürste variiert. Die hieraus berechneten Korrelationslängen zeigen, dass das „excluded volume“ mit Abstand zur Grenzfläche größer wird. Dies wurde mit der veränderten Beweglichkeit der Ketten über die Polymerbürstendicke erklärt. Insgesamt ergeben sich aus den Experimenten interessante Anhaltspunkte für das Design von Systemen weicher Materie an Grenzflächen, welche für funktionelle Beschichtungen eine wichtige Rolle spielen.

Publications authored during the PhD:

- Witte, J.; Kyrey, T.; Lutzki, J.; Dahl, A. M.; Kühnhammer, M.; von Klitzing, R.; Holderer, O. and Wellert, S. Looking Inside Poly(*N*-isopropylacrylamide) Microgels: Nanomechanics and Dynamics at Solid-Liquid Interfaces. *ACS Applied Polymer Materials,* **2021,** *3,* 976-985.

- Witte, J.; Krause, P.; Kyrey, T.; Dahl, A. M.; Lutzki, J.; Schmidt, B. V. K. J.; Ganeva, M.; Koutsioubas, A.; Holderer, O. and Wellert, S. Grazing Incidence Neutron Spin Echo Study of Poly(*N*-isopropylacrylamide) Brushes. *Macromolecules,* **2020,** *53,* 1819-1830.

- Witte, J.; Kyrey, T.; Lutzki, J.; Dahl, A. M.; Houston, J.; Radulescu, A.; Pipich, V.; Stingaciu, L.; Kühnhammer, M.; Witt, M. U.; von Klitzing, R.; Holderer, O. and Wellert, S. A Comparison of the Network Structure of Homogeneously and Heterogeneously Crosslinked PNIPAM Microgels with High Crosslinker Content. *Soft Matter,* **2019,** *15,* 1053-1064.

Co-authored publications:

- Kyrey, T.; Ganeva, M.; Witte, J.; von Klitzing, R.; Wellert, S. and Holderer, O. Understanding Near-Surface Polymer Dynamics by a Combination of Grazing-Incidence Neutron Scattering and Virtual Experiments. *Journal of Applied Crystallography,* **2021,** *54,* 72-79.

- Kyrey, T.; Witte, J.; Feoktystov, A.; Pipich, V.; Wu, B.; Pasini, S.; Radulescu, A.; Witt, M. U.; Kruteva, M.; von Klitzing, R.; Wellert, S. and Holderer, O. Inner Structure and Dynamics of Microgels with Low and Medium Crosslinker Content Prepared *via* Surfactant-Free Precipitation Polymerization and Continuous Monomer Feeding Approach. *Soft Matter,* **2019,** *15,* 6536-6546.

- Kyrey, T.; Witte, J.; Pipich, V.; Feoktystov, A.; Koutsioubas, A.; Vezhlev, E.; Frielingshaus, H.; von Klitzing, R.; Wellert, S. and Holderer, O. Influence of the Cross-Linker Content on Adsorbed Functionalized Microgel Coatings. *Polymer,* **2019,** *169,* 29-35.

- Kyrey, T.; Ganeva, M.; Gawlitza, K.; Witte, J.; von Klitzing, R.; Soltwedel, O.; Di, Z.; Wellert, S. and Holderer, O. Grazing Incidence SANS and Reflectometry Combined with Simulation of Adsorbed Microgel Particles. *Physica B: Condensed Matter,* **2018,** *551,* 172-178.

- Kyrey, T.; Witte, J.; Gvaramia, M.; Wellert, S.; Koutsioubas, A.; Mattauch, S.; Holderer, O. and Frielinghaus, H. Simpler Neutron Resonator Enhances the Wave Field for Grazing Incidence Scattering Experiments with Lower Parasitic Scattering. *Physica B: Condensed Matter,* **2018,** *551,* 405-406.

Contents

List of Abbreviations

AAPH 2,2'-azobis(2-methylpropionamidine) dihydrochloride

AFM Atomic Force Microscopy

APCI Atmospheric Pressure Chemical Ionization

ATRP Atom Transfer Radical Polymerization

BIS *N,N'*-methylenebisacrylamide

CB Citizens Band

CCSS Collapsed Core Swollen Shell

CRP Controlled Radical Polymerization

DLS Dynamic Light Scattering

dSTORM direct Stochastic Optical Reconstruction Microscopy

DWS Diffusing Wave Spectroscopy

eBMPUS [11-(2-Bromo-2-methyl)propionyloxy]undecyltrichlorosilane

ELS Electrophoretic Light Scattering

EW DLS Evanescent Wave Dynamic Light Scattering

GC Gas Chromatography

GINSES Grazing Incidence Neutron Spin Echo Spectroscopy

IENS Incoherent Elastic Neutron Scattering

ISF Intermediate Scattering Function

IQNS Incoherent Quasi-elastic Scattering

JCNS Jülich Centre for Neutron Science

KF Karl Fischer

LC-MS Liquid Chromatography Mass Spectrometry

LCST Lower Critical Solution Temperature

MLZ Maier-Leibnitz Zentrum

MNP Magnetic Nanoparticle

MWCO Molecular Weight Cut-Off

NIPAM *N*-isopropylacrylamide

NMP Nitroxide-mediated Polymerization

NR Neutron Reflectometry

NSE Neutron Spin Echo Spectroscopy

OEGMA Oligoethylene glycol methacrylate

OSB Oversaturated Brush Regime

PCSA Polerizer Compensator Sample Analyzer

PDEAAM Poly(*N,N*-diethylacrylamide)

PDI Polydispersity Index

PEG Polyethylene glycol

PEO-PS Polyethylene oxide-Polystyrene

PMDETA *N,N;N',N",N"*-pentamethyldiethylenetriamine

PNIPAM Poly(*N*-isopropylacrylamide)

PTFE Polytetrafluorethylene

RAFT Reversible Addition-fragmentation Chain Transfer Polymerization

SAM Self-assembled Monolayer

SANS Small Angle Neutron Scattering

SCCS Swollen Core Collapsed Shell

SEC Size Exclusion Chromatography

SEM Scanning Electron Microscopy

SI ATRP Surface-initiated Atom Transfer Radical Polymerization

SLD Scattering Length Density

STM Scanning Tunneling Microscopy

TBAF Tetrabutylammonium fluoride

TEM Tranmission Electron Microscopy

THF Tetrahydrofuran

THQ Toluhydroquinone

UCST Upper Critical Solution Temperature

USANS Ultra Small Angle Neutron Scattering

VPT Volume Phase Transition

VPTT Volume Phase Transition Temperature

XPCS X-ray Photon Correlation Spectroscopy

List of Figures

List of Tables

1. Introduction

Polymeric materials have become indispensable in modern life. Their advent in the mid-19th century with the production of products based on cellulose and casein was followed by a steady development and extensive research throughout the 20th century. Mainly, this was due to their advantages to other materials such as low weight, reduced stiffness, corrosion resistance and improved processability.
The growing interest in micro- and nanomaterials sparked a lot of research and technological advances in the field. Among others the development of analytical instruments to resolve small structures such as the invention of the atomic force microscope (AFM) by Binning and Rohrer in 1986 were a direct result. Furthermore, new fields such as nanomedicine, nano-pharmaceuticals and nano-oncology were created.
The field of soft condensed matter subsumes multiple systems with unique properties such as liquid crystals, colloids, foams, suspensions and polymers. Those systems possess a low elastic modulus and are organized "on a mesoscopic scale into entities much larger than an atom, but much smaller than the overall size of the material."[1] Therefore, the field includes polymeric materials with dimensions in the micro- and nano-range. Soft matter can be used in surface coatings to alter the surface properties of materials, e.g. wettability, fouling, proneness to corrosion, or even to make surfaces icephobic. The constant development of new soft matter systems calls for experimental and computer-based methods to further their fundamental understanding.
In this thesis, *N*-isopropylacrylamide (NIPAM)-based soft matter systems (Figure 1.1) were investigated, specifically in the context of surface coatings. The focus lays on the relationship of structure and dynamics in systems below the volume phase transition temperature. Here, NIPAM serves as a suitable model system for an uncharged polymer. In the literature studies on NIPAM-based macro- and microgels and polymer brushes have already sparked wide interest. This interest is in part due to the responsive character of NIPAM with a lower critical solution temperature of approximately 32 °C. Soft matter systems based on the polymer NIPAM retain this property.
Chapters 4 and 5 deal with microgels based on NIPAM. Microgels are colloidal particles with typical diameters between 100 nm and 1 μm. Their gel network is suited to load a cargo and hence stimuli responsive microgels are discussed in the context of (drug) delivery applications.

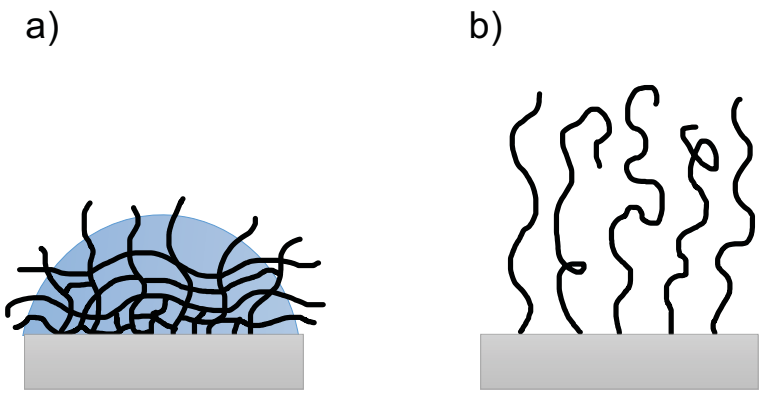

Figure 1.1.: Scheme of cross-linked and non-cross-linked polymer architectures at solid planar surfaces. a) adsorbed microgel particle and b) polymer brush.

Chapter 4 is inspired by the development of continuous methods for the preparation of NIPAM-based microgels. Within the field, it is a well-known fact that the preparation by a batch method leads to PNIPAM microgel particles with an inhomogeneous internal structure. Hence, in Chapter 4 PNIPAM microgels with varying amounts of cross-linker were prepared by a batch and a continuous method. Their optical properties and swelling behavior in water are compared. Further, adsorbed microgel particles are studied with the AFM to characterize their surface structure and their ability to reswell in water after adsorption.
In Chapter 5 the internal structure and internal dynamics of highly cross-linked PNIPAM batch- and feeding-microgels (10 mol% cross-linker) are investigated in more detail. First, in bulk (SANS, NSE) and later in the adsorbed state (AFM, GINSES). In bulk the correlation length in the polymer network, the fuzziness parameter and the collective diffusion coefficient are compared for both types. In the adsorbed state, fast force mapping on the AFM is used to determine the lateral distribution of the elastic modulus of individual microgel particles. Afterwards, monolayers of PNIPAM microgels on flat silicon substrates are investigated with neutron spin echo spectroscopy under grazing incidence (GINSES). GINSES is a relatively young technique and has not been used extensively in the study of adsorbed soft matter samples. The method enables the resolution of dynamics perpendicular to the interface. Therefore, the collective diffusion coefficient in near-surface layers and averaged over the entire particle could be measured and compared. This allows the estimation of the influence of the interface on the dynamics of a soft matter sample.

In Chapter 6 polymer brushes based on NIPAM were investigated. Polymer brushes are an example of a non-crosslinked soft matter system. The structure of a polymer brush can be tuned by the variation of the grafting density. Here, care must be taken to remain within the brush regime of grafted polymers (other regimes are the mushroom and pancake regime). The grafting density was experimentally determined by degrafting of the polymer brush and subsequent size exclusion chromatography. It is discussed which pitfalls this technique entails. Furthermore, polymer volume fraction profiles were measured with neutron reflectometry (NR) and the brush structure in relation to the grafting density was discussed. Finally, GINSES was applied to PNIPAM brushes with differing grafting densities. This study allows a comparison of the correlation length (related to the blob size) in near-surface layers and the correlation length averaged over the entire brush. Further, the influence of the grafting density on the correlation length is shown.

In summary, this thesis presents GINSES as a valuable addition to the toolbox for the investigation of soft matter coatings. GINSES helps to understand the influence of a solid planar surface on the system's dynamics in near-surface layers on small time and length scales, hardly accessible with other methods.

2. Scientific Background

This chapter provides an overview of the scientific background relevant for this thesis. The investigated systems, namely microgel particles and neutral polymer brushes, are based on polymer chains. Therefore, common concepts for the description of ideal and real polymer chains are introduced. A brief discussion of the synthesis and structure of microgel particles and polymer brushes follows. The chapter is concluded with an introduction of the basic principles of neutron scattering.

2.1. Ideal and Real Polymer Chains

Ideal chains The following section introduces the most important concepts used for the description of ideal polymer chains. This facilitates the understanding of the subsequent descriptions of the freely jointed and equivalent freely jointed chain model. The description of ideal chains neglects interactions between monomers that are separated by many bonds along the polymer chain.

Polymers are flexible chains consisting of a sequence of monomer units. Their flexibility results from the variation of torsion angles along the chain. In Figure 2.1a the carbon atoms C_{i-2}, C_{i-1} and C_i span a plane. The bonds between the carbon atoms are described by the bond vectors $\vec{r}_{i-1}$, $\vec{r}_i$ and $\vec{r}_{i+1}$. The bond vector $\vec{r}_i$ is the axis of rotation for $\vec{r}_{i+1}$. As $\vec{r}_{i+1}$ rotates along $\vec{r}_i$ the torsion angle φ varies between 0 and 360°. If φ equals 0, $\vec{r}_{i-1}$ and $\vec{r}_{i+1}$ are colinear. This is called the *trans* conformation. In Figure 2.1b the energy is displayed against the torsion angle φ. It is shown that the energy changes with the variation of the distance between the CH_2 groups bonded to C_{i+1} and C_i. The *trans* conformation is the state with the lowest energy. Another low energy state is the so-called *gauche* conformation. The *gauche* conformation is assumed at φ = + 120° ($gauche_+$) and φ = - 120° ($gauche_-$). The magnitude of the energy difference between the *trans* and *gauche* state $\Delta\epsilon$ determines the probability of finding a *gauge* state in thermal equilibrium. The two *gauge* states and the *trans* state are separated by the energy barrier ΔE. This energy barrier determines the dynamics of conformational rearrangement.

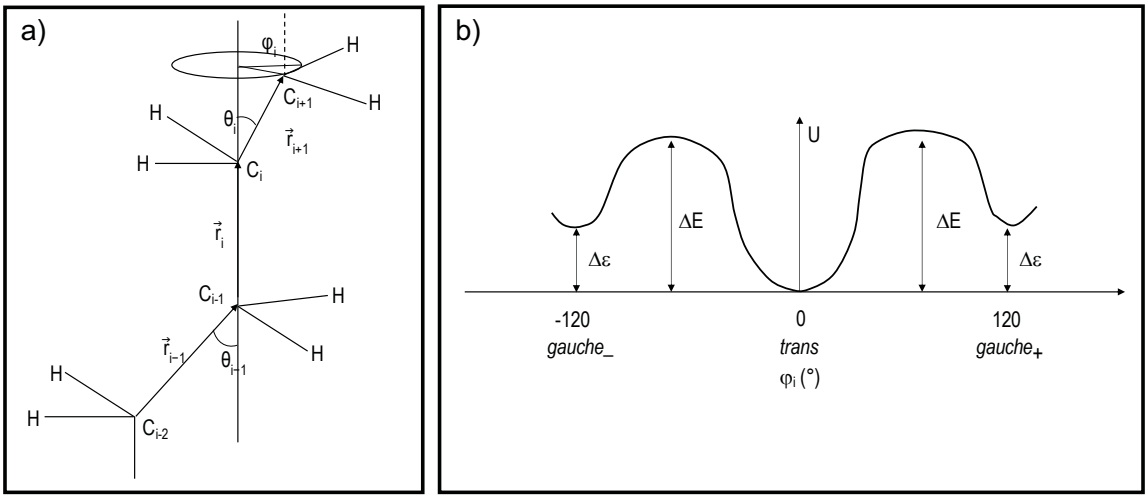

Figure 2.1.: Torsion angle φ_i in a polymer. The energy depends on the torsion angle. Reproduced from Ref. 2.

The **contour length** R_{max} of a polymer chain is the largest end-to-end distance which would result if all torsion angles within a chain were in the *trans* state. It is defined as

$$R_{max} = nlcos\frac{\theta}{2}, \tag{2.1}$$

with n the number of skeleton bonds and $lcos(\theta/2)$ their projected length along the contour. After a number of consecutive *trans* states (rod-like section) a gauge state breaks up the rod-like all-*trans* zig zag. Therefore, on small length scales the chain is rod-like, but on longer length scales flexible.

The **end-to-end vector** of an ideal chain with n+1 atoms is defined as

$$\vec{R_n} = \sum \vec{r_i} \tag{2.2}$$

and in an isotropic collection of chains with n backbone atoms the ensemble average of the end-to-end vector is

$$\langle \vec{R_n} \rangle = 0. \tag{2.3}$$

A simple model for the description of ideal chains is the **freely jointed chain model**. It assumes a constant bond length $l = |\vec{r_i}|$ and neglects correlations between the direction

of different bond vectors. Therefore, $\langle \cos\theta_{ij} \rangle = 0$ for $i \neq j$ and $\cos\theta_{ij} = 1$ for $i = j$. This means that there are exactly n non-zero terms and the mean square end-to-end distance is

$$\langle R^2 \rangle = nl^2. \tag{2.4}$$

The sum over all other bond vectors j for one bond vector i converges to a finite number C_i, which is defined by

$$C_i' \equiv \sum cos\theta_{ij} \tag{2.5}$$

and yields the mean-square end-to-end distance

$$\langle R^2 \rangle = l^2 \sum \sum \langle cos\theta_{ij} \rangle = l^2 \sum C_i' = C_n n l^2. \tag{2.6}$$

C_n is Flory's characteristic ratio, which is characteristic for each polymer. This ratio always has a value larger than 1 and approaches a value C_∞ for long chains.

The **equivalent freely jointed chain model** describes a polymer chain as N freely-joined effective bonds with a length b, called the Kuhn length. N is also called the **degree of polymerization**.
In the framework of this model the contour length is defined as

$$R_{max} = Nb \tag{2.7}$$

and the mean-square end-to-end distance as

$$\langle R^2 \rangle = Nb^2 = bR_{max} = C_\infty n l^2, \tag{2.8}$$

from which follows

$$N = \frac{R_{max}^2}{C_\infty n l^2}; \qquad b = \frac{\langle R^2 \rangle}{R_{max}} = \frac{C_\infty n l^2}{R_m ax}. \tag{2.9}$$

The root-mean-square end-to-end distance is defined as

$$R_0 = \sqrt{\langle R^2 \rangle} = bN^{1/2}, \tag{2.10}$$

where the index 0 refers to the ideal chain.

Examples for more complex models that describe ideal chains are the freely rotating chain model, the worm-like chain model (often called Kratky-Porod model), the hindered rotation model and the rotational isomeric state model. An in depth description of these models exceeds the scope of this thesis, but can be found elsewhere.[2]

The **radius of gyration** R_g is another convenient parameter to describe the dimension of an ideal polymer chain. It is especially useful to describe the dimension of a polymer chain with a non-linear architecture. For example in the case of branched polymers the end-to-end distance is not suited to describe the polymer dimension.

The square radius of gyration is

$$R_g^2 \equiv \frac{1}{N} \sum (\vec{R}_i - \vec{R_{cm}})^2, \tag{2.11}$$

where $\vec{R}_i$ is the position vector of a monomer i and $\vec{R}_{cm}$ the position vector of the center of mass of the polymer. After substituting $\vec{R}_{cm}$ and considering that for fluctuating objects, such as polymers, the ensemble average of all allowed conformations has to be considered, we obtain

$$\langle R^2 \rangle = \frac{1}{N} \sum \sum \langle (\vec{R}_i - \vec{R}_j)^2 \rangle. \tag{2.12}$$

Real chains In contrast to ideal chains, the description of reals chains takes into consideration the interactions between monomers that are separated by many bonds along the contour length. This is important, because in 3-dimensional space, for long chains the probability of monomer-monomer contacts is large.[2]
The effective interaction between a pair of monomers results from the difference between the monomer's direct interaction with another monomer and with other surrounding molecules (e.g. solvent molecules). Two phenomena that need to be considered in this context are the **excluded volume** and **self-avoiding walks**.

In order to explain the excluded volume, a description of the **Mayer f-function** is necessary. The Mayer f-function is the difference between the Boltzmann-factor for two monomers at a distance r and that for the case of no interaction (the Boltzmann-factor equals 1 at infinite distances).

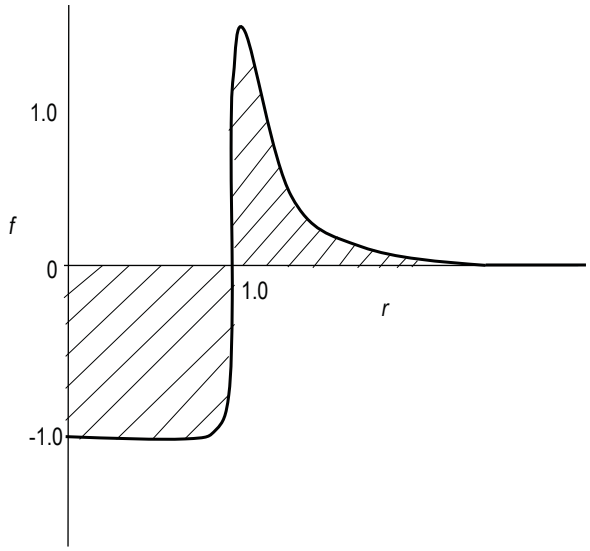

Figure 2.2.: Mayer f-function. Lines represent the integration of the Mayer f-function to determine the excluded volume.

$$f(r) = exp[-U(r)/(kT)] - 1 \tag{2.13}$$

with $U(r)$ the potential at the distance r and kT the thermal energy.

Figure 2.2 shows that the Mayer f-function has negative values at short distances, because the probability of finding monomers at that distance from each other is reduced due to hard core repulsion. However, in the attractive well of the potential between two monomers, the Mayer f-function is positive and the probability of finding monomers is increased.

The excluded volume v is the minus integral of the Mayer f-function over the whole space:

$$v = -\int f(r) d^3r = \int (1 - exp[-U(r)/(kT)]) d^3r \tag{2.14}$$

The excluded volume summarizes the net two-body interactions between monomers. An excluded volume $v > 0$ describes net attraction, while $v < 0$ means net repulsion.

It is important to note that the description above is only valid for spherical monomers. Most monomers, however, are better described as cylinders with a Kuhn length b and a

smaller radius d. The aspect ratio of most flexible polymers is $2 < b/d < 3$, with larger values for stiffer polymers. Depending on the solvent the excluded volume varies and is $0 < v < b^2 d$ in a good solvent.

To describe the conformation of a real chain in a good solvent the **Flory theory** takes into consideration the balance between the effective repulsion between monomers, which swells the chain, and the entropy loss due to that deformation. The theory makes a rough estimate of the energetic and entropic contributions to the free energy of the chain.

It considers a chain with N monomers that is swollen to $R > R_0 = bN^{1/2}$. The monomers are uniformly distributed within the volume R^3 with no correlations between them. The probability to find a second monomer within the excluded volume of another monomer is $(vN)/R^3$ and the energetic cost of being excluded is kT per exclusion or $kTvN/R^3$ per monomer. For all N monomers we obtain the energy of the excluded volume interaction as

$$F_{int} \approx kTv\frac{N^2}{R^3}. \tag{2.15}$$

The entropic contribution to the free energy is the energy required to stretch an ideal chain to its end-to-end distance

$$F_{ent} \approx kT\frac{R^2}{Nb^2}. \tag{2.16}$$

The total free energy of the chain is the sum of the energetic and entropic contribution

$$F = F_{int} + F_{ent} \approx kT\left(v\frac{N^2}{R^3} + \frac{R^2}{Nb^2}\right). \tag{2.17}$$

The optimum size of a real chain R_F, called the Flory radius, can be calculated by assuming $\delta F/\delta R = 0$, which yields

$$R_F = \nu^{1/5} b^{2/5} N^{3/5}. \tag{2.18}$$

The swelling ratio shows that long real chains are larger in size than ideal chains with the same number of monomers:

$$\frac{R_F}{bN^{1/2}} \approx (\frac{\nu}{b^3}N^{1/2})^{1/5}. \tag{2.19}$$

However, excluded volume interactions only swell a chain when the chain interaction

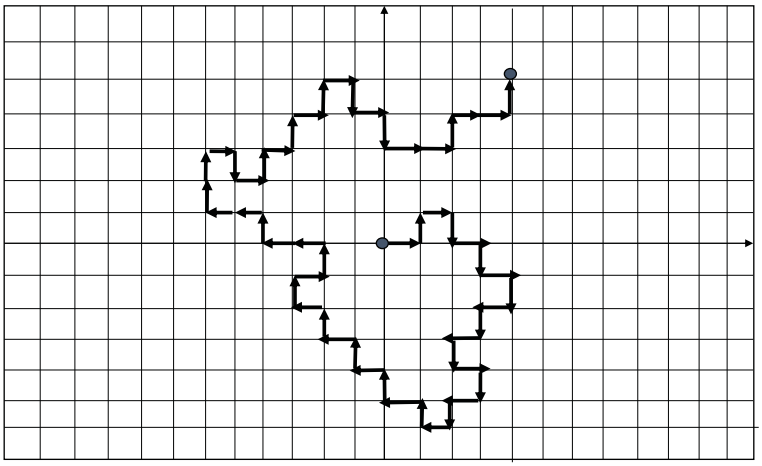

Figure 2.3.: Self-avoiding walk of a real chain on a 2-dimensional lattice.[2]

parameter z is sufficiently large:

$$z \equiv \left(\frac{3}{2\pi}\right)^{3/2} \frac{v}{b^3} N^{1/2} \approx \frac{F_{int}(R_0)}{kT} \approx v\frac{N^2}{R_0^3} \approx \frac{v}{b^3} N^{1/2} \tag{2.20}$$

Although the Flory theory is criticized for overestimating the interaction energy and the elastic energy, it offers predictions that agree well with experiments and other more elaborate theories. The Flory theory leads to a universal power law, in which the polymer size R depends on the number of monomers N according to

$$R \sim N^{\nu}, \tag{2.21}$$

with the exponent ν being $3/5$ for a swollen linear polymer and $1/2$ for an ideal linear chain.

Furthermore, real chains display a self-avoiding walk, which can be described as a random walk on a lattice that never visits the same site more than once. This is illustrated in Figure 2.3.

2.2. Thermodynamics of Mixing

2.2.1. Flory-Huggins Theory

The Flory-Huggins theory describes the thermodynamics of mixing. A polymer solution in a good solvent can be considered a homogeneous mixture, since it is uniform and all components of the mixture are intermixed on a molecular scale.

First, we will look at the entropy of binary mixing. If we consider the species A and B with volumes V_A and V_B, the mixture volume will be assumed as $V_A + V_B$ (s. Figure 2.4) and the volume fractions of the components are

$$\phi_A = \frac{V_A}{V_A + V_B} \tag{2.22}$$

and

$$\phi_B = \frac{V_B}{V_A + V_B}. \tag{2.23}$$

For polymer solutions, with A the polymer chains and B the solvent molecules, the lattice site volume v_0 is determined by the smaller units, namely the solvent molecules. The polymer occupies multiple connected lattice sites and the molecular volumes are

$$v_A = N_A v_0; \qquad v_B = N_B v_0, \tag{2.24}$$

with N_i the number of lattice sites occupied by the species.
The number of lattice sites in the system is

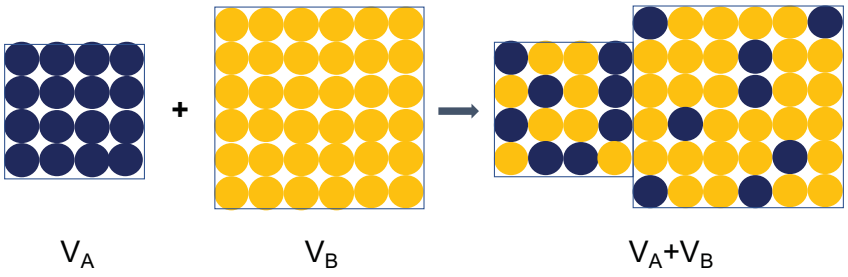

Figure 2.4.: The mixing of two species does not result in a volume change.[2]

$$n = \frac{V_A + V_B}{v_0}, \tag{2.25}$$

where species A occupies

$$\frac{V_A}{v_0} = n\phi_A \tag{2.26}$$

lattice sites, and species B

$$\frac{V_B}{v_0} = n\phi_B. \tag{2.27}$$

The entropy of the system is

$$S = kln\Omega, \tag{2.28}$$

with k the Boltzmann constant and Ω the number of ways in which the molecules can be arranged on the lattice.

Before mixing $\Omega_A = n\phi_A$. The change of entropy for a single molecule upon mixing is

$$\Delta S_A = kln\Omega_{AB} - kln\Omega_A = kln\left(\frac{\Omega_{AB}}{\Omega_A}\right) = kln\left(\frac{1}{\Omega_A}\right) = -kln\phi_A. \tag{2.29}$$

As ϕ_A is always larger than 1, the entropy change of mixing is always positive and therefore promotes mixing.

The total entropy change of mixing is a sum of the entropy contributions of each molecule in the system

$$\Delta S_{mix} = n_A\Delta S_A + n_B\Delta S_B = -k(n_A ln\phi_A + n_B ln\phi_B). \tag{2.30}$$

There are $n_A = n\phi_A/N_A$ molecules of species A and $n_B = n\phi_B/N_B$ molecules of species B in the mixture. The entropy of mixing per lattice site $\Delta S_{mix} = \Delta S_{mix}/n$ is an intrinsic thermodynamic quantity

$$\Delta S_{mix} = -k\left[\frac{\phi_A}{N_A} ln\phi_A + \frac{\phi_B}{N_B} ln\phi_B\right]. \tag{2.31}$$

For a polymer solution $N_A = N$ for the polymer and $N_B = 1$ for the solvent. Therefore, the equation becomes

$$\Delta S_{mix} = -k\left[\frac{\phi_A}{N} ln\phi_A + \phi_B ln\phi_B\right]. \tag{2.32}$$

For polymer solutions the entropy of mixing is lower than for regular solutions, but it always remains positive.

In addition to the entropic contribution, we need to consider the energetic contribution to the thermodynamics of mixing. The **Flory interaction parameter** χ characterizes the difference of interaction energies in the mixture

$$\chi \equiv \frac{z}{2}\left(\frac{2u_{AB} - u_{AA} - uBB}{kT}\right) \tag{2.33}$$

where u is the pairwise interaction energy and z the coordination number in the lattice ($z = 4$ for a square lattice, and $z = 6$ for a cubic lattice).

The energy of mixing per lattice site is

$$\Delta U_{mix} = \chi\phi(1-\phi)kT, \tag{2.34}$$

which is the mean-field description of all binary regular mixtures.

Combining the energy of mixing with the entropy of mixing gives the Helmholtz free energy

$$\Delta F_{mix} = \Delta U_{mix} - T\Delta S_{mix} = kT\left[\frac{\phi}{N_A} ln\phi + \frac{1-\phi}{N_B} ln(1-\phi) + \chi\phi(1-\phi)\right]. \tag{2.35}$$

For polymer solutions it is simplified to the Flory-Huggins equation:

$$\Delta F_{mix} = kT\left[\frac{\phi}{N} ln\phi + (1-\phi)ln(1-\phi) + \chi\phi(1-\phi)\right]. \tag{2.36}$$

The last term is of energetic origin and can obtain positive values, a zero value or negative values. Positive values oppose mixing, at zero it is an ideal mixture and negative values promote mixing. The sign of the Flory interaction parameter χ determines the sign of the entire last term. If there is a net attraction between species the interaction parameter is negative and mixing is always favored. In the more likely case of net repulsion between the species, the interaction parameter has a positive value and the equilibrium state of the mixture depends on the functional dependence of the free energy of mixing on the composition ϕ for the whole range of compositions $\Delta F_{mix}(\phi)$.

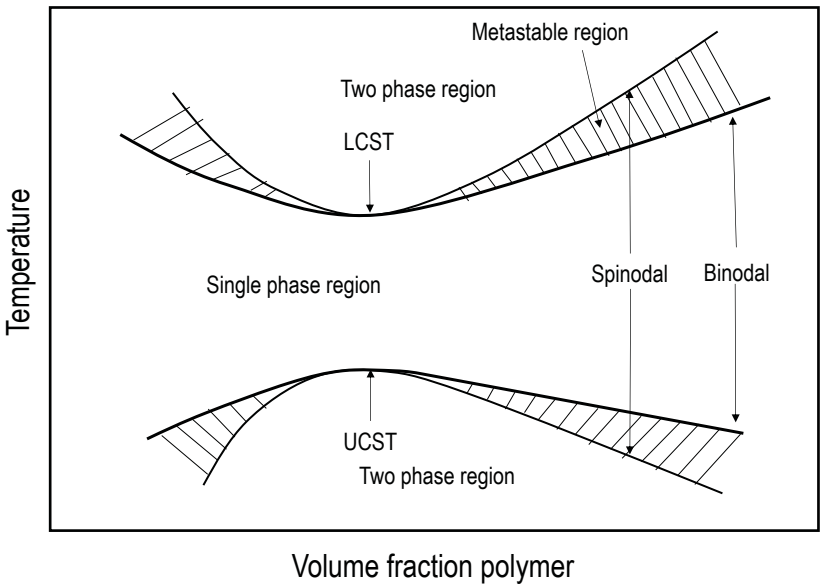

Figure 2.5.: Phase diagram displaying lower and upper critical solution temperature and corresponding binodal and spindodal demixing.

The interaction parameter χ is often written as

$$\chi(T) \approx A + \frac{B}{T}, \tag{2.37}$$

with A the "entropic" and B the "enthalpic" parameter. In this way the Flory parameter accounts for dependences on composition, chain length and temperature that are not trivial. It can be measured by light scattering and values for many polymer blends are listed.[2]

2.2.2. Lower Critical Solution Temperature of Polymers

The phase diagram of a thermoresponsive polymer with a **lower critical solution temperature (LCST)** and an **upper critical solution temperature (UCST)** is displayed in Figure 2.5.

In the following, the LCST will be explained. In the phase diagram, the single phase and two phase region are separated by two binodals. When the first binodal is crossed by an increase in temperature, the metastabil region is entered. In this region, the system is stable against small changes and demixing *via* nucleation and growth occurs. The second

binodal is called a spinodal. Crossing the spinodal leads to spinodal decomposition and demixing of the single phase into two separate phases. This region of the phase diagram is called the miscibility gap. The binodal and spinodal cross at one point in the phase diagram. This point is called a **critical point** and depending on whether it is the minimum or the maximum of the binodals is called the lower or upper critical solution temperature. If the system enters the miscibility gap through a critical temperature, spontaneuos demixing occurs. Critical solution temperatures make systems based on thermoresponsive polymers interesting for many applications such as sensors or delivery applications. A detailed description of the phase behaviour of PNIPAM is given by Halperin *et al.*.[3]

2.3. Polymer Dynamics

2.3.1. Rouse and Zimm Dynamics

The Rouse and Zimm model describe unentangled polymer dynamics. The Rouse model neglects hydrodynamic interactions and should only be applied to polymer melts. In contrast, the Zimm model is suited to describe the dynamics in polymer solutions.[2]

The Rouse model In 1953 Rouse published the first successful molecular description of unentangled polymer dynamics.[4] In the Rouse model a polymer chain is described by an arrangement of N beads, connected *via* springs of a root-mean square size b.
Each bead possesses its own friction coefficient ζ with solvent freely draining through the chains. The friction coefficient for the entire Rouse chain is

$$\zeta_{Rouse} = N\zeta. \tag{2.38}$$

The diffusion coefficient of a Rouse chain is described using the **Stokes-Einstein relation**

$$D_{Rouse} = \frac{kT}{\zeta_{Rouse}} = \frac{kT}{N\zeta}. \tag{2.39}$$

The characteristic time during which the polymer diffuses a distance of the order of its size is called the **Rouse time**.

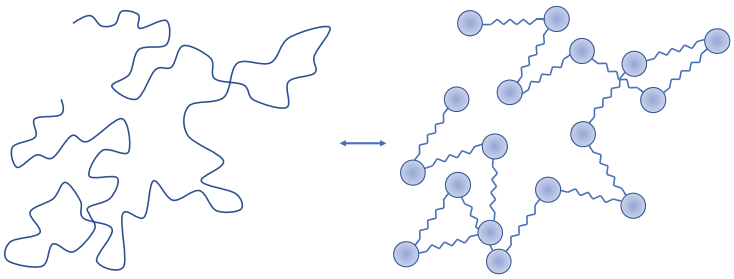

Figure 2.6.: Depiction of a polymer chain as a Rouse chain, where N monomers are represented by N beads connected by springs.[2]

$$\tau_{Rouse} \approx \frac{R^2}{D_{Rouse}} \approx \frac{R^2}{kT/(N\zeta)} = \frac{\zeta}{kT} N R^2. \tag{2.40}$$

For times shorter than the Rouse time viscoelastic modes of the polymer chain are observed, while times longer than the Rouse time mean simple diffusive chain motion.

The size of the Rouse chain can be described as

$$R \approx bN^{\nu}, \tag{2.41}$$

where ν is the reciprocal of the fractal dimension of the polymer. For ab ideal chain ν equals $1/2$.

The Rouse time can further be described as a product of the Kuhn monomer relaxation time and a power law in the number of the monomer units in the chain. The Kuhn monomer relaxation time τ_0 describes the time scale for a motion of the individual beads

$$\tau_0 \approx \frac{\zeta b^2}{kT}. \tag{2.42}$$

For the Rouse time this yields

$$\tau_{Rouse} \approx \frac{\zeta}{kT} N R^2 = \frac{\zeta b^2}{kT} N^{1+2\nu} \approx \tau_0 N^{1+2\nu}. \tag{2.43}$$

For an ideal chain, where $\nu = 1/2$, the Rouse time is proportional to the square of the

number of monomers in the chain

$$\tau_{Rouse} \approx \tau_0 N^2. \tag{2.44}$$

Taking into account the coefficient of $1/(6\pi^2)$, as published by Rouse, the Rouse time for an ideal chain equals

$$\tau_{Rouse} = \frac{\zeta b^2}{6\pi^2 kT} N^2. \tag{2.45}$$

If we further take into consideration the viscosity of the polymer solution this yields

$$\zeta \approx \eta_s b^3 \tag{2.46}$$

for the friction coefficient of each monomer, with η_s the solvent viscosity. Since τ_0 describes the time scale at which a monomer would diffuse a distance of its own size b without being connected to the chain, this results in

$$\tau_0 \approx \frac{\eta_s b^3}{kT} \tag{2.47}$$

and

$$\tau_{Rouse} \approx \frac{\eta_s b^3}{kT} N^2. \tag{2.48}$$

Therefore, no movement of the polymer is observed for time scales lower than τ_0.

Observation of viscoelastic properties therefore is possible for $\tau_0 < t < \tau_R$.
However, the Rouse model is mostly reasonable for polymer melts, since it assumes that beads only interact with each other *via* connecting springs. In contrast, the Zimm model, which will be introduced in the next section, takes into account hydrodynamic interactions.

The Zimm model The Zimm model was first described by Bruno H. Zimm in 1956.[5] It takes into account hydrodynamic interactions. These are long-ranging forces acting on solvent molecules and other particles from the motion of a particle. Therefore, the Zimm model is considered more appropriate for dilute polymer solutions.
In the Zimm model the polymer drags solvent with it within its pervaded volume. Therefore, the pervaded volume of a chain is described as a solid object that is moving through the surrounding solvent. The chain size is

$$R \approx bN^{\nu} \tag{2.49}$$

and the friction coefficient

$$\zeta_{Zimm} \approx \eta_s R. \tag{2.50}$$

Here all numerical coefficients from Stokes' law are dropped, since chains are not spherical objects, for which these numerical coefficients are valid. From eqs. 2.49 and 2.50 we obtain the **Stokes-Einstein relation** for a polymer in dilute solution as

$$D_{Zimm} = \frac{kT}{\zeta_{Zimm}} \approx \frac{kT}{\eta_s R} \approx \frac{kT}{\eta_s b N^{\nu}}, \tag{2.51}$$

where again η_s is the solvent viscosity.

The full calculation for an ideal chain, as published by Zimm in 1956, is

$$D_{Zimm} = \frac{8}{3\sqrt{\pi^3}} \frac{kT}{\eta_s R} \cong 0.196 \frac{kT}{\eta_s R}. \tag{2.52}$$

The Zimm time is, similar to the Rouse time, the characteristic time during which the polymer diffuses a distance of the order of its size

$$\tau_{Zimm} \approx \frac{R^2}{D_{Zimm}} \approx \frac{\eta_s}{kT} R^3 \approx \frac{\eta_s b^3}{kT} N^{3\nu} \approx \tau_0 N^{3\nu}, \tag{2.53}$$

with the full calculation for an ideal chain being

$$\tau_{Zimm} = \frac{1}{2\sqrt{3\pi}} \frac{\eta_s}{kT} R^3 \cong 0.163 \frac{\eta_s}{kT} R^3. \tag{2.54}$$

Table 2.1.: Comparison of description of properties by the Rouse and the Zimm model.

Property	**Rouse**	**Zimm**
Diffusion	$\frac{kT}{N\zeta_0}$	$0.196\frac{kT}{\eta_s R_e}$
Characteristic time	$\tau_{Rouse} = \frac{\zeta R_e^4}{3\pi^2 kTa^2}$	$\tau_{Zimm} = 0.325\frac{\eta_s R_e^3}{kT}$
Mean square displacement	$2a^2(\frac{3kTt}{\pi\zeta a^2})^{1/2}$	$\frac{16}{9\pi^{3/2}}(\frac{\sqrt{3\pi}kT}{\eta_s}t)^{2/3}$
Physical parameter	$\frac{\zeta_0}{a^2}$	-

Comparing the Rouse and Zimm time the two major differences are (1) the Zimm time has a weaker dependence on the chain dimensions as $3\nu < 2\nu + 1$ for $\nu < 1$ and (2) the Zimm motion is a faster process, since there is less frictional resistance as the solvent within the pervaded volume is hydrodynamically coupled to the chain.

Table 2.1 compares the description of properties in the Rouse and the Zimm model.

In Chapters 5 and 6 of this thesis, Zimm-type dynamics will be used to described the segmental polymer dynamics in microgel particles and polymer brushes in a good solvent.

2.4. Cross-Linked and Non-Cross-Linked Polymer Architectures

2.4.1. Microgel Particles

Microgels are submicron particles that consist of 3-dimensional chemically cross-linked polymer networks. The network is swollen by solvent molecules. In contrast to solid particles, microgel particles show viscoelastic behavior. This means that they have properties of both solids and liquids. They are elastic, because under mild deformation they retain their shape. Still, smaller molecules can diffuse into the microgel network, if they are smaller than the microgel's mesh size.[6–8] The elasticity of microgel particles allows for overpacking through deformation, interpenetration and compression[9,10] Microgels can further model hard sphere behavior up to a certain effective volume fraction, above which their behavior differs from hard spheres.[11–13]

A popular microgel system is based on *N*-isopropylacrylamide (NIPAM), cross-linked with *N,N'*-methylenebisacrylamide (BIS, often MBA). Those microgels respond to temperature changes, because PNIPAM has an LCST of approximately 32 °C. Therefore, water molecules are expelled from the polymer network above the so-called volume phase transition temperature (VPTT) and the microgel volume decreases.[14,15] This is displayed in Figure 2.7. Here you can see how water molecules are ordered around the isopropyl and acrylamide groups of the PNIPAM network.[16] As the temperature increases the interactions between the polymer chains are favored over the interactions between polymer and water and the volume of the microgel particles decreases.

Microgels can be synthesized in many different ways. The mechanism of a surfactant-free precipitation polymerization is displayed in Figure 2.8. First, an initiator radical is produced by thermal decomposition in solution. The initiator radical initiates the homogeneous polymerization of monomer and crosslinker, which leads to the growth of charged oligomer radicals. Here, the charge depends on the charge of the thermal initiator. When the oligomer radical, which is not soluble under the reaction conditions, reaches a certain size, it collapses and becomes a precursor particle that is not colloidally stable. As precursor particles coalesce, the charges concentrate at the water interface and colloidally stable primary particles are formed. Newly formed precursor particles are later deposited onto stable primary particles until the polymerization is quenched

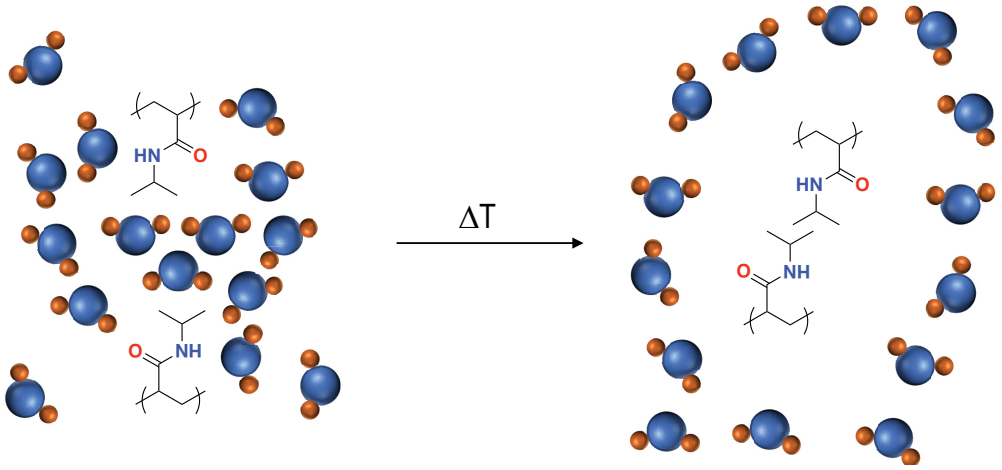

Figure 2.7.: Structure of water molecules surrounding PNIPAM chains below and above the volume phase transition temperature.

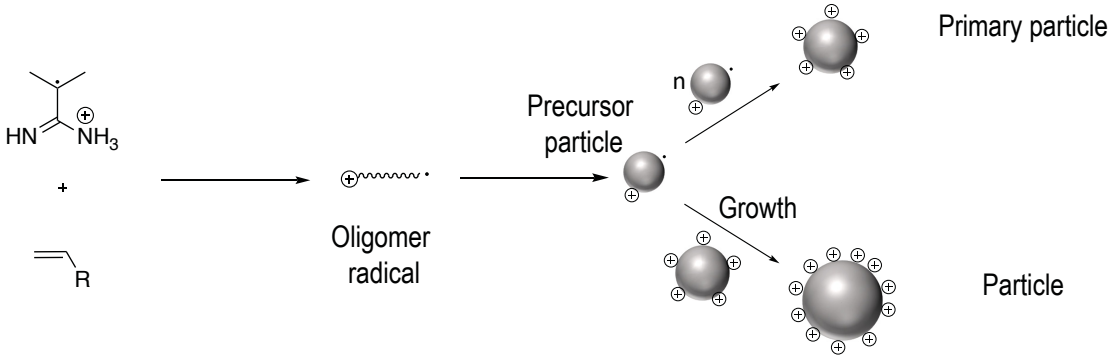

Figure 2.8.: Reaction scheme of surfactant-free precipitation polymerization. Reproduced from 8

and the final particle size reached.

The formation of spheres over a bulk gel is favored by the elevated reaction temperatures during the polymerization. At higher temperatures water and oligomer radicals, precursor and primary particles are phase separated. A sphere is the optimal shape to reduce the interface between water and polymer.[8]
Microgels that are synthesized from NIPAM and BIS in a batch synthesis have an inhomogeneous radial distribution of crosslinker molecules (s. Figure 2.9). BIS is incorporated into the polymer network faster than NIPAM, which leads to decreasing polymer density from the center of the sphere towards its edge. Wu *et al.* first proposed this

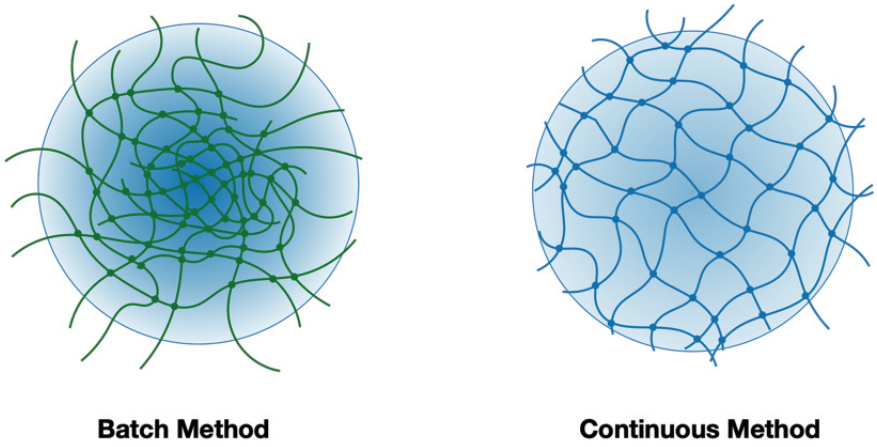

Figure 2.9.: Schematic comparison of the internal structure of microgels prepared by the batch and continuous method.

property when they investigated the reaction kinetics of PNIPAM latex formation.[17] Later, Stieger *et al.*[18] developed a fuzzy sphere model to describe the small angle scattering of those PNIPAM-based microgels particles.

The inhomogeneous distribution of crosslinks influences another important parameter that describes the internal microgel structure: the mesh size. The mesh size measures the distance between two crosslinks in the polymer network.[19] Due to the reaction kinetics described above, the mesh size is not constant throughout the entire network but should on average increase with distance from the particle's center.[20,21]

In recent years, many polymerization methods have been developed to reach a more even distribution of polymer throughout the microgel network. Instead of a batch approach, semi-batch[22] and continuous feeding methods[23,24] have been used. In a semi-batch polymerization parts of the monomer and crosslinker are in the reaction vessel prior to initiation, and the remaining monomer and crosslinker are fed into the system during polymerization. In the feeding method, either only the monomer or no reactant is present in the reaction vessel prior to initiation. After addition of the initiator, the crosslinker (and monomer) is fed into the reaction vessel. Different approaches vary in the initially present amount of monomer and crosslinker, the feeding rate and the duration of the feed. Many more parameters influence the outcome of a precipitation polymerization, such as reaction temperature, crosslinker, monomer and initiator concentration, speed of stirring, polymerization time, and the chosen solvent.

Chapters 4 and 5 investigate and compare the internal structure and dynamics of PNIPAM-based microgels prepared by the conventional batch and a continuous monomer feeding method.

2.4.2. Polymer Brushes

The term polymer brush describes polymer chains end-tethered to a solid substrate, such as Au, Si, Ti or polymeric surfaces. These brushes are used to either functionalize a surface or to change its properties, e.g. wettability,[26,27] fouling[28,29] or friction.[30–32] The chain composition (charge, functional groups, copolymers, mixed chains) and chain properties (chain length, dispersity) can be varied to a wide degree, which makes these surface coatings very versatile. Furthermore, polymer brushes can be coated onto substrates of different shapes, curvatures and sizes, such as nanoparticles, nanorods, silicon wafers and others. In most cases, polymer brushes are an example of **non-cross-linked** polymer architectures.[33,34]

The distance between tethering sites determines the system's tethering regime (s. Figure 2.10). At a distance between the polymer chains of $D > 2R_g$, there are no interactions between the tethered chains and they act as single free chains. Depending on the interactions with the substrate there are two subregimes: the mushroom and the pancake regime. The **mushroom regime** results from weak or repulsive interactions with the surface, whereas the **pancake regime** results from strong attractive interactions.

For moderate and low distances between the tethering sites, where $D < 2R_g$, the chains begin to interact with each other. The steric repulsion between the chains leads to a stretching away from the surface. This, however, reduces the entropy of the system, which is unfavorable. The polymer chains desire to find a balance between the random walk (more coiled) and the stretching due to steric repulsion. This regime is called the **brush regime**.[25]

The **reduced tethered density** Σ is used to further describe the tethering regime. Σ represents the number of chains occupying the area, which under the same conditions would be occupied by a free non-overlapping polymer chain. It is defined as

$$\Sigma = \sigma \pi R_g^2, \tag{2.55}$$

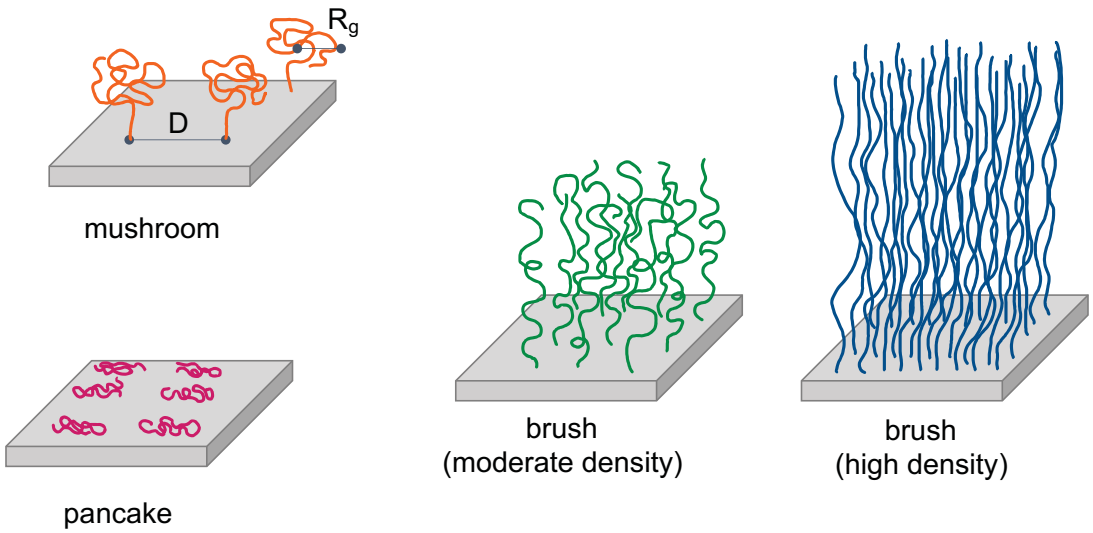

Figure 2.10.: Tethering regimes of polymer brushes.[25]

where σ is the grafting density.

At $\Sigma < 1$ the tethered chains are in the mushroom regime, at $\Sigma \approx 1$ the crossover to the brush regime is reached, $\Sigma > 1$ describes the highly stretched regime and at $\Sigma >> 1$ the brush regime is fully established.[33]

Atom transfer radical polymerization

Controlled radical polymerization (CRP) techniques allow the synthesis of polymers with a defined molecular weight and a narrow molecular weight distribution. The advantage over conventional radical polymerization is the extended lifetime of the growing chain from approximately 1 s to 1 day. Periods of dormancy are broken up by short active periods. Examples for such CRPs are nitroxide-mediated polymerization (NMP), reversible addition-fragmentation chain transfer polymerization (RAFT) and atom transfer radical polymerization (ATRP).

Advantages of ATRP are a straightforward experimental setup and a variety of commercially available monomers, solvents and initiators. In addition to ATRP in solution, ATRP can be used relatively easy to graft polymer brushes from a multitude of surfaces. This is called surface-initiated atom transfer radical polymerization (SI ATRP).

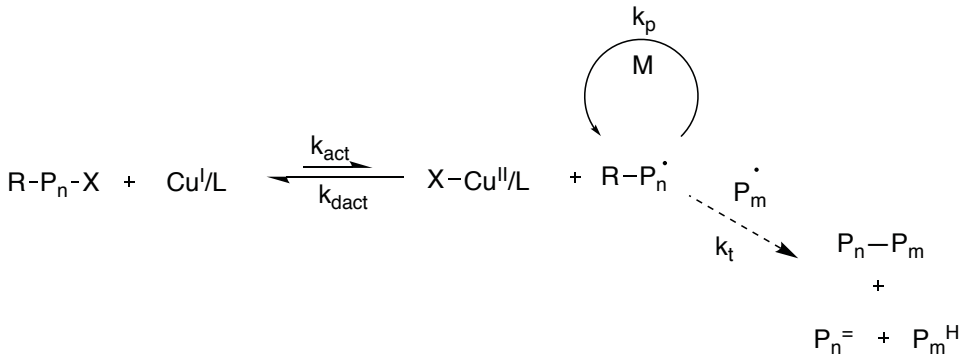

Figure 2.11.: The mechanism of an ATRP. Reproduced from Ref. 35.

All polymer brushes in this thesis were prepared by SI ATRP.

In an ATRP a controlled polymerization is reached through a fast, dynamic activation-deactivation equilibrium between radicals and dormant alkyl halides. The cleavage of a C-X bond requires high energies and therefore a catalytic process is used to avoid the application of high temperatures.

Figure 2.11 shows the reaction scheme of an ATRP. The dormant alkyl halide ($P_n - X$) is activated by the transition metal catalyst in the lower oxidation state (Cu^I/L), which generates the higher oxidation state halide complex ($X - Cu^{II}/L$) and a radical $P_n^{\cdot}$. After one to several monomer additions the radical stops propagation and is deactivated to the dormant species ($P_n - X$). This fast and efficient deactivation is crucial to obtain polymers with a predefined molecular weight and a narrow molecular weight distribution.

The rate of an ATRP depends on the monomer concentration [M], radical concentration $[P^{\cdot}]$ and the rate coefficient of propagation k_p according to

$$R_p = -\frac{d[M]}{dt} = k_p[M][P_n^{\cdot}], \tag{2.56}$$

and the equilibrium constant is

$$K_{ATRP} = \frac{[X - Cu^{II}/L][R^{\cdot}]}{[Cu^I/L][RX]}. \tag{2.57}$$

Therefore, the rate of polymerization is determined by the ratio of $[Cu^I]/[Cu^{II}]$ and not the total concentration of catalyst. Other factors that mainly determine the kinetics

of an ATRP are the choice of initiator, catalyst system, solvent, temperature and additives.[35]

The two most commonly used synthetic approaches for polymer brushes are the "grafting to" and the "grafting from" approach.[35]

For the **"grafting to" approach**, polymer brushes are pre-formed in solution and attached to the substrate *via* a reactive end-group.[36] This has the advantage that the pre-formed polymer chains can be thoroughly characterized prior to surface attachment and can be separated by size. This results in a low molecular dispersity of the resulting polymer brush. However, the disadvantage is that less dense brushes are achieved. An already attached polymer chain will repel other polymer chains, due to excluded volume effects, leading to larger distances between grafting sites.

The **"grafting from" approach** allows the *in-situ* growth of polymer chains from the surface.[36] First, the surface is functionalized with an initiator layer, which will initiate the polymerization of the monomer. The monomer is fed to the substrate from the solution. This allows higher grafting densities, because the monomer diffusion to the reactive sites of simultaneously growing chains determines the brush growth kinetics. However, because the polymer chains cannot be separated by size prior to grafting, and initiator coverage, reactivity and occurring termination reactions between growing chains play an important role, the "grafting from" approach results in higher molecular dispersity .

The kinetics of SI ATRP are analogous to ATRP in solution. However, due to a lower concentration of radicals the addition of deactivating species into the bulk reaction solution helps to enhance the control over the polymerization. Termination between neighboring chains is unlikely, however it has been shown that radical centers may migrate through activation-deactivation cycles leading to termination reactions.[37]

Scaling Laws

Conformations and concentration profiles of polymer brushes can be discussed in terms of scaling laws.[38–44] The theoretical picture displayed in Figure 2.12a was first described by Alexander[38] and later adopted by De Gennes.[39] As described in the previous section, polymer chains end tethered to a solid surface at an average distance D below the radius of gyration R_g of the chain in a good solvent will stretch away from the surface. The height h of the brush layer results from a free-energy-balance argument

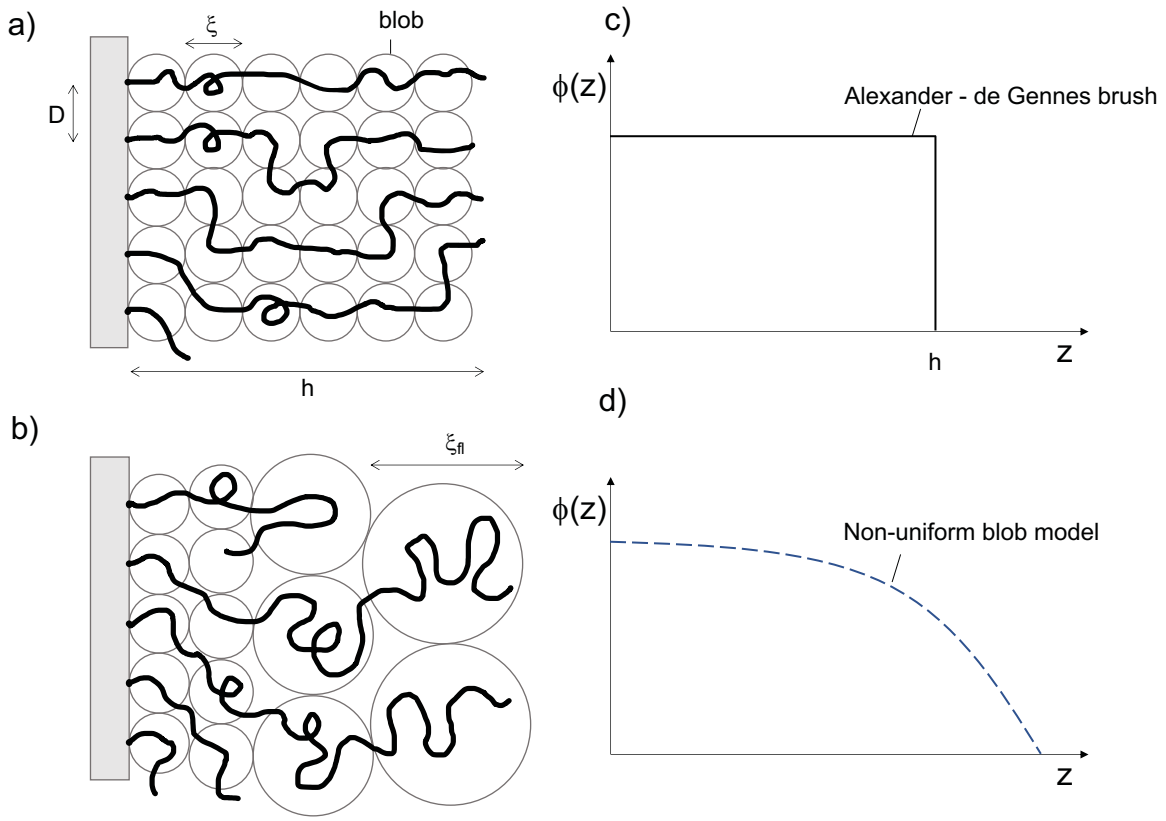

Figure 2.12.: a) Alexander-de Gennes and b) non-uniform blob model for polymer brushes. c)+d) Corresponding polymer volume fraction $\Phi(z)$ profiles.[34,41]

$$\Delta F \propto k_B T \left[\frac{3h^2}{2Na^2} + wN\left(\frac{N\sigma}{h}\right) \right], \tag{2.58}$$

where ΔF is the free energy cost per chain, h is the height of the brush layer, N is the number of monomers in a chain, a is the Kuhn length and w is the excluded volume parameter.[34] In other words, at $D < R_g$ the tendency to maximize the configurational entropy by adoption of random walk configurations and the tendency to interact with solvent molecules, rather than with neighboring chains, oppose each other. For this reason the brush adopts a height h to minimize the free energy cost.[34]

"Blobs" are units of subdivision of the grafted chain. Each blob contains a certain number g_D of monomers and according to de Gennes the average distance between the grafted sites D scales as

$$ag_D^{3/5} = D. \tag{2.59}$$

Within the blob correlations are dominated by excluded volume effects. According to Alexander, the brush layer is treated as a semi-dilute polymer solution, hence the blob size is derived from the static correlation length ξ.[45]

The theoretical consideration by Alexander and de Gennes implicate a box profile for the polymer density as a function of the distance from the grafting surface (Figure 2.12c). Another theoretical approach for the description of polymer brushes can be derived from the works of Semenov[44] and Milner and Witten.[42,43] In contrast to the Alexander-de Gennes brush, Semenov, Milner and Witten assume a parabolic density profile of the polymer brush (Figure 2.12d). They argue that polymer chain ends do not have to be situated towards the boundary, but can penetrate back into the brush layer, causing a slightly higher polymer density $\phi(z)$ towards the substrate and a parabolic decrease of polymer density towards the boundary. Furthermore, the chain ends are distributed over the height of the brush layer, contributing to the parabolic brush profile. This results in a non-uniform blob picture where the blob size increases with the distance z from the surface (Figure 2.12b).

The non-uniform blob model has been adopted by Binder in simulation studies as well.[40] The parabolic polymer density profile can be described by

$$\phi(z) = \phi(0)[1 - (z/h)^2]. \tag{2.60}$$

However, this description fails for the size of the last blob ξ_{fl}, which scales as[40]

$$\xi_{fl} \propto \sigma^{-1/6} N^{2/5} \tag{2.61}$$

and can assume 10 - 20% of the entire brush height.[46]

Further, in the high coverage regime, the so-called over-stretched regime,[47,48] additional three body interactions need to be taken into account and the density profile assumes an elliptic profile according to[49,50]

$$\phi(z) = \phi(0)[1 - (z/h)^2]^{1/2}. \tag{2.62}$$

PNIPAM-based brushes with different grafting densities are subject to Chapter 6 of

this thesis. A combination of ellipsometry and neutron scattering techniques is used to experimentally investigate the structure and dynamics in such systems.

2.5. Neutron Scattering

Neutron scattering uses neutrons to probe matter. Neutrons are uncharged subatomic particles with a mass of 1.0087 atomic mass units, a spin of 1/2 and a magnetic moment μ_n of -1.9132 nuclear magnetons.[51] As neutral particles their interactions with matter are short ranged and they interact with the nuclei of atoms. Therefore, the probability of interaction is small and these subatomic particles penetrate deep into matter.

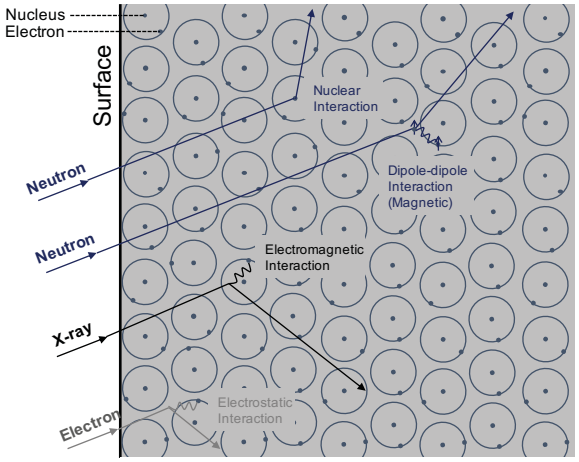

Figure 2.13.: Scattering of different probes by condensed matter. Reproduced from Ref. 52.

Advantages of neutron scattering over other techniques such as X-ray scattering are the observability of light atoms, such as hydrogen, and the availability of isotopic replacement to mark selected atoms. This is especially advantageous in the study of soft matter. Hydrogen, which is abundant in soft matter, is a light atom and can be replaced by deuterium. Moreover, due to spin-based dipole-dipole interactions with unpaired orbital electrons, neutrons are well-suited to study magnetic materials. Figure 2.13 illustrates the interaction of different probes with condensed matter.

2.5.1. Elastic Neutron Scattering

Elastic scattering refers to scattering events where no energy is exchanged between neutron and sample. The scattering of the neutron leads to a change in momentum $\mathbf{P}$. This can be described by

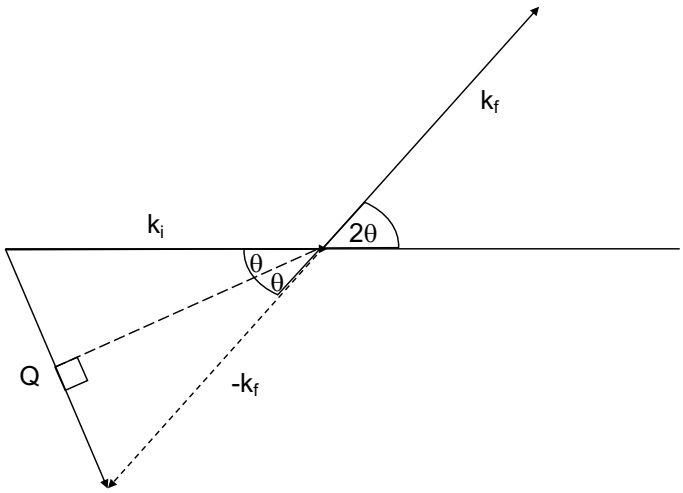

Figure 2.14.: Geometry of elastic scattering. Reproduced from Ref. 52.

$$\mathbf{P} = \hbar k_i - \hbar k_f = \hbar \mathbf{Q} \tag{2.63}$$

where $\hbar = h/2\pi$, the so-called reduced Planck constant, and $\mathbf{Q} = k_i - k_f$ the momentum transfer. k_i and k_f are the initial and final wave vectors. Figure 3.15 shows the scattering geometry of an elastic scattering experiment.

The modulus of the incident wave vector $|k_i|$ is unchanged (no energy exchange) and therefore $|k_i| = |k_f|$. Basic geometry yields

$$\frac{|\mathbf{Q}|}{2} = |k_i| \sin\theta = \frac{2\pi}{\lambda} \sin\theta. \tag{2.64}$$

hence the modulus of the momentum transfer is

$$|\mathbf{Q}| = \frac{4\pi \sin\theta}{\lambda}. \tag{2.65}$$

In neutron scattering experiments the proportion of incident particles that emerge with a given energy and momentum transfer is measured, which results in a four dimensional function $S(\mathbf{P}, E)$, which is mostly written as $S(\mathbf{Q}, E)$ or $S(\mathbf{Q}, \omega)$. All scattering has an elastic and an inelastic contribution, but since the inelastic contribution is comparatively small, it is neglected in elastic scattering experiments. Therefore, the energy transfer in elastic scattering is assumed to be zero, and the function is reduced to $S(\mathbf{Q})$, which is three dimensional with $\mathbf{Q} = (Q_x, Q_y, Q_z)$.

Examples for elastic neutron scattering techniques are neutron diffraction, small angle neutron scattering and neutron reflectometry.[52]

2.5.2. Inelastic Neutron Scattering

In inelastic scattering, which is measured e.g. in neutron spin echo spectroscopy, the change in energy after a scattering event is measured. Therefore, in contrast to elastic scattering, $S(\mathbf{Q}, \omega)$ remains four-dimensional. Figure 2.15 shows how the wave vector diagram changes for inelastic scattering.

In case of inelastic scattering the moduli of the incident and final wave vector are no longer equal ($|k_i| \neq |k_f|$), and therefore the incident and final wavelength differ as well ($\lambda_i \neq \lambda_f$). As the resulting triangle is no longer isoscele the formula

$$|\mathbf{Q}^2| = k_i^2 + k_f^2 - 2k_i k_f \cos 2\theta \tag{2.66}$$

applies.

The change of wavelength for a proton is associated with a change in frequency. However, for a neutron the kinetic energy is considered and

$$\omega = \frac{\pi h}{m_n}\left(\frac{1}{\lambda_i^2} - \frac{1}{\lambda_f^2}\right) \tag{2.67}$$

and

$$E = E_i - E_f. \tag{2.68}$$

Therefore, $E > 0$ is associated with a loss in energy and $E < 0$ with an energy gain.

The scattering function now is

$$S(\mathbf{Q}) = \int_{-\infty}^{\omega_i} S(\mathbf{Q}, \omega) d\omega \tag{2.69}$$

with an elastic contribution S_{el} of

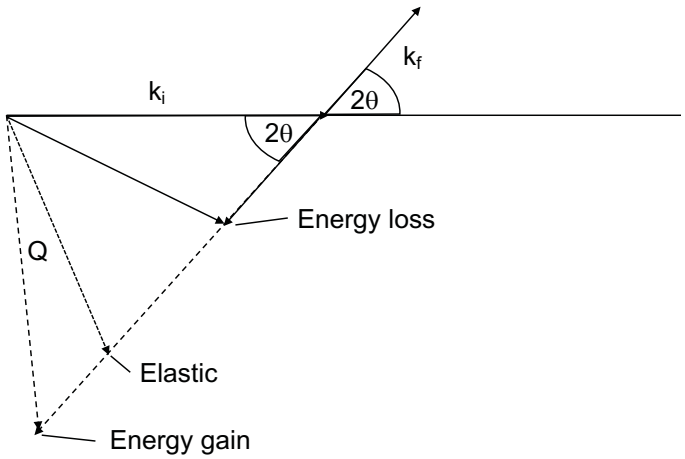

Figure 2.15.: Geometry of inelastic scattering. Reproduced from Ref. 52.

$$S_{el}(\mathbf{Q}) = S(\mathbf{Q}, \omega = 0) \tag{2.70}$$

It is crucial to keep in mind that no more than the initial energy $\hbar\omega_i$ can be transferred to the sample. Examples for inelastic neutron scattering techniques are neutron spin echo and neutron backscattering spectroscopy.[52]

In the experiments presented in this thesis, elastic and inelastic neutron scattering techniques are used to investigate the structure and dynamics of soft condensed matter. A more detailed description of different neutron scattering techniques such as small angle neutron scattering, neutron reflectometry and neutron spin echo spectroscopy follows in the next chapter.

3. Materials and Methods

3.1. Materials

All chemicals were used as received. *N*-Isopropylacrylamide (NIPAM; ≥99 %), poly(*N*-isopropylacrylamide (PNIPAM; average M_n=30 000, PDI=1.5), *N,N'*-methylenebisacrylamide (BIS; 99 %) and 2,2'-azobis(2-methylpropionamidine) dihydrochloride (AAPH; 97 %), copper(I) chloride (99.995%, trace metal basis), copper(II) chloride (99%), *N*, *N'*, *N"*, *N"*-pentamethyldiethylenetriamine (PMDETA, ≥ 99%), trichlorododecylsilane (≥ 95% (GC)), tetrabutylammonium fluoride solution (TBAF, 1 M in THF) and tetrahydrofuran (THF, anhydrous ≥ 99.9% inhibitor-free) were purchased from Sigma-Aldrich. Hydrogen peroxide solution (30 %), methanol (z.A. min. 99.8% CH_2OH) and sulfuric acid (z.A. 95%) were purchased from CHEMSOLUTE®. Toluene (dried, max. 0.005% H_2O) was purchased from SeccoSolv®. Ethanol (absolute) was purchased from VWR CHEMICALS. [11-(2-Bromo-2-methyl)propionyloxy]undecyltrichlorosilane (eBMPUS) was purchased from Gelest. D_2O (99,9%) was purchased from Deutero. Water was purified with a MilliQ system (Millipore) with a resistance of 18 MΩ.

Silicon wafers and double-sided polished silicon wafers (both <100>, n-type) were purchased from MicroChemicals. Silicon blocks were purchased from Siliciumbearbeitung Andrea Holm GmbH.
Carl Roth™ membrane tubes based on regenerated cellulose (RC membranes, MWCO = 14 kDa) and Spectrum™ membrane tubes based on cellulose ester (CE membranes, MWCO = 6 - 8 kDa) were purchased from FisherScientific. Amicon® Ultra-4 centrifugal filter devices (MWCO = 3 kDa) were purchased from Merck.

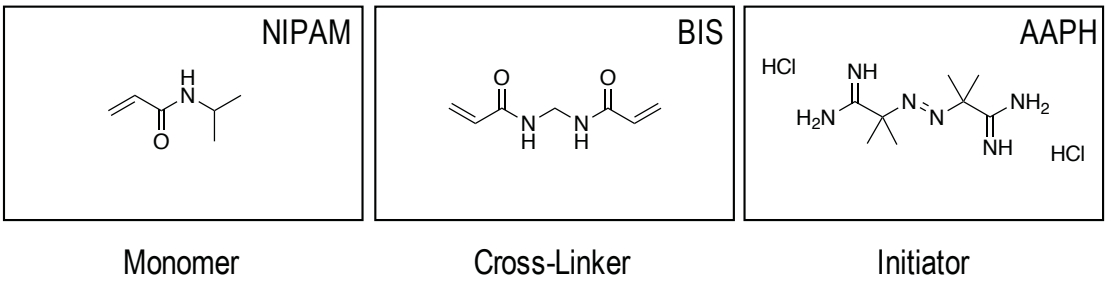

Figure 3.1.: Reactants used for surfactant-free precipitation polymerization.

3.1.1. Sample Preparation

Microgel Particles

Microgel particles based on the monomer NIPAM with various amounts of cross-linker BIS were synthesized by surfactant-free precipitation polymerization. First, the batch method according to Pelton and Chibante[14] was used, which yields a heterogeneous distribution of cross-links as described by Wu *et al.*[17] Furthermore, a continuous monomer feeding method[23,53] was implemented, which leads to a more even distribution of cross-linker throughout the microgel particle. The chemical structure of the reactants is displayed in Figure 3.1. Detailed information concerning the precipitation polymerization can be found in Table A.1 in the Appendix.

Batch Method NIPAM and BIS were dissolved in 120 mL water in a 250 mL double-walled glass reactor with a PTFE baffle and overhead stirrer. The reaction solution was continuously stirred at 300 rpm, heated to 80 °C and purged with nitrogen for 60 min for oxygen removal. Before addition of the initiator (AAPH, 68.7 mg in 1 mL water) the stir rate was increased to 1000 rpm. The polymerization was carried out for 10 min before the turbid microgel dispersion was released into an ice-cooled beaker to quench the reaction.

Continuous Monomer Feeding Method 100 mL water were filled into the double-walled glass reactor and treated as is described above. In a separate beaker, NIPAM and BIS were dissolved in the remaining 20 mL water and purged with nitrogen for 60 min. Monomer and cross-linker were filled into a syringe and fed into the reactor at a rate of 2 mL/min. After 11 min 20 s the reaction was quenched as described above.

Purification Independent of the chosen polymerization method, unreacted monomer and low molecular weight oligomers were removed from the microgel dispersion by dialysis. The molecular weight cut-off (MWCO) of the RC membrane was 14 kDa. Prior to dialysis the membrane was stored in ultrapure water for 30 min to remove residue glycerin. The dialysis was carried out over 21 days with two solvent exchanges per day. Afterwards, the microgel dispersion was lyophilized at -85 °C and $1x10^{-3}$ bar until complete water removal.

LC-MS The conversion of monomer and cross-linker over the polymerization time was tracked with liquid chromatography – mass spectrometry (LC-MS) measurements. Mass spectrometry measurements were conducted on a LTQ Orbitrap XL (Thermo Fisher Scientific, USA) using atmospheric pressure chemical ionization (APCI). LC-MS spectra were recorded at the Analytic Centres of the Institute of Chemistry at TU Berlin by Dr. Maria Schlangen-Ahl and Marc Griffel. The setup is equipped with a Grom-Sil-120-ODS-4-HE column (Grace, Columbia, MD, USA) with a length of 50 mm, inner diameter of 2 mm and particle size of 3 μm. The spectra from the UV channel were analyzed with Freestyle (Thermo Fisher Scientific, USA). To ensure a linear relationship between the peak area and the reactant concentration BIS and NIPAM samples of known concentrations were measured in the concentration range relevant to the polymerization. Calibration curves with a linear regression and HPLC conditions can be found in the Appendix (Figure A.1).

Samples were removed during the polymerization at different times. In more detail, 1.5 mL were removed with a previously THQ-washed syringe to quench the polymerization upon removal. Particles and oligomers were separated from monomer and cross-linker by ultracentrifugation in Amicon® centrifugal filter devices prior to LC-MS measurements.

Spin Coating Microgel monolayers were deposited onto silicon substrates of various dimensions by a spin coating procedure. The technique utilizes the centripetal force that occurs upon high speed spinning of a dispersion, and the surface tension of the liquid to create even coatings. Figure 3.2 schematically displays the spin coating procedure. First, the substrate is covered with the particle dispersion **(1)**. Afterwards, the substrate is rotated at a high speed to remove most of the solvent **(2)**. The solvent then completely evaporates **(3)** and leaves a particle film on top of the substrate **(4)**.[54] The parameters most commonly varied are spinning speed (in rpm), spinning time and

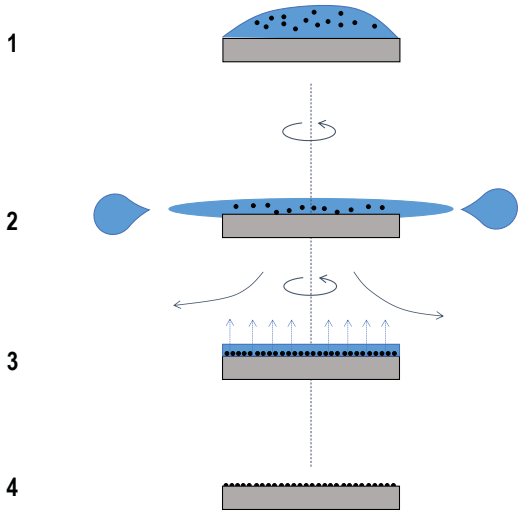

Figure 3.2.: Spin coating procedure. **(1)** A substrate is covered with a dispersion of particles in a liquid solvent. **(2)** High speed rotation of the substrate removes most of the solvent. **(3)** The remaining solvent evaporates. **(4)** The particle film remains on the substrate. Reproduced from Ref. 54.

particle concentration of the deposited dispersion. Specific spin coating parameters are given in the respective chapters.

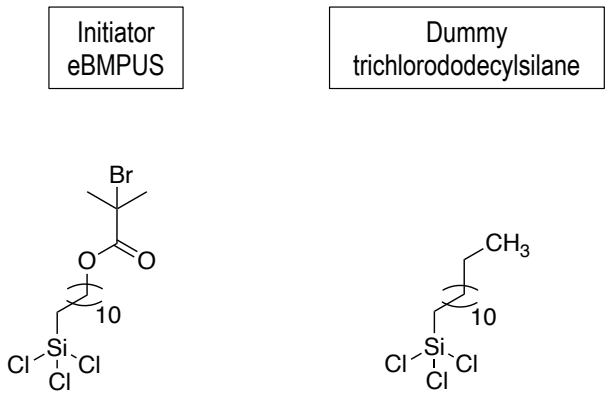

Figure 3.3.: Chemical structure of the initiator (eBMPUS) and the dummy molecule (trichlorododecylsilane) for SI ATRP.

3.1.2. Polymer Brushes

Surface-Initiated Atom Transfer Radical Polymerization PNIPAM brushes were prepared by surface-initiated atom transfer radical polymerization (SI ATRP) as described in the literature.[55]

In order to obtain a reactive hydroxylized surface layer, all silicon substrates were piranha etched. Silicon substrates were placed in a solution of equal parts H_2SO_4 and H_2O_2 for 30 min. Afterwards, the silicon substrates were removed from the piranha solution, thoroughly rinsed with water and dried under a stream of nitrogen. Substrates were then placed in a custom-built reactor, which contained a 0.5 wt% eBMPUS solution in anhydrous toluene, which had been purged with nitrogen for 30 min. In cases where the grafting density was varied, certain ratios of initiator and dummy molecules were present in the initiator solution.[56] Trichlorododecylsilane was chosen as a dummy molecule, because its molecular structure resembles that of the initiator (s. Figure 3.3). The reactor was sealed to prevent gas exchange. After 24 h at room temperature the substrates were removed from the reactor, sonicated in toluene for 15 min, in ethanol for 5 min and dried under a stream of nitrogen. The reaction volume was adjusted to the dimensions of the silicon substrates (Si-wafers vs. Si-blocks).

The SI ATRP was carried out immediately after the initiator deposition. The monomer NIPAM was dissolved in a mixture of equal parts methanol and water in a custom-built reactor. The solution was rigorously stirred at 600 rpm for 30 min, meanwhile being purged with nitrogen. Afterwards, the ligand PMDETA and the activating species

Cu(I)Cl were added to the solution under continuous stirring. To ensure oxygen removal the solution was purged with nitrogen for another 30 min. It was ensured that all Cu(I)Cl had been dissolved, before the initiator-coated silicon substrates were placed in the reactor. To determine the evolvement of brush height over time, samples were removed from the polymerization after 1, 2, 4, 5, and 10 minutes. Removed samples were sonicated in water for 10 minutes, rinsed with water and dried under a stream of nitrogen.

Degrafting and Size Exclusion Chromatography In order to measure their molar mass and molecular dispersity the grafted polymer chains were removed from the substrates.[57,58] Polymer brushes were grafted from two-side polished Si-wafers to maximize the yield of polymer chains for size exclusion chromatography (SEC), and to avoid less controlled reactions on the non-polished, rough side of single-side polished wafers. SI ATRP conditions were the same as described above.
In a cleanroom a commercially purchased solution of TBAF in THF (1 M) was filtered thoroughly and diluted in filtered THF to obtain a 0.04 M solution. This solution was placed in a double-walled glass reactor at 50 °C and 16 coated Si-substrates were submerged in the solution. As the Si-F-bond is stronger than the Si-O-bond TBAF can be used to remove the polymer chains from the substrates as is illustrated in Figure 3.4. To prevent sublimation of THF, the reactor was sealed air-tight. After 24 h the Si-substrates were removed from the reactor and thoroughly rinsed with filtered THF to remove all degrafted polymer. The THF containing the degrafted polymer chains was transferred to a round bottom flask, and carefully removed with a rotary evaporator. A brown resin was obtained and was lyophilized at -85 °C at $1x10^{-3}$ bar for 7 days. For the removal of small contaminants and excess TBAF the resin was redissolved in ultrapure water and dialyzed at 4 °C for 7 days. The low temperature was chosen to ensure the stretched state of the polymer chains. The molecular weight cut-off of the CE membrane was 6 to 8 kDa. Afterwards, the solution was lyophilized again and the obtained brown resin was measured with SEC. To ensure complete degrafting of the polymer brush, X-ray reflectivity curves were recorded after the degrafting procedure.

All SEC measurements were conducted at the Max Planck Institute of Colloids and Interfaces (Golm, Germany) by Marlies Graewert. The SEC instrument is equipped with a series of three PSS gram columns, a guard column and two columns with a particle size of 7 μm and different porosities of 100 and 1000 Å. Prior to the measurements,

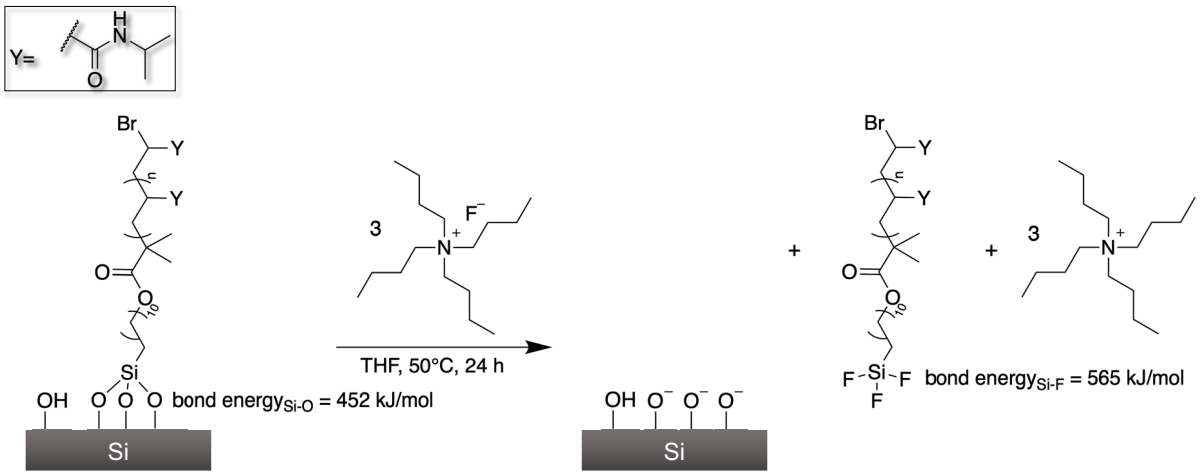

Figure 3.4.: Degrafting of PNIPAM brushes with TBAF.

the setup was calibrated for a molar mass range between 600-2 000 000 g/mol with polystyrene standards. The eluent was *N*-Methylpyrrolidone (NMP) with 0.5 g/L LiBr. SEC measurements were conducted at a flow rate of 0.8 mL/min at 70 °C. A UV detector (SECcurity) and an refractive index (RI) detector were used.

3.2. Methods

3.2.1. Dynamic Light Scattering

In a dynamic light scattering (DLS) experiment monochromatic laser light illuminates a dilute sample that contains scattering centers. The fluctuations of the scattered light are detected by a fast photon detector at a known scattering angle θ. The setup of a typical DLS experiment is depicted in Figure 3.5.

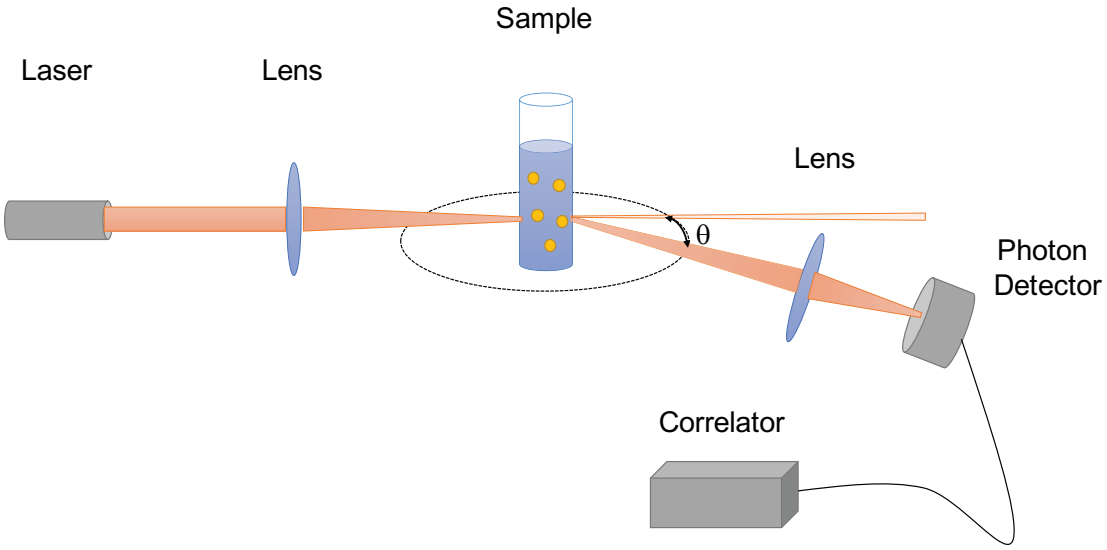

Figure 3.5.: Setup of a DLS experiment.

Dynamic light scattering is a popular non-destructive method to determine the size of objects in samples such as emulsions, micelles, polymers, proteins, nanoparticles, and colloids. As the name dynamic light scattering indicates, the method investigates the mobility of objects in solution, which is based on Brownian motion.[2,59]
The instantaneous scattering intensity $I(Q,t)$ at a certain scattering angle Q depends on the spatial arrangement of the scattering centers at time t. However, as the particles move and change their conformation and location the scattering intensity fluctuates in time. The averaged scattering intensity over a long time interval is the static scattering intensity $I(Q)$. Information about the particle dynamics on the length scale $1/Q$ is contained in the fluctuations around the average value.
Mathematically, the memory of the instantaneous scattering intensity $I(Q,t)$ after $t+\tau$ can be expressed by the time autocorrelation function. At $t = 0$ the autocorrelation

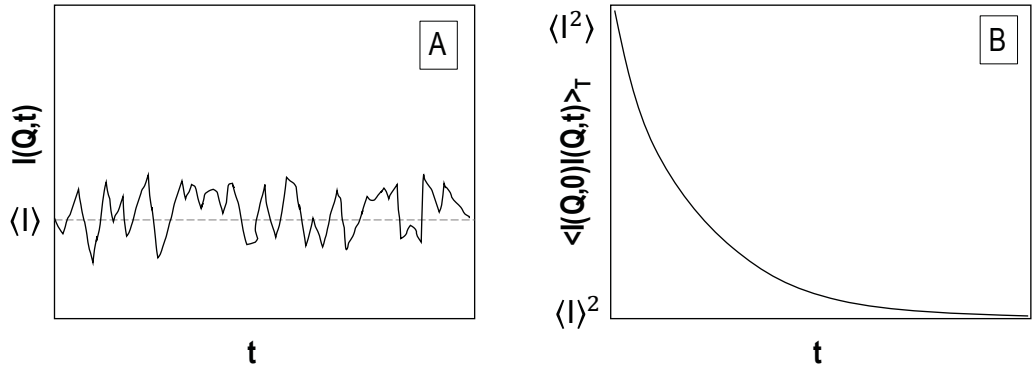

Figure 3.6.: A) Intensity I of scattered light over time. B) Time autocorrelation function of scattered intensity over time.[2]

function is the mean-square value of the intensity $\langle I^2 \rangle$. At times much longer than the correlation time τ, $I(Q,0)$ and $I(Q,t)$ are independent and the autocorrelation function is the square of the average intensity $\langle I \rangle^2$. The normalized intensity correlation function is

$$g_2(Q,\tau) = \frac{\langle I(Q,t)I(Q,t+\tau)\rangle}{\langle |I(Q,t)|^2 \rangle}. \tag{3.1}$$

This can be related to the electric field correlation function $g_1(Q,\tau)$ with the Siegert relation

$$g_2(Q,\tau) = 1 + \beta |g_1(Q,\tau)|^2 \tag{3.2}$$

$$g_1(Q,\tau) = \frac{\langle E_s(Q,t)E_s^*(Q,t+\tau)\rangle}{\langle |E_s(Q,t)|^2 \rangle}, \tag{3.3}$$

where E_s is the electric field of the scattered light and β is the coherence area, which relates to the scattering geometry and the size of the light sensitive area of the detector.

Monodisperse samples display a single exponential decay as displayed in Figure 3.7. The intensity autocorrelation function can be fitted according to

$$g_1(Q,\tau) = exp(-\Gamma\tau), \tag{3.4}$$

with Γ the decay rate. The decay rate is defined by

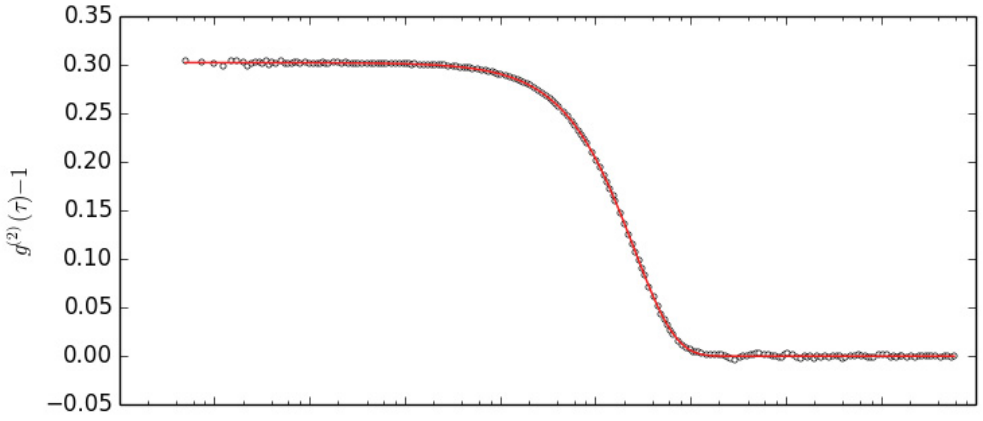

Figure 3.7.: Example for a measured intensity autocorrelation function with a single exponential decay.

$$\Gamma = Q^2 D. \tag{3.5}$$

Q is known and therefore the diffusion coefficient D can be determined. In turn, the Stokes-Einstein relation can be used to determine the hydrodynamic radius R_h of the scattering object

$$R_h = \frac{kT}{6\pi\eta D}, \tag{3.6}$$

with k the Boltzmann constant, T the temperature in K, an η the solvent viscosity. The hydrodynamic radius R_h is the radius of a sphere that would experience a friction f, identical to the friction experienced by the scattering particle during Brownian motion through the solution.

In a DLS experiment there are a few pitfalls that need to be kept in mind. To get accurate information on the particle size distribution, it is recommended to measure at multiple scattering angles (multi-angle DLS). This is because the scattering intensity of differently sized particles depends on the scattering angle. Therefore, if only one scattering angle is applied, the scattering signal from particles with a certain size can be suppressed.

Furthermore, the theory is not valid for multiple scattering. Concentrated and turbid samples should therefore not be measured by DLS. A way to suppress multiple scattering

is cross-correlation. Diffusing wave spectroscopy (DWS) is an alternative method that can be used to describe multiple scattering.
There are different methods to analyze DLS data. The cumulant analysis is suitable for noisy data with one particle population. It assumes a Gaussian distribution around a single particle size and therefore is not well-suitable for bimodal samples. In case of a bimodal sample, a CONTIN analysis, based on the CONTIN algorithm, is recommended.

Experimental Setup Dynamic light scattering of PNIPAM microgels was conducted on an LS spectrometer (LS Instruments, Fribourg, Switzerland). A decaline bath was used for temperature control and refractive index matching. Autocorrelation functions were measured at temperatures between 18 and 50 °C at scattering angles between 30 and 90° in 5° steps. The solvent was H_2O and the microgel concentration was 0.05 mg mL^{-1}. A He-Ne laser with a wavelength $\lambda = 632.8$ nm was used. The raw data was fitted with a third-order cumulant fit in a Python-based fitting script written by Anja Hörmann (Python Software Foundation, version 2.7).

3.2.2. Electrophoretic Light Scattering

Electrophoretic light scattering (ELS) uses the principle of electrophoresis to determine the zetapotential of colloidal particles in liquid dispersions. The surface of dispersed charged particles is surrounded by an electrochemical double-layer. This is displayed in Figure 3.8. The layer adjacent to the charged particle surface is called the Stern layer. The Stern layer is oppositely charged to the particle surface. However, with increasing distance to the particle surface the charge distribution becomes more diffuse. As the particle moves, surrounding charges are dragged along up to the distance which is marked by the slipping plane. Charges that are beyond the slipping plane do not move along with the particle. The potential at the slipping plane is referred to as the zetapotential. The potential decreases linearly between the particle surface and the Stern layer, and exponentially from thereon. This is described by Debye's law.[60,61]
Particle dispersions are increasingly stable with higher zetapotential as particles with a high charge are stabilized and tend to aggregate less. Parameters that influence colloidal stability are pH, ionic strength and sample concentration.
During an ELS experiment, the velocity of the movement of particles at an applied potential (v_{ep}) is measured. This is called the electrophoretic mobility. Particles should have a size between 1 nm and 20 μm to be suitable for ELS and the concentration of

the dispersion should be low. The equation most commonly used for the calculation of the zetapotential from v_{ep} is the Smoluchowski equation:

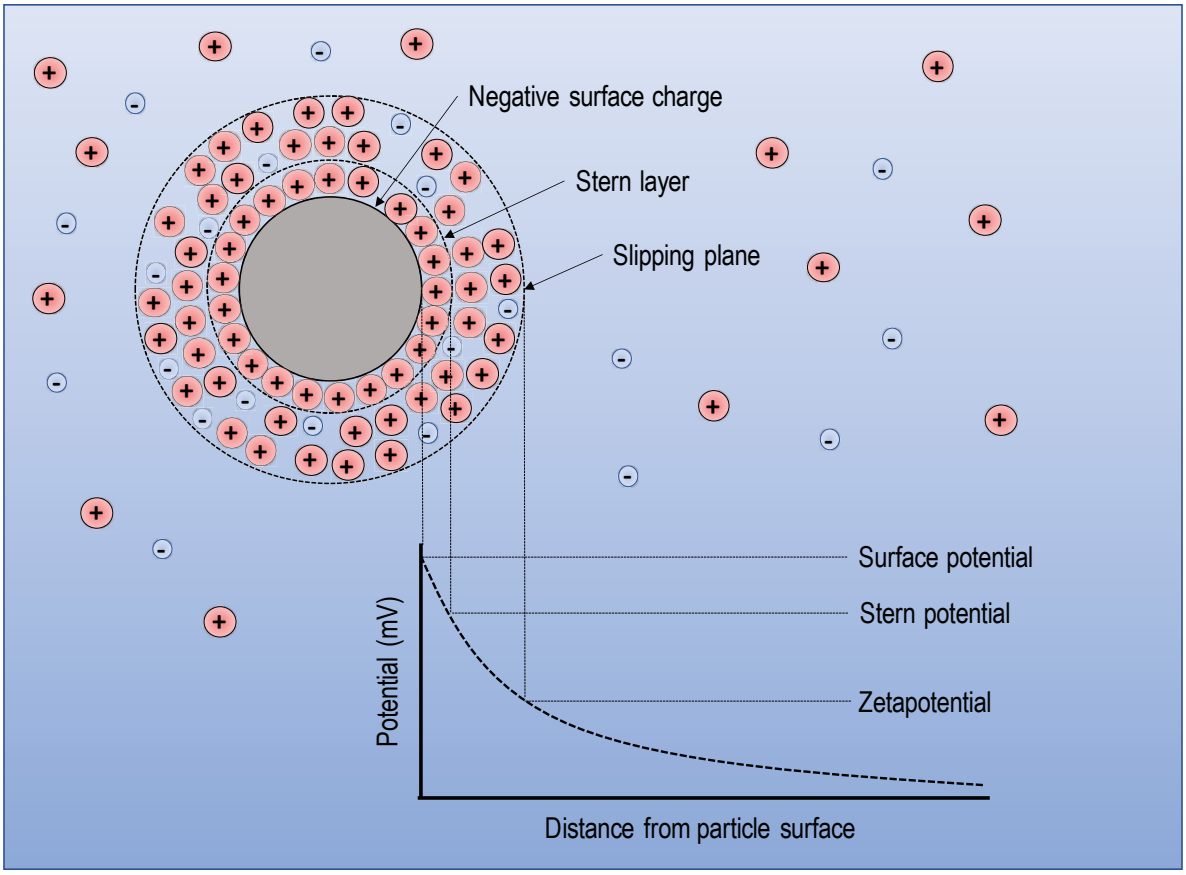

Figure 3.8.: Schematic representation of the potential as a function of the distance from a charged particle surface. Reproduced from Ref. 62.

$$\zeta = \frac{v_{ep}}{E} \frac{\nu}{\epsilon_f \epsilon_0} \tag{3.7}$$

where E is the magnitude of the electric field, ν the kinematic viscosity of the dispersion medium, and $\epsilon_f \epsilon_0$ the permittivity.

The Smoluchowski equation is only valid for particles with a very thin electrochemical double-layer. The effective thickness of the electrochemical double-layer is quantified by the Debye-length κ. Other models have been developed by Hückel, and Sumner and Henry to calculate the zetapotential for colloidal particles with thicker electrochemical double-layers. However, the Smoluchowski equation remains the most commonly used

equation in every day laboratory practice.

For an ELS measurement a particle dispersion with a low concentration is filled into a capillary (glass, polymeric), which has to electrodes at its end. Those electrodes generate the electric field. Due to effects from the wall, the determination of the zetapotential can only be done at a certain distance from the capillary wall. A laser is used and the Doppler effect is taken advantage of to determine the velocity of several particles at once.[61]

Experimental Setup ELS measurements were conducted on a Litesizer 500 (Anton Paar, Graz, Austria), which is equipped with a 658 nm laser. The samples were measured at temperatures between 18 and 50 °C at a concentration of 0.05 mg mL^{-1}.

3.2.3. Atomic Force Microscopy

Atomic force microscopy (AFM) measures surface structures with high resolutions of up to 0.1 nm. In contrast to optical microscopy, AFM does not use visible light and lenses to magnify small objects. In AFM a sharp probe is used to scan a surface area and translate the interactions between the surface and probe into a topographic image. The method was invented by Binnig, Quate and Gerber in 1986 and is related to techniques such as the Stylus profiler, the topografiner or Scanning Tunneling Microscopy (STM). However, AFM has many advantages, such as a high resolution, a wide range of scan sizes (5 nm to 100 μm) and the ability to scan very soft to very hard surfaces. Furthermore, in contrast to STM, TEM and SEM, the AFM is able to scan conducting and insulating samples. Figure 3.9 shows a comparison of the different length scales accessible with different microscopy techniques. With an AFM samples can be measured under ambient conditions and minimal sample preparation is needed. However, if need be, samples may be scanned under vacuum, in gas or liquid as well.[63]

Figure 3.10 shows the setup of an AFM experiment. The cantilever with an integrated tip is inserted into a holder and the sample is placed underneath the tip. The vertical position of the cantilever is then controlled by a piezoelectric transducer, which converts electrical potential into mechanical motion. In this way, very accurate control of small movements can be realized. Typical piezoelectric transducers move 0.1 nm for every volt. The cantilever acts as a force transducer. Commonly, AFMs use optical levers as

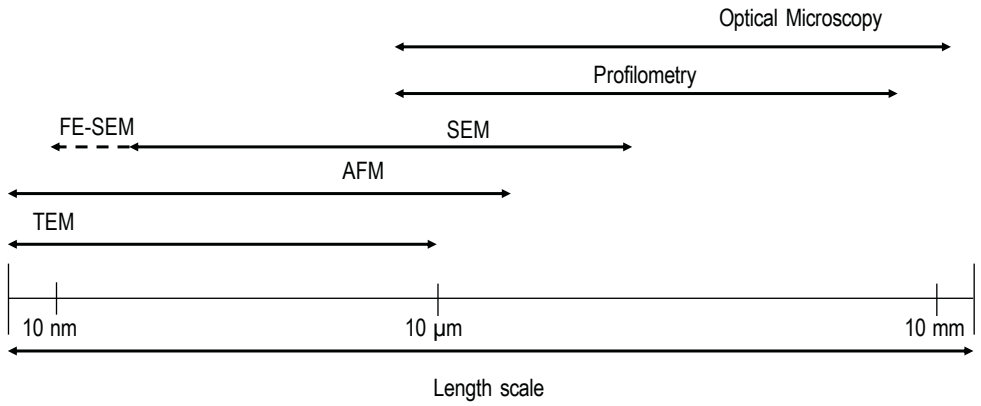

Figure 3.9.: Length scales accessible by different microscopy methods. Reproduced from Ref. 63.

displayed. Here a laser is focused on the back of a reflective cantilever and the laser beam is reflected onto a split photodetector. The position of the laser spot is measured and a change equals a change of the force experienced by the cantilever. At contact with the surface the voltage output of the force transducer increases and forces as low a 10 pN can be measured. Lastly, the feedback control is a crucial element of an AFM. It maintains a set force between the probe and the sample. The control electronics get the signal from the force transducer and send the information to the piezoelectric transducer. In this way, the piezoelectric transducer moves the force transducer away from the surface if an increase in force is registered and moves it closer to the surface at a decrease of force. This up and down movement of the cantilever is then translated into the sample topography.[63]

AFMs can be operated in topographic and non-topographic modes. The major topographic modes are contact mode and oscillatory modes. **Contact mode** was the first mode that was developed for the AFM. The different topographic modes are best explained by taking a look at the force-distance curve describing the interaction between probe and sample as displayed in Figure 3.11. At far distances from the sample, the probe experiences zero force, and there is no interaction between probe and sample. As the probe approaches the sample, it experiences an attractive force, which leads to a snap in of the probe onto the sample. As the probe further approaches the sample, repulsive forces start affecting the probe. The contact mode operates in the repulsive regime, where probe and sample are in close contact.

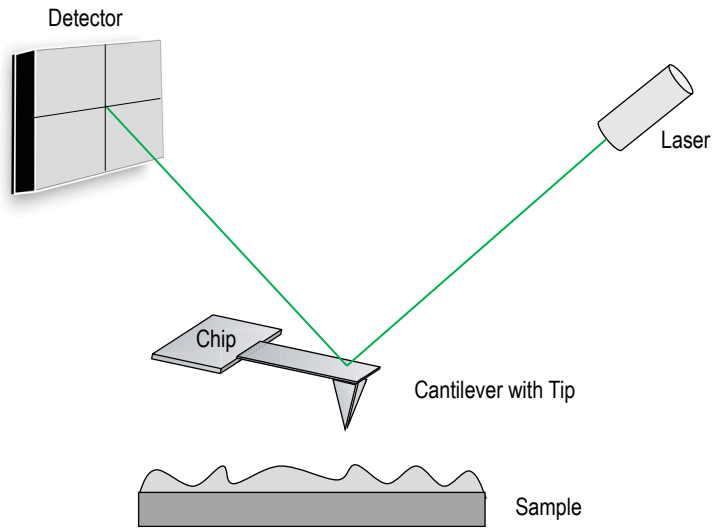

Figure 3.10.: Setup of an AFM experiment. Reproduced from Ref. 63.

While contact mode offers the advantage of a high resolution and fast measurements, it also has some disadvantages. Due to the close contact of probe and sample either the sample or the probe can be damaged. Furthermore, in addition to the vertical forces, in contact mode lateral forces occur. Lateral forces are problematic for weakly adsorbed, soft or easily deformable samples. They can lead to distortion, damage or even removal of the sample.[63]

The **oscillating modes** subsume intermittent contact and non-contact mode. In the oscillating modes the probe is oscillated at its resonance frequency by an additional piezoelectric element. The amplitude is reduced by the contact with the sample, because the force field from the sample interacts with the probe and dampens the cantilever's oscillation. This results in a reduction in the frequency and amplitude of the oscillation. The feedback system reacts to this and keeps a fixed sample-probe distance.

The main difference between intermittent and non-contact mode is the amplitude of the oscillations. In the intermittent contact mode the cantilever undergoes all three regimes due to the large oscillation amplitude between 1 and 100 nm. When it is far away from the sample it experiences zero force. When it approaches the sample further, the attractive regime is reached until it comes into close contact with the sample upon which point the repulsive regime occurs. Upon each oscillation cycle all regimes are passed.

The disadvantage of the intermittent contact mode is that the crossing of the repulsive regime bears the danger of tip or sample damage. However, due to the perpendicular movement during the scan lateral forces are almost eliminated. This is especially useful

for weakly adsorbed, soft or easily deformable samples and make intermittent contact mode the mode of choice for AFM imaging of microgel particles.
In non-contact mode small oscillation amplitudes are used and therefore the cantilever is maintained in the attractive regime with small probe-surface forces.[?]

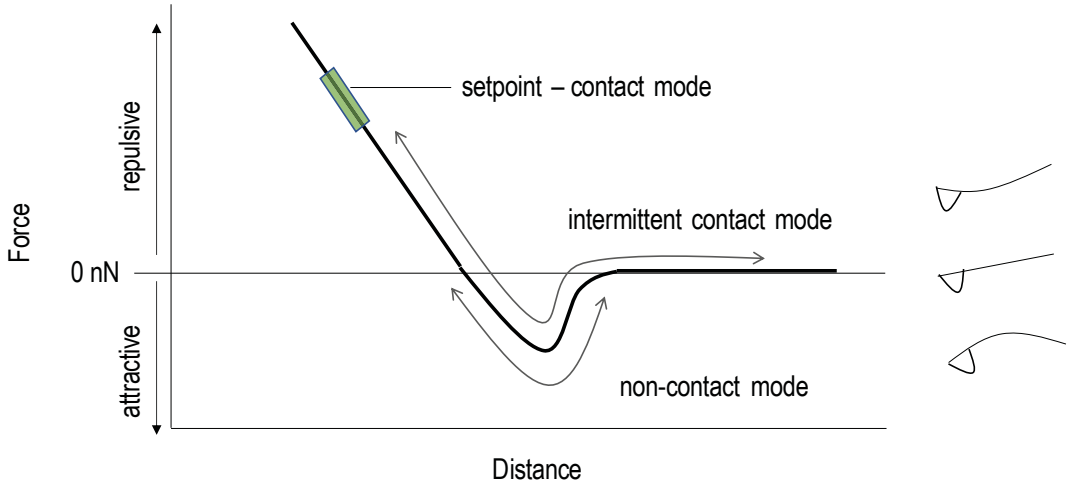

Figure 3.11.: Typical force-distance curve of an AFM probe interacting with a sample. Reproduced from Ref. 63.

Bimodal Dual AC™ Imaging In a bimodal AFM experiment, two resonance frequencies of the cantilever, instead of one, are exited simultaneously. The first, lower mode resonance frequency is used to scan the sample in tapping mode. The amplitude of the cantilever provides the feedback error signal for the topography and the phase yields information on the material contrast. By simultaneously employing a second, higher-order resonance frequency of the cantilever, an enhanced contrast and spatial resolution of the phase image can be achieved.[64] While the technique offers a qualitative indication of a materials properties, the contrast is oftentimes hard to interpret. The bimodal dual AC™ technique is patented by Asylum Research.

Non-topographic modes are used to investigate sample properties other than topography. **Force spectroscopy** is a technique which allows the investigation of the force acting of the probe as it approaches and retraces from the sample. In a force spectroscopy experiment, the deflection of the cantilever is recorded as a function of the position of the Z-sensor of the piezoelectric element. This can be converted into

a force-distance curve. Furthermore, 2D arrays of such curves can be recorded. This quasistatic technique is called force mapping. In this way, nanomechanical properties of samples with elastic moduli between 10 kPa and 100 GPa can be measured. The cantilever spring constant should roughly match the stiffness of the tip-sample contact. The Young's modulus can be determined by fitting the force-distance curve with models such as the Hertz, Sneddon, DMT or JKR model.[63]

Experimental Setup **AFM images** were recorded on an Asylum Research Cypher AFM (Oxford Instruments, Abingdon, UK) in intermittent contact mode. Images under ambient conditions were scanned with AC160TS cantilevers (Olympus) with a nominal spring constant k of 26 N m^{-1} and nominal resonance frequency of 300 kHz. Furthermore, the cantilever OMCL-AC240TS-R2 (Olympus) with nominal k of 2 N m^{-1} and a resonance frequency of 70 kHz were used. Cross sections were analyzed using the Asylum Research/IGOR Pro software.

Nanoindentation measurements were conducted on a MFP-3D AFM (Oxford Instruments, Abingdon, UK) situated in an acoustic enclosure. A CSC-38-A cantilever (Mikromasch) with a nominal k of 0.2 N m^{-1} and a tip radius of $R_{tip} = 8$ nm was used to probe the centre of the particles at 20 °C and 50 °C. For ten microgel particles individual force curves were recorded. The data was fit with the Hertz-model for spherical indenters

$$F = \frac{4E\sqrt{R}}{3(1-\nu^2)}\delta^{(3/2)} \tag{3.8}$$

where F is the force exerted by a sphere of radius R indented into the particle, E the elastic modulus, ν the Poisson ratio and δ the indentation depth. We fitted up to 20% of the maximum indentation to avoid falsifying results due contributions from the hard substrate.

For **fast force mapping** microgel layers on Si-wafers (1 cm x 1 cm) with a low packing density were prepared. PNIPAM microgel dispersions in water with a microgel concentration of 0.02 mg mL^{-1} were spin coated at room temperature. Spin coating was done at 1000 rpm for 300 s. The packing density was briefly evaluated with dry imaging of the wafers.

Fast force maps were recorded on an Asylum Research Cypher ES AFM (Oxford Instruments, Abingdon, UK). We used the BL-AC40TS (Olympus) cantilevers with a nominal spring constant k of 0.09 N m^{-1} and a resonance frequency of 25 kHz in water. Wafers were situated in a fully sealed liquid cell. Water was pumped into the cell and the

temperature was adjusted to 20 °C. 512x512 images with a scan size of 5 μm x 5 μm displaying single particles were recorded. Nanoindentation measurements and fast force mapping were performed by Matthias Kühnhammer at TU Darmstadt.

3.2.4. Ellipsometry

Ellipsometry is an optical, non-destructive method for the analysis of thin films. It uses the change of light polarization upon reflection from a surface to determine material properties such as refractive index n, extinction coefficient k and the film thickness. The incident and reflected beam are described by Jones vectors

$$\vec{E}_{inc} = \begin{pmatrix} |E_p^i|e^{i\delta_p^i} \\ |E_s^i|e^{i\delta_s^i} \end{pmatrix} \qquad \vec{E}_{ref} = \begin{pmatrix} |E_p^r|e^{i\delta_p^r} \\ |E_s^r|e^{r\delta_s^r} \end{pmatrix}. \tag{3.9}$$

E is the amplitude and δ the phase of the light components, the subscripts p and s represent light oscillating within and perpendicular to the plane of incidence respectively, and the subscripts i and r stand for the incident and the reflected light.

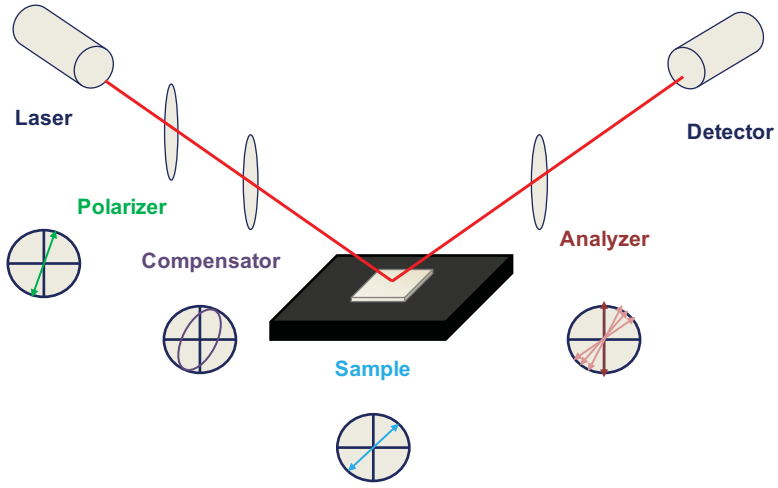

Figure 3.12.: Null-ellipsometry setup with a PCSA (**P**olarizer, **C**ompensator, **S**ample, **A**nalyzer) configuration. Reproduced from Ref. 65.

The two parameters ψ and Δ describe the changes in the state of polarization upon reflection and are defined as

$$\Delta = (\delta_p^r - \delta_s^r) - (\delta_p^i - \delta_s^i) \tag{3.10}$$

and

$$tan\psi = \frac{|E_p^r|/|E_p^i|}{|E_s^r|/|E_s^i|}. \tag{3.11}$$

Δ describes the change in phase and ψ the change in amplitude.

The reflectivity properties are described by the reflection coefficients r_p and r_s

$$r_p = \frac{|E_p^r|}{|E_p^i|} e^{i(\delta_p^r - \delta_p^i)} \qquad r_s = \frac{|E_s^r|}{|E_s^i|} e^{i(\delta_s^r - \delta_s^i)}. \tag{3.12}$$

As orthogonal beams do not interfere, the in-plane and perpendicular components can be treated seperately. The basic equation of ellipsometry is

$$tan\psi \cdot e^{i\Delta} = \frac{r_p}{r_s}. \tag{3.13}$$

Δ and ψ are directly measurable in a null-ellipsometry setup as depicted in Figure 3.12. The PCSA configuration describes the arrangement of the optical components. The polarizer (P) produces linearly polarized light. The light passes the compensator (C), which introduces a defined phase retardation of one field component in reference to the orthogonal one. After interacting with the sample (S), the light passes the analyzer (A) and finally hits the detector. In null-ellipsometry the analyzer rotates in a way that minimizes the detected intensity.[66,67]

Experimental Setup Ellipsometry was measured on a multiscope null-ellipsometer (Optrel GbR, Germany). This instrument is equipped with a green laser (λ = 532 nm) and a PCSA setup. Measurement under ambient conditions were conducted at an angle of incidence α_i of 70°. In order to measure polymer brushes in water, a stainless steel cell was filled with ultrapure water and the sample was placed inside. This setup was mounted onto the sample stage. Water measurements require an angle of incidence of 60°. A copper plate underneath the sample holder was used to adjust the temperature. Since PNIPAM has a VPTT of approximately 32 °C, measurements were conducted between 18 and 50 °C.

All data were fitted with a four-layer model. The first two layers were (i) the silicon substrate with a refractive index n = 4.1520 and an infinite thickness h, and (ii) fused silica with n = 1.4607 and h = 1.5 nm.[68] The third layer was the polymer brush layer.

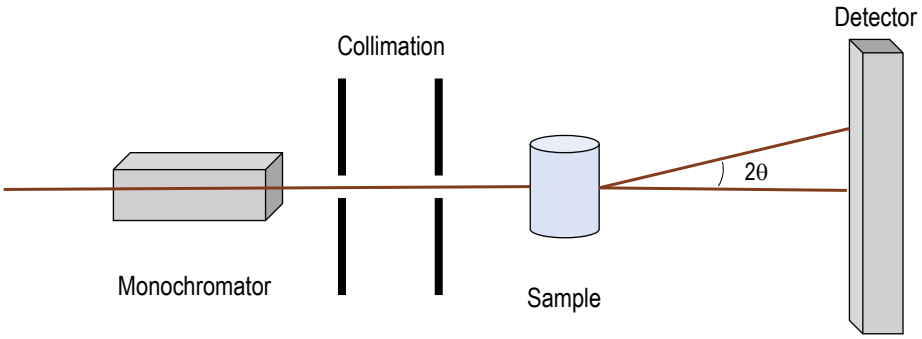

Figure 3.13.: Setup of a SANS experiment. Reproduced from Ref. 70.

For measurements under ambient conditions the refractive index of the polymer brush layer was n = 1.5062,[69] the refractive index of PNIPAM. In case of water measurements, the amount of water present in the PNIPAM layer depends on the temperature and is not constant. Therefore, in these cases the refractive index and the height were fitted. As a rule of thumb, the refractive index in such cases must lie between the refractive indices of pure water and pure PNIPAM. The fourth layer is the medium in which the measurement is carried out. While the height of this layer is infinite, its refractive index in air is $n = 1.00028381$ and in water $n = 1.33370$.

3.2.5. Small Angle Neutron Scattering

Small angle neutron scattering (SANS) is an example of an elastic neutron scattering technique. In a small angle neutron scattering experiment the scattered intensity $I(Q)$ is measured as a function of the momentum transfer Q.[52] For monodisperse spherically symmetric particles the scattered intensity is approximated by

$$I(Q) = (\Delta\rho_v)^2 n V_{pol}^2 P(Q) S(Q), \tag{3.14}$$

with $\Delta\rho_v$ the difference in SLD between solvent and scatterer (in case of this thesis the polymer), n the number density of particles, V_{pol} the volume of polymer within the particle, *P(Q)* the form factor and *S(Q)* the structure factor.

P(Q) describes the interference of radiation from polymer segments within the same particle. *S(Q)*, on the other hand, describes interference of radiation from different particles. In a dilute solution we assume no interference of radiation from different particles

and *S(Q)* can therefore be approximated as 1.

Homogeneous spherical particles can be described by a form factor with a box function

$$P_{hom}(Q) = \left(\frac{3[sin(QR) - QRcos(QR)]}{(QR)^3} \right)^2, \tag{3.15}$$

with R the radius of the sphere.

However, microgel particles prepared by batch polymerization possess a dense core and a fluffy shell. Therefore, Stieger *et al.*[18] convoluted the radial box profile with a Gaussian and derived

$$P_{inho}(Q) = \left[\frac{3[sin(QR) - QRcos(QR)]}{(QR)^3} \cdot exp\left(-\frac{(\sigma_{surf}Q)^2}{2} \right) \right]^2, \tag{3.16}$$

where σ_{surf} describes the smeared particle surface.

Figure 3.14 displays the polymer volume fraction (PVF) of a microgel with a dense core and a fluffy shell as a function of the distance from the particle center. This microgel particle has its highest polymer density in the center up to the radius R_{box}. Above R_{box} the PVF begins to decrease and the radius R, received from a fit of the fuzzy sphere model to our data is $R = R_{box} + 2\sigma_{surf}$. Finally, the radius R_{SANS} obtained by SANS is

$$R_{SANS} = R + 2\sigma_{surf}. \tag{3.17}$$

The polydispersity of microgel particles can be taken into account by assuming the number distribution of the particle radius R to be a Gaussian function[18]

$$D(R, \langle R \rangle, \sigma_{poly}) = \frac{1}{\sqrt{2\pi\sigma_{poly}^2 \langle R \rangle^2}} \cdot exp\left(-\frac{(R - \langle R \rangle)^2}{2\sigma_{poly}^2 \langle R \rangle^2} \right), \tag{3.18}$$

with $\langle R \rangle$ the average particle radius and σ_{poly} the relative particle size polydispersity.

In swollen gel networks spatial inhomogeneities can occur due to an uneven distribution of cross-links. These are often referred to as frozen inhomogeneities and are taken into account by an additional term $I_{inho}(Q)$. Furthermore, network fluctuations are described by I_{fluct},[71] which yields

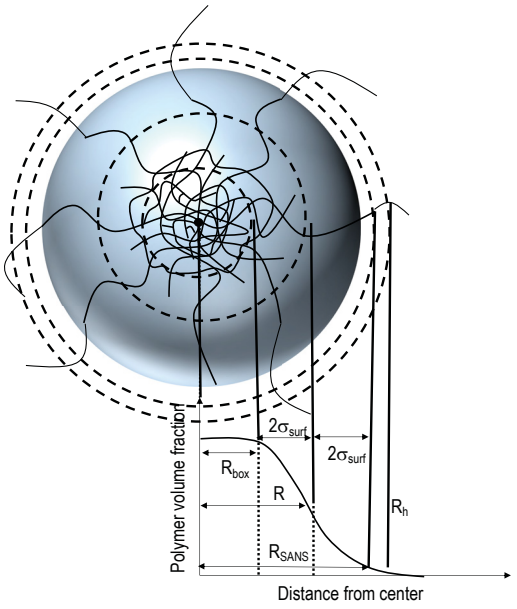

Figure 3.14.: Radial box profile for a "Fuzzy Sphere" microgel. Reproduced from Ref. 18.

$$I(Q) = I_{inho}(Q) + I_{fluct}(Q). \tag{3.19}$$

This can be further expressed as a combination of a Gaussian spatial distribution and an Ornstein-Zernike contribution (Lorentzian function)

$$I(Q) = I_G(0) \cdot \left(-\frac{\Lambda^2 Q^2}{3} \right) + \frac{I_{fluct}(0)}{1 + \xi^2 Q^2} \tag{3.20}$$

with Λ the characteristic length scale of the static inhomogeneities and ξ the correlation length of the network fluctuations, which is related to the blob or mesh size.[18]

Experimental Setup Small angle neutron scattering (SANS) experiments were conducted on the "KWS-2" and "KWS-3" instruments of the Jülich Center for Neutron Science (JCNS) at the Maier-Leibnitz Zentrum (Garching, Germany). KWS-3 covers a Q-range between $3{\cdot}10^{-4}$ and $2.4{\cdot}10^{-3}$ Å^{-1} at a sample-to-detector distance of 9.5 m. KWS-2 can measure Q-values between $1{\cdot}10^{-4}$ and 0.5 Å^{-1} at sample-to-detector distances of 2, 8 and 20 m. The used Hellma quartz cells had a neutron path way of 2 mm. The concentration of the microgel dispersion was 0.001 g$\cdot$ mL^{-1} ($S(Q) \approx 1$) and measurements were carried out at 20 and 50 °C. D_2O was used for bulk contrast. Furthermore, a semidilute solution of linear PNIPAM (30 kDa) with a concentration of 0.05 g$\cdot$ mL^{-1} was measured as a reference.
SANS data were analysed in IGOR Pro using the SANS and USANS Data Reduction and Analysis Software by the NIST Center for Neutron Research (Gaithersburg, MD).

3.2.6. Neutron and X-ray Reflectometry

Reflectometry is a scattering technique that takes advantage of the reflection of light (or neutrons) from the interface of media with different refractive indeces. Neutrons and X-ray radiation are well-suited to characterize thin polymer films, because their short wavelengths correspond to the measured lengths.[72,73]

Neutrons provide some advantages in the study of polymer materials. As neutrons can pass D_2O aqueous polymer solutions can be measured. On the other hand, X-rays from common sources cannot penetrate water and more expensive anode materials would be

needed to generate the suitable wavelength. Therefore, X-ray scattering is more commonly used for measurements of dry samples. Due to the isotope sensitivity of neutrons, it is possible to label parts of a sample, vary or match the contrast between solvent and sample (or parts of the sample). Therefore, homogeneous materials can be characterized and buried interfaces can be made visible.[74]
This chapter will focus on the theoretical description of neutron reflectometry. However, X-ray reflectivity is based on similar principles, with some differences due to the different nature of neutrons and X-rays.

For neutrons the refractive index of a material is defined as

$$n = 1 - \delta - ik, \tag{3.21}$$

where δ is the dispersion in and ik the absorption by the material. Further δ is defined

$$\delta = \frac{\lambda^2}{2\pi}\rho, \tag{3.22}$$

with λ the neutron wavelength and ρ the scattering length density

$$\rho = \sum b_i n_i, \tag{3.23}$$

where b_i is the scattering length of nuclei i and n_i the number of nuclei i per unit volume. The scattering length is characteristic for each atom and, unlike electron density in X-ray scattering, does not follow a predictable trend. It quantifies the scattering of neutrons from a nucleus and is isotope sensitive. The scattering length b_i can assume negative or positive values. An example of two isotopes with very different scattering lengths are hydrogen H and deuterium D. While hydrogen has a negative scattering length, deuterium has a high positive scattering length. This fact is often used for contrast.

Figure 3.15 shows the setup of a neutron reflectivity experiment in specular geometry. The incident angle θ_i equals the angle of reflection θ_f. The wave vectors of the incoming beam k_i and the reflected beam k_f describe the momentum transfer as

$$\vec{Q} = \vec{k_f} - \vec{k_i}, \tag{3.24}$$

and as we assume elastic scattering $|\vec{k_i}| = |\vec{k_f}|$ with $|\vec{k}| = 2\pi/\lambda$ we obtain

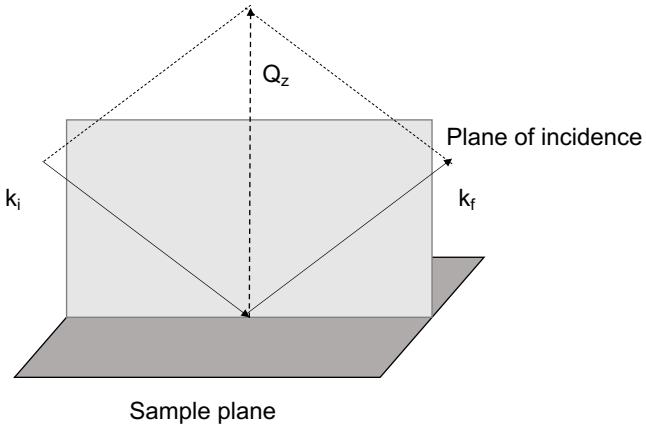

Figure 3.15.: Geometry of a neutron reflectivity experiment. Reproduced from Ref. 75.

$$|\vec{Q}| = Q_z = \frac{4\pi}{\lambda} sin\theta, \tag{3.25}$$

where Q_z is the modulus of the momentum transfer in z-direction and $Q_x, Q_y = 0$.

The reflected intensity I can either be measured at different angles and a constant wavelength or vice versa. The reflectivity R is the normalized intensity

$$R = \frac{I}{I_0}, \tag{3.26}$$

where I_0 is the intensity of the direct neutron beam.

As a result of the constructive and destructive interference of the reflected waves, minima and maxima in the intensity along Q_z are observed (Figure 3.16 a). Furthermore, the total reflected intensity decreases with increasing angle of incidence, because transmission through the material is enhanced. This is called "Fresnel decay" and has a θ_i^4 dependency (hence a Q^4 dependency). These two effects combined result in a typical reflectivity curve as depicted in Figure 3.16 c. The typical oscillations in such a reflectivity curve are called Kiessig fringes and their spacing is related to the distance between two interfaces.[75]

The reflectivity curve can be described as follows. Below the critical angle θ_c there is total reflection of the incoming beam, if the refractive index of the medium from which the beam impinges on the polymer film is lower than the refractive index of the polymer film itself ($n_{film} > n_{medium}$). This is the general condition for total external reflection. Therefore, the reflectivity between 0 and θ_c equals 1. From the critical angle onward the neutron beam is partially reflected and partially transmitted. Therefore, the reflected

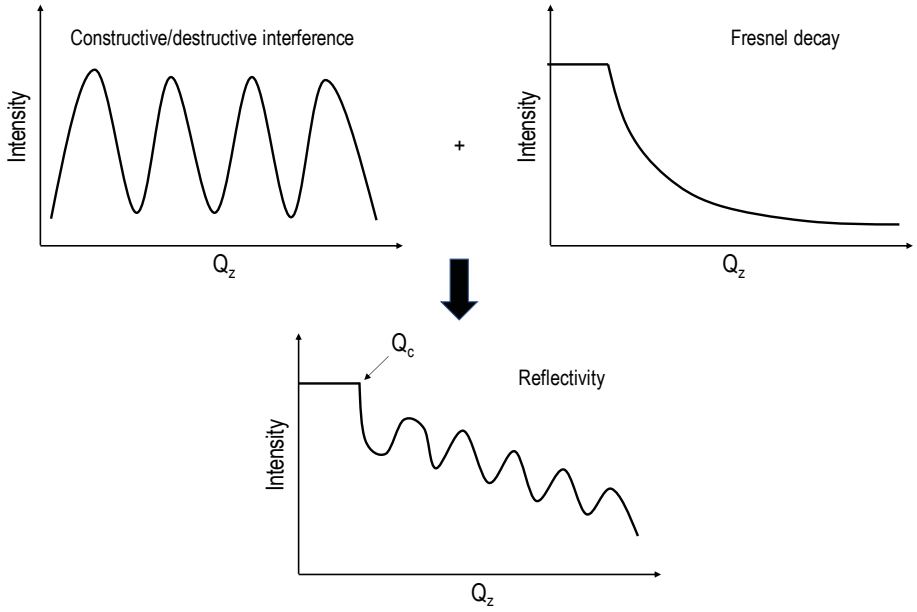

Figure 3.16.: Interference pattern (a) and Fresnel decay (b) yield the reflectivity curve (c).

intensity continuously decreases, displaying more or less pronounced Kiessig fringes.

There are three major factor influencing the form of the reflectivity curve: (I) The critical angle θ_c and therefore the critical wave vector Q_c depend on the refractive index of the medium at which the beam is reflected. The interface between two media can be described by Snell's law $cos\theta_i = n \cdot cos\theta_{trans}$, where θ_i is the angle of incidence and θ_{trans} the angle of the transmitted neutrons. At the critical angle of total external reflection $\theta_{trans} = 0$ and therefore $cos\theta_c = n$. (II) The damping of the decay is related to the roughness of the sample. As the surface is rougher there is more diffuse (off-specular) reflection which results in out of specular geometry scattering and therefore decreases the intensity that reaches the detector. (III) The width of the Kiessig fringes depends on the thickness of the film as the length of one oscillation ΔQ in the reciprocal space is proportional to the layer thickness in real space.[76,77] This is described by Bragg's law

$$2dsin(\theta) = n\lambda, \tag{3.27}$$

and it follows

$$d = \frac{2\pi}{\Delta q_z}. \tag{3.28}$$

Experimental Setup (PNIPAM Microgels) Microgel layers with a high packing density were prepared on 50 mm x 80 mm x 15 mm Si-blocks. PNIPAM microgel dispersions in water with a microgel concentration of 0.25 wt% were spin coated at room temperature. The spin coating parameters were set to 1000 rpm and 100 s. The higher packing density was mainly a result of a higher concentration of microgel particles in the coated dispersion. The packing density was evaluated with light microscopy on a Keyence instrument.

Neutron reflectivity curves of microgels with 10 mol% crosslinker were measured on the TREFF instrument at the Maier-Leibnit Center (Garching, Germany) covering a Q-range of 0.005-0.04 $Å^{-1}$. The neutron wavelength was 4.74 Å. Neutron reflectivity curves were recorded at 20 °C. We recorded neutron reflectivity curves at two contrasts, i.e. in D_2O and H_2O, to facilitate data analysis. Neutron reflectivity curves were fitted with the Motofit package in IGOR Pro.
The data was fitted with a 2-layer model in Motofit. The backing was silicon with an SLD of 2.07 $Å^{-2}$ and infinite thickness. On top of the silicon layer is a silicon oxide layer of approximately 1.5 nm thickness[68] and to have a roughness of approximately 470 pm (AFM, 5μm scan). Adjacent to the silicon oxide layer is the PNIPAM layer. The SLD was taken from the literature as $0.8x10^{-6}$ $Å^{-2}$.[78] The backing was the solvent phase, which for contrast was deuterated water. Deuterated water has an SLD of $6.34x10^{-6}$ $Å^{-2}$.

Experimental Setup (PNIPAM Brushes) Neutron reflectivity curves of PNIPAM brushes were recorded on the magnetic reflectometer with high incidence angle (MARIA) situated at the Maier-Leibnitz Center (Garching, Germany). As we investigate non-magnetic samples, all measurements were conducted in non-polarized beam mode. For low Q-values the neutron wavelength was 10 Å and for high Q-values the neutron wavelength was 5 Å. The wavelength distribution of MARIA is 10 %. We chose to measure at a temperature of 15 °C to ensure the stretched state of the polymer brushes.
All neutron reflectivity curves were fitted with the Motofit package in IGOR Pro.

Two different models were used for the brush with maximum and low grafting density. For the high grafting density brush a three-layer model was used. The first layer is silicon oxide with a scattering length density of $3.47x10^{-6}$ $Å^{-2}$ and a thickness of approximately 1.5 nm.[68] The second layer is the initiator SAM. This layer has an SLD of $0.29x10^{-6}$ $Å^{-2}$ and a thickness of 1.3 nm as measured by spectroscopic ellipsometry. Finally, the third

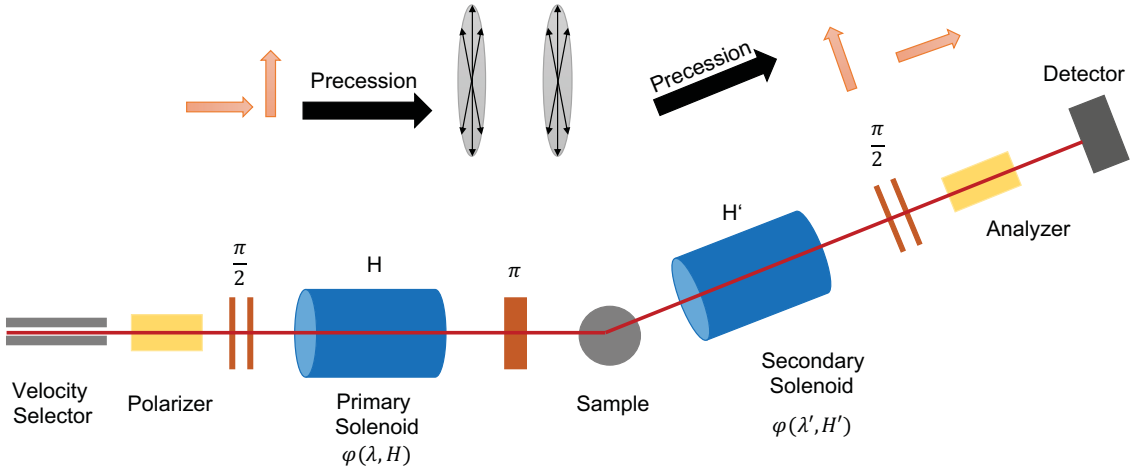

Figure 3.17.: Setup of a neutron spin echo spectrometer.[82,83]

layer is a PNIPAM layer with an SLD of 0.8x10^{-6} Å^{-2}. The thickness of the third layer was fitted. The initial fit guess was derived from ellipsometry measurements.
For the low grafting density brush a four-layer model was assumed. In addition to the three-layer model described above, a fourth layer, consisting of the PNIPAM brush with a higher volume fraction of D_2O toward the solvent phase was added. The SLD of the initiator layer was adjusted to the ratio of initiator and dummy molecules on the surface. More details can be found in Chapter 6 of this thesis.

3.2.7. Neutron Spin Echo Spectroscopy

Neutron spin echo spectroscopy (NSE) is well-suited to study the rather slow dynamics in polymer systems.[79,80] Due to its high energy resolution it grants access to the space and time evolution of segmental diffusion.
These days times up to a few 100 ns can be measured with NSE on large and intermediate length scales. The technique measures energy changes in neutrons due to scattering events, with an energy resolution of up to 10^{-5} and a neutron velocity bandwidth of 20%.[81]
The neutron velocity of the incidenct and scattered neutron beam are compared, taking advantage of the Larmor precession of the neutron spin in an external homogeneous magnetic field.

More precisely the polarization of the neutron beam is measured. Figure 3.17 shows

the typical setup for a neutron spin echo experiment. The primary neutron beam passes a velocity selector, which typically selects a wavelength band of 20%. Afterwards, the neutron beam is polarized in a forward direction and all neutrons are polarized parallel to the beam direction. As the neutron beam passes a so-called $\pi/2$-flipper the neutron spin is flipped by 90° and all neutrons are polarized perpendicular to the beam direction. After entering the primary solenoid the neutron spin begins to precess around the longitudinal field and undergoes ten to hundred thousands of precessions. As the neutrons have different velocities, after exiting the primary solenoid, they will have different precession angles. In close proximity to the sample a π-flipper rotates the neutron spin by 180°. Behind the sample is the secondary solenoid, which is symmetric to the primary solenoid. Assuming that there is no energy exchange with the sample, the number of precessions in the secondary solenoid is equal to the primary. Upon reaching the second $\pi/2$-flipper all neutrons would have the same precession angle, pointing upwards, which is due to the π-flipper. This response is called the spin-echo. The second $\pi/2$-flipper rotates the neutron spin by 90°. An analyzer then transmits only neutrons with spin components parallel or antiparallel to the axis.[80]
If however there is an energy exchange with the sample, a velocity change $\Delta\nu_S$ from the scattering results. Therefore, the downward pointing spins will be rotated to the axially antiparallel direction by the $\pi/2$-flipper and will be blocked by the analyzer, which will result in a reduced echo signal. The cosine of the final precession angle determines the transmission at the detector. The scattering function $S(Q,\omega)$ describes the influence of the sample on the neutrons. Here, ω is the frequency proportional to the energy transfer between neutron and sample.

$$\frac{\omega}{2\pi} = \frac{m_n}{2h}[\nu^2 - (\nu + \Delta\nu_S)^2]. \tag{3.29}$$

The relation between the final polarization P_f and the initial polarization P_i can be expressed as:

$$P_f = P_i \frac{\int_{-\infty}^{+\infty} S(Q,\omega) cos(\omega t) d\omega}{\int_{-\infty}^{+\infty} S(Q,\omega) d\omega}. \tag{3.30}$$

The normalized dynamic structure factor describes the probability that a scattering event occurs at a certain wavelength change

$$\delta\lambda = (m/2\pi)\lambda^3\omega \tag{3.31}$$

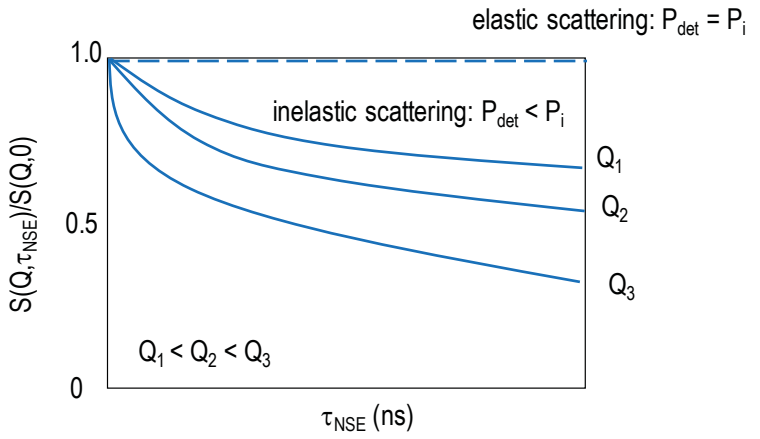

Figure 3.18.: Normalized intermediate scattering functions. A decay is only observed for inelastic scattering.

at a given momentum transfer Q. However, the result of a NSE measurement is the intermediate scattering function $\mathrm{S}(Q, \tau_{NSE})$. A NSE scan is done by variation of the guide field, which leads to a variation in Fourier time.[80]

$$\tau_{NSE} = 1.863x10^{-14} HL\lambda^3 \tag{3.32}$$

The intensity that reaches the detector is

$$I_{Det} \propto \frac{1}{2}[S(Q) \pm \int cos(J\lambda^3\gamma \frac{m_n^2}{2\pi h^2}\omega) S(Q,\omega) d\omega] \tag{3.33}$$

with $J = \int_{path} |B| dl$ the integral if the magnetic induction along the flight path of the neutron, and $\gamma = 1.83033x10^8$ radian/sT. Therefore, the detected intensity strongly depends on the strength of the magnetic field and the neutron wavelength. However, at higher magnetic fields, inhomogeneities in the magnetic field will affect the measurement more. Furthermore, the maximum Fourier time depends on

$$\tau_{NSE} = J\lambda^3\gamma \frac{m_n^2}{2\pi h^2}. \tag{3.34}$$

Therefore, the maximum achievable Fourier time is limited by the neutron wavelength and the magnetic field.[79,80]

A schematic representation of different intermediate scattering functions (ISFs) is displayed in Figure 3.18. The dashed line represents a purely elastic scattering event, where no decay is observed and the polarization at the detector P_{det} equals the initial

polarization P_i. The three solid lines represent inelastic scattering at different Q-values, where P_{det} is smaller than P_i. With increasing Q the decay becomes more rapid over τ_{NSE}.

Experimental Setup ISFs of PNIPAM microgels were recorded at the SNS-NSE at the spallation neutron source at the Oak Ridge National Laboratory in Tennessee, USA. Combination of two neutron wavelengths (8 and 11 Å) allows coverage of a wide range of Fourier times between $\tau_{NSE} = 0.04$ and 95 ns (s. Figure A.5). The Hellma quartz cells for NSE experiments had a neutron path way of 3 mm. To suppress center-of-mass diffusion the microgel concentration was 8 wt%. All measurements were conducted in D_2O at 20 °C to ensure the swollen state of the microgel network.
Furthermore, a semidilute solution of linear PNIPAM (30 kDa) was measured. The concentration was chosen due to results from viscosimetry. The viscosity in D_2O as a function of the polymer concentration was measured with a Lauda iVisc glass capillary viscometer (LAUDA Scientific, Germany). The efflux time t was measured with micro-Ostwald-viscometers (type I and Ic), suited for different viscosity ranges. Samples sat in the temperature bath for 10 minutes prior to the measurement for thermal equilibration. Results are the average over five measurements. As Ostwald-viscosimetry measures the kinematic viscosity $\nu = \eta/\rho$, the polymer solution density had to be measured as well. The polymer solution density was measured with an Anton Paar DMA 4500 density meter (Anton Paar, Austria).

3.2.8. Grazing Incidence Scattering

Grazing incidence scattering circumvents issues with low intensities due to extremely small sample volumes in the investigation of thin films. It yields average statistical information over a large illuminated area and allows the investigation of buried structures without any damage to the sample. Furthermore, the technique is surface sensitive and allows a variation of the probed depth of the sample layer.[84,85]

In grazing incidence scattering a shallow angle of incidence α_i is chosen. If we take a look at the detector image, we observe a bright peak where $\alpha_i = \alpha_f$, which arises from specular scattering and is therefore called the specular peak (S) (s. Figure 3.19). For an incident angle α_i which equals the critical angle of total external reflection α_c a second peak, the so-called Yoneda-peak (Y) is observed. In Figure 3.19 it is shown that the

sample defines the (x, y) plane and that the neutron beam is directed in x-direction. The scattering plane is defined by the (y, z) plane and the scattering vector has the components

$$\vec{Q} = \vec{k}_f - \vec{k}_i = \frac{2\pi}{\lambda} \begin{pmatrix} \cos(\alpha_f)\cos(\theta_f) - \cos(\alpha_i) \\ \cos(\alpha_f)\sin(\theta_f) \\ \sin(\alpha_f) + \sin(\alpha_i) \end{pmatrix}. \tag{3.35}$$

The Q_y component probes lateral structures and dynamics. Therefore, the Q_y resolution is essential in grazing incidence scattering techniques, especially GISANS, and a point-shaped neutron beam is generated by using slits in the collimation section.

The refractive index is described by equation 3.21, and the dispersion δ and absorption β are described by

$$\delta(\vec{Q}, \lambda) = \frac{Nb\lambda^2}{2\pi} \tag{3.36}$$

and

$$\beta(\lambda) = \frac{N\alpha_a\lambda}{4\pi}, \tag{3.37}$$

with N the atomic number density, b the scattering length and α_a the absorption cross-section for neutrons. The product Nb is the scattering length density ρ. A beam-stop is used to prevent damaging of the detector by the direct beam.

The critical angle of total external reflection depends on the scattering length density of the polymer under investigation and is

$$\alpha_c = \lambda\sqrt{\frac{\rho_P}{\pi}}. \tag{3.38}$$

The Yoneda peak results from diffuse scattering due to surface and inner roughness of the sample and has its maximum at α_c. As very small angles are used in grazing incidence scattering, the lateral structure in y-direction and the structure perpendicular to the surface (z) are probed, because $Q_x << Q_y, Q_z$.

As mentioned above with grazing incidence scattering, the probed depth can be varied as well.

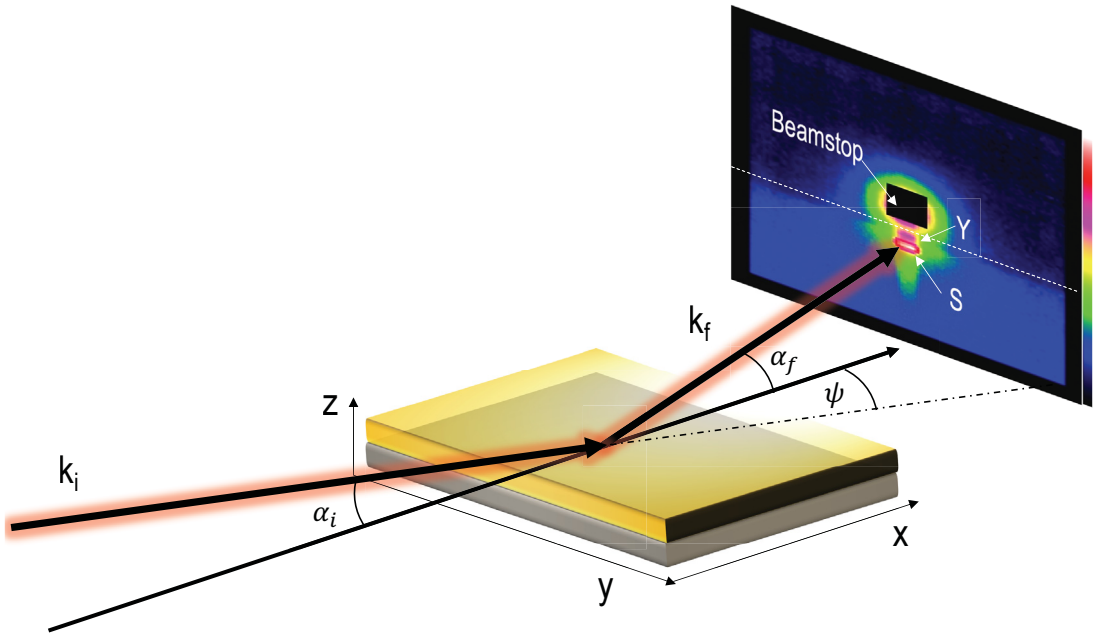

Figure 3.19.: Geometry of a grazing incidence scattering experiment. Reproduced from Ref. 85.

$$D = \frac{\lambda}{\sqrt{2}\pi(l_i + l_f)}, \tag{3.39}$$

with

$$l_{i,f} = \left[\sin^2\alpha_c - \sin^2\alpha_{i,f} + \sqrt{(\sin^2\alpha_{i,f} - \sin^2\alpha_c)^2 + \left(\frac{\mu\lambda}{2\pi}\right)^2}\right]^{1/2}. \tag{3.40}$$

Therefore, in order to measure surface near and bulk dynamics it is sensible to measure at multiple different angles of incidence namely (1) $\alpha_i < \alpha_c$ (surface near) and (2) $\alpha_i > \alpha_c$ (bulk). This is illustrated in Figure 3.20. However, limited angular and wavelength resolution in neutron scattering result in a smearing of the scattering depth. This makes measurements at angles close to α_c problematic and therefore limits the detectable variation in the dynamics profile at the interface.

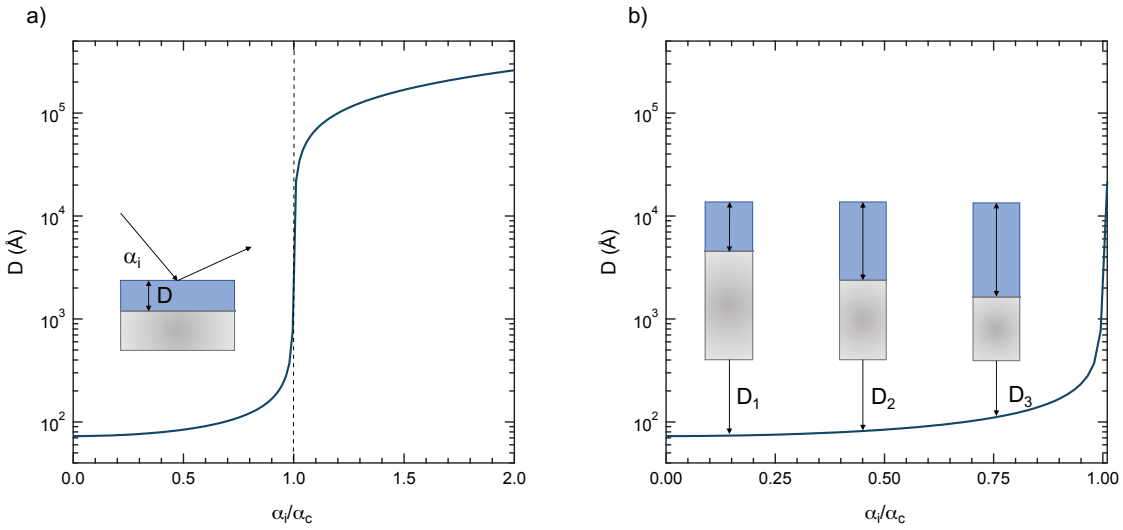

Figure 3.20.: Neutron penetration depth as a function of the angle of incidence α_i. Reproduced from.[85]

3.2.9. Grazing Incidence Neutron Spin Echo Spectroscopy

Grazing incidence neutron spin echo spectroscopy (GINSES) combines classical neutron spin echo spectroscopy with grazing incidence scattering. The technique therefore allows observation of thermal fluctuations of macromolecules close to rigid, planar interfaces. Examples for such systems are polymer brushes,[86] adsorbed microgel particles,[87] microemulsions[88] or hydrogel films.

Under certain conditions an evanescent field is generated which then travels parallel to the surface. It can penetrate the sample perpendicular at a penetration depth between 10 and 100 nm. The method is sensitive to thermal fluctuations close to the interface, and thermal fluctuations can be measured as a function of the distance to the interface as well. Due to the orientation of the sample cell and that of Q_{GINSES} the y-component is rather small and the technique is sensitive to fluctuations perpendicular to the interface. GINSES can be measured on a standard NSE spectrometer. However, the entrance and sample aperture are set to approximately 2 mm. The collimation in combination with a small sample volume in a thin film leads to a loss in intensity of several orders of magnitude compared to standard experiments in transmission. Therefore, GINSES experiments require a stable instrument and low background.[89]

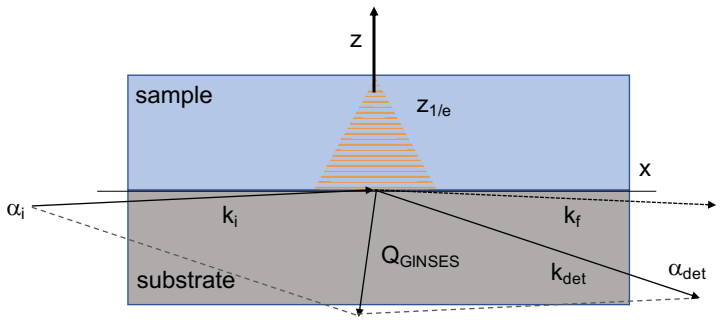

Figure 3.21.: Geometry of a grazing incidence neutron spin echo spectroscopy experiment. The neutron beam impinges the substrate under the angle of incidence α_i below the critical angle of total external reflection α_c (not shown). This generates an evanescent field, which decreases in intensity over z. The penetration depth $z_{1/e}$ describes the z-position where the intensity has decreased to 1/e. The scattered neutrons are detected at α_{det}. Because $\alpha_{det} >> \alpha_i$ the momentum transfer $Q_{GINSES} = k_{det} - k_i$ has an in-plane component. Still, the z-component is probed, as the in-plane component in negligible.[86]

Experimental Setup (PNIPAM Brushes) ISFs of PNIPAM brushes were measured on the J-NSE spectrometer at the Maier-Leibnitz Center (Garching, Germany). Measurements had to be conducted during two separate beam times due to capacity issues. During the first beam time, the sample with a maximum grafting density was measured. Diffraction scans were conducted at a neutron wavelength of 6 Å to determine the ideal Q-value. An ideal Q-value combines a high count of coherently scattered neutrons with a comparatively low count of incoherently scattered neutrons. Measurements were carried out at $Q = 0.08$ Å^{-1}. In between the two beam times the instrumental setup was altered and superconducting magnetic coils were installed. Therefore, during the second beam time the parameters were slightly altered. All remaining measurements were conducted at a neutron wavelength of 8 Å. The corresponding diffraction scans show the best ratio between coherent and incoherent scattering at a Q-value of 0.06 Å^{-1}. Due to the instrumental changes the Fourier time covered during the second beam time could be extended from $\tau_{NSE} = 0.5$ - 40 ns to $\tau_{NSE} = 0.5$ - 60 ns. Measurements were conducted in D_2O at 15 °C (good solvent conditions).

Experimental Setup (PNIPAM Microgel Particles) GINSES measurements of adsorbed PNIPAM microgel particles were conducted on the J-NSE instrument at the Maier-Leibnitz Center (Garching, Germany). To determine the ratio between coherent

and incoherent scattering contribution to the spin echo at a neutron wavelength of 6 Å, diffraction scans were recorded prior to sample measurement. A Q-value of 0.06 $Å^{-1}$ was chosen and intermediate scattering functions were recorded for Fourier times between $\tau_{NSE} = 0.5$ and 35 ns. Based on the critical angle of total reflection as determined from neutron reflectivity curves, an angle of incidence below the critical angle of total reflection ($\alpha_{i,1} = 0.2°$) and an angle of incidence above the critical angle of total reflection ($\alpha_{i,2} = 1.0°$) were measured. Therefore, two different neutron penetration depths are covered by the measurements. As a comparison, a bare Si-block was measured against D_2O. The apeture was set to 2 mm.

BornAgain Simulations Simulations of the intensity map of the evanescent intensity at $\alpha_{i,1} = 0.2°$ were simulated with BornAgain.[90] Simulations were based on the neutron reflectivity curves. For the simulations of the adsorbed microgel particles a form factor for a truncated sphere was assumed. The Ornstein-Zernike correlation length was adopted from SANS bulk measurements of the particles in bulk. A vertical cut through the intensity map of the evanescent field allows us to determine the neutron penetration depth more exact. The neutron penetration depth is defined as the depth were the intensity of the evanescent field has decreased to 1/e. Furthermore, the background was simulated to better estimate the contribution of the background to the signal. BornAgain simulations were conducted by Dr. Tetyana Kyrey.

4. Microgels Prepared by Batch and Continuous Monomer Feeding Method

Abstract

In colloid science, poly(*N*-isopropylacrylamide) based microgels prepared by precipitation polymerization in a batch reactor have been studied extensively. Recently, the inhomogeneous network morphology of such microgels has inspired the development of continuous feeding methods, which result in a more homogenous radial polymer density profile. However, no systematic analysis of how the internal structure of such microgels in bulk translates to the adsorbed state has been attempted so far. In this chapter, we analyze the swelling behavior and look at the adsorption on solid surfaces for microgels prepared with low, medium and high molar fractions of cross-linker by both the batch and a continuous monomer feeding method. For this purpose, experiments such as liquid chromatography mass spectrometry, dynamic light scattering and atomic force microscopy imaging were combined to compare batch-and feeding-microgels. This will help to understand how feeding-microgels behave differently from their batch counterparts and to indicate their suitability for surface applications.

4.1. Introduction

The internal structure and dynamics of microgel particles are influenced by the chosen preparation method. In a conventional batch method (Figure 4.1**a**) the cross-linker BIS is incorporated into the network at a higher rate than the monomer NIPAM.[17] This results in a dense, highly cross-linked core, which is surrounded by dangling polymer chains. A more homogeneous network can be accomplished with the continuous monomer feeding method (Figure 4.1**b**).[23]

The internal structure and dynamics are important for the loading capability to incorporate guest-molecules and guest-particles into the polymer network. An example for guest-particles are magnetic nanoparticles (MNPs). Witt *et al.* studied the distribution and loading capability of batch- and feeding-microgels with MNPs. They found that while the MNPs were mainly located in the outer shell of batch-microgels, they were more evenly distributed in the feeding-microgel particles. Furthermore, the more even distribution of cross-links led to a higher overall loading capability.[53] Another example for the incorporation of guest molecules into microgel networks is the immobilization of enzymes. Gawlitza *et al.* immobilized horse radish peroxidase in PNIPAM microgels to use the water-soluble enzyme in organic media.[91] The loading capability is related to the mesh size of the polymer network. The mesh size needs to be compatible with the size of the guest particle or molecule.

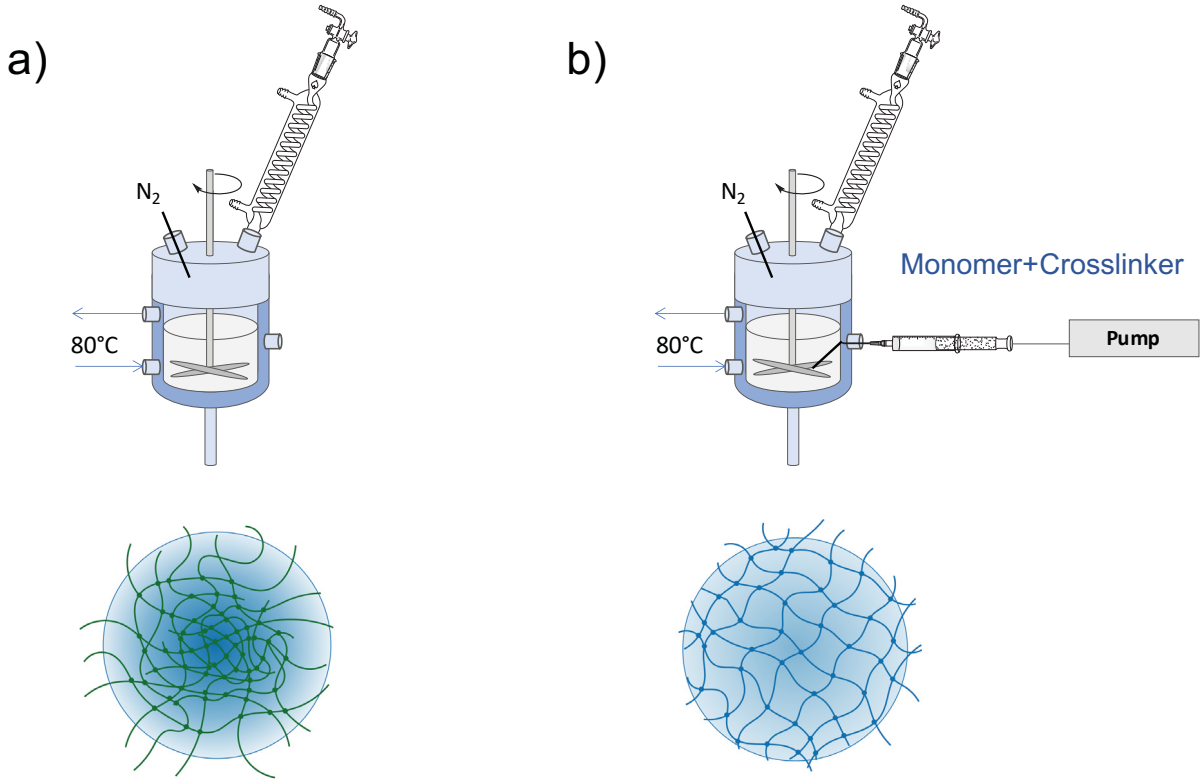

Figure 4.1.: Different setups for surfactant-free precipitation polymerization: a) batch method and b) continuous monomer feeding method. In the bottom the anticipated network morphology is displayed.

Another parameter that influences the mesh size is the degree of cross-linking. The

degree of cross-linking can be varied by the amount of cross-linker that is used during precipitation polymerization. A higher degree of cross-linking has shown to result in a smaller mesh size.[92] Furthermore, it has been shown that the dynamic properties of the network are influenced by the degree of cross-linking. Hellweg *et al.* investigated the internal dynamics of PNIPAM-based batch-microgels and found a decrease of the collective diffusion coefficient with increasing cross-linking.[93]

In this chapter, PNIPAM microgel particles with 2, 5 and 10 mol% BIS were prepared by the conventional batch method and by the continuous monomer feeding method. Their swelling behavior and the influence of adsorption on a solid planar surface were studied and compared. For this, dynamic light scattering and atomic force microscopy imaging were employed. The overarching goal of this chapter was to identify particles suitable for further studies of the dynamics and nanomechanics of adsorbed microgel particles.

4.2. Results

In the first part of this section, properties of batch- and feeding-microgels in the bulk phase with varying degrees of cross-linking are characterized and compared to each other. First, the polymerization kinetics are investigated with liquid chromatography mass spectrometry (LC-MS). Secondly, the difference in optical transmission is shown and thirdly, the microgels' temperature-dependent swelling behavior is investigated with dynamic light scattering (DLS). In the second part, microgel particles were coated onto solid substrates. The particle profile in the adsorbed state was extracted from AFM topography images to compare aspect ratios in the dry and swollen adsorbed state. This yields information about the particles' swelling capability after adsorption and the influence of the confining surface.

4.2.1. Polymerization Kinetics

The conversion of microgels prepared with the batch method can be calculated from LC-MS measurements. This is possible, because all reactants are present in the reactor at a polymerization time of $t_p = 0$ and are consumed over t_p. Figure 4.2**a** shows the consumption of NIPAM and BIS in a conventional batch method for polymerization

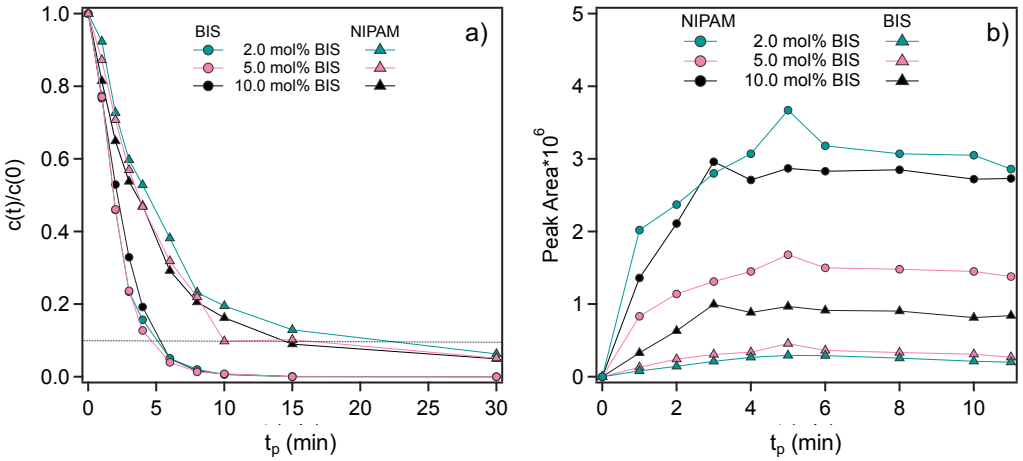

Figure 4.2.: a) Conversion c(t)/c(0) against the polymerization time t_p between 0 and 30 min for the conventional batch method. The dashed line indicates a total consumption of 90% of the initial concentration c(0). b) Peak areas determined from LC-MS measurements of samples removed from the continuous monomer feeding method. After a short initiation period ($\approx$ 3 min) the concentration remains constant.

times t_p between 0 and 30 min. In all cases, the consumption of BIS is significantly faster than the consumption of NIPAM. Overall, after 5 to 6 min 90% of BIS are consumed regardless of the initial cross-linker concentration (indicated by the dashed horizontal line), whereas 85 to 90% of NIPAM are consumed after 15 min. The slopes of linear fits between $0 \leq t_p \leq 3$ min yield the conversion rates ω_{NIPAM} and ω_{BIS} according to $\omega = a \cdot c_0$. The degree of cross-linking in the core x_{core} can be calculated according to

$$x_{core} = \frac{\omega_{BIS} \cdot 100\ \%}{\omega_{BIS} + \omega_{NIPAM}}, \tag{4.1}$$

assuming that the core was already formed after 3 minutes. The degree of cross-linking of the shell is

$$x_{shell} = \frac{c_{BIS,shell} \cdot 100\ \%}{c_{BIS,shell} + c_{NIPAM,shell}} \tag{4.2}$$

$$= \frac{(c_{0,BIS} - 3\ min \cdot \omega_{BIS}) \cdot 100\ \%}{(c_{0,BIS} - 3\ min \cdot \omega_{BIS}) + (c_{0,BIS} - 3\ min \cdot \omega_{NIPAM})}. \tag{4.3}$$

Table 4.1.: Results from linear fits to the conversion of NIPAM and BIS during the batch precipitation polymerization.

mol% BIS	a_{NIPAM} **(min^{-1})**	ω_{NIPAM} **(mM/min)**	a_{BIS} **(min^{-1})**	ω_{BIS} **(mM/min)**	x_{core} **(mol%)**	x_{shell} **(mol%)**
2.0	-0.14	17.19	-0.26	0.65	3.6	0.75
5.0	-0.15	17.30	-0.26	1.64	8.7	1.98
10.0	-0.16	17.46	-0.23	2.81	13.9	6.3

The results indicate a significant difference between the theoretical degree of cross-linking in the core and shell (s. Table 4.1). While the calculated core cross-linker density is higher than expected, the shell cross-linker density is lower. This is in agreement with the formation of a highly cross-linked particle core. For a batch microgel with a theoretical cross-link density of 2 mol% calculations according to equation 4.1 yield a core cross-link density of x_{core}=3.6 mol% versus a shell cross-link density of x_{shell}=0.75 mol%. This means that the differences between the theoretical and experimental cross-link density are 63 to 80 % For the highest initial cross-link density of 10 mol% this difference is less pronounced with a cross-link density of x_{core}=13.9 mol% and a shell cross-link density of x_{shell}=6.3 mol%. This is a difference of 37 to 39 %.

Unfortunately, the conversion of BIS and NIPAM in a continuous monomer feeding method could not be determined in the same manner. Figure 4.2**b** shows the peak area determined from LC-MS spectra over the polymerization time t_p of a continuous monomer feeding polymerization. The first sample for LC-MS measurements was removed from the reaction after 1 minute. Between t_p =1 min and t_p = 3 min an increase in the peak area of both reactants is observed. This means an increase in the concentration of the reactants. Afterwards, the peak areas remain at a constant, low value. Therefore, in $\omega_{BIS/NIPAM} = a * c_0$ the parameters a and c_0 are zero. However, this does not mean that there is no conversion, but that the conversion happens quickly. The initial increase can be explained by the fact that in the beginning of the reaction there is a very low concentration of reactants, which means a low probability of initiation and propagation. As more reactants are fed into the reactor, continuous polymerization occurs and the peak area remains constant. Therefore, in the future it is recommended to use *in situ* methods track the conversion of feeding methods.

4.2.2. Optical Properties

Figure 4.3 shows dispersions of batch- and feeding-microgels (c_{MG}=0.5 wt%) prepared with the same molar fractions of BIS. A difference in the turbidity of the microgel dispersions is apparent by optical observation already.

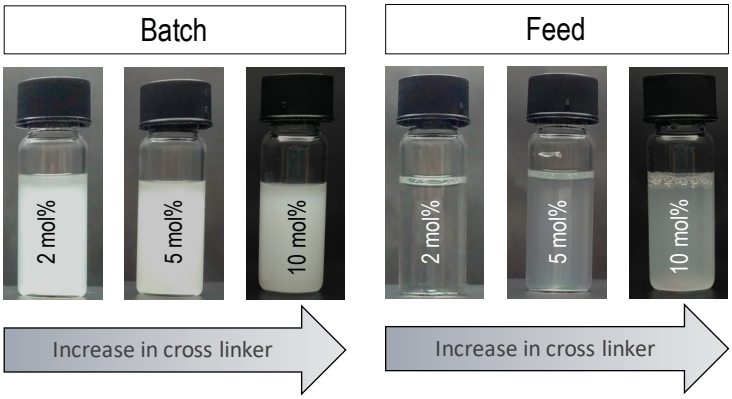

Figure 4.3.: Dispersions of PNIPAM microgels (c_{MG} = 0.5 wt%) with different cross-linker content prepared by the continuous monomer feeding method and the batch method.

The transmittance of a HeNe-laser beam with a wavelength of λ = 632.8 nm and a power of 5 mW through microgels from the conventional batch method and the continuous monomer feeding method was measured to quantify the microgels' turbidity. First, the transmitted intensity of the cuvette (2mm) filled with water (I_0) was measured. Afterwards, the microgel dispersions were filled into the cuvette and the corresponding intensity I was measured. The transmittance was calculated according to

$$\%T = \frac{I}{I_0} \cdot 100\%. \tag{4.4}$$

As the degree of cross-linking increases the transmittance decreases for both types of microgels (Figure 4.4). The batch-microgels have a lower overall transmittance compared to the feeding-microgels. For instance a batch-microgel with a degree of cross-linking of 2 mol% has a transmittance of T = 69%, while the corresponding feeding-microgel transmits 98% of the light. This difference can be explained by the lower scattering cross-section for light, leading to a lower scattered light intensity.

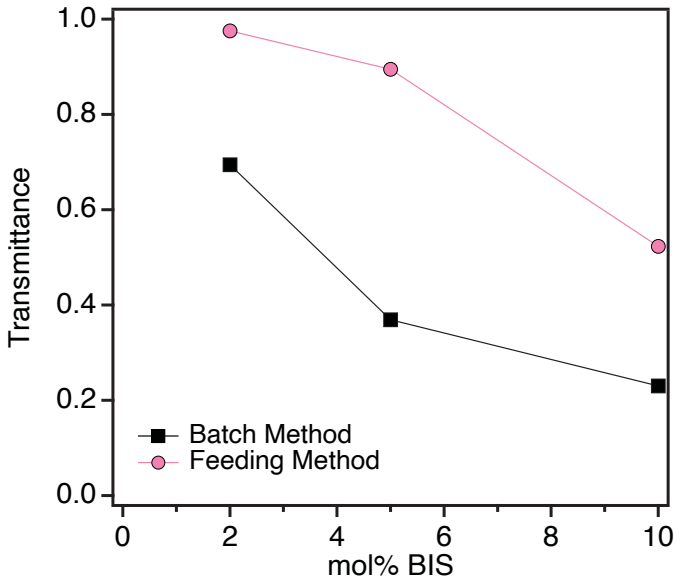

Figure 4.4.: Transmittance of PNIPAM microgel dispersions ($c_{MG} = 0.5$ wt%) with different cross-linker content prepared by the continuous monomer feeding method and the batch method.

4.2.3. Swelling in the Bulk Phase

First, microgels prepared with a molar fraction of cross-linker between 2 and 10 mol% were synthesized with the conventional batch method. Figure 4.5**a** displays the hydrodynamic radius as a function of the temperature. The microgel particles display the typical thermoresponsive behavior with a reversible VPT around their VPTT. At this temperature the microgel particles collapse to the hydrodynamic radius they possess during polymerization. While all microgels were polymerized under indentical conditions, an increasing molar fraction of cross-linker results in a higher hydrodynamic radius at elevated temperatures.

The swelling ratio $\alpha_{20°C} = \frac{R_{h,20°C}}{R_{h,50°C}}$ (Figure 4.5**b**) helps to further characterize the microgels' swelling behavior. As the molar fraction of cross-linker increases, the swelling ratio decreases. This can be attributed to the fact that a denser polymer network is less flexible and the magnitude of the displacement vector of the network is smaller.[94] This in turn negatively affects the interaction with solvent molecules. The microgel with the lowest amount of cross-linker swells more than twice as much as the microgel with the highest amount. For orientation, the swelling ratios at 20 °C are displayed in Table 4.2.

In Figure 4.5**c** the first derivative of the hydrodynamic radius in reference to the

Table 4.2.: Swelling ratios of PNIPAM batch- and feeding-microgels at T=20 °C.

Cross-linker (mol%)	$\alpha_{\mathbf{20°C,\ batch}}$	$\alpha_{\mathbf{20°C,\ feeding}}$
2.0	3.7	–
5.0	2.6	3.1
10.0	1.7	2.2

temperature is displayed and fitted with a Gaussian. This illustrates two properties of the thermoresponsive behavior of the microgels. First, the width of the Gaussian gives information on the broadening of the VPT. As the degree of cross-linking increases we observe that the width increases. This corresponds to a broader transition. For those microgels with a low degree of cross-linking we observe a rather abrupt VPT. Second, we can determine the VPTT from the x-value at the minimum of the Gaussian fit. The VPTT increases with increasing cross-linker content at values between 31 and 34 °C (s. Table 4.3).

In a second step, microgels in the same size range were prepared by a continuous monomer feeding method. In Figure 4.6**a** the hydrodynamic radii of those feeding microgels with 2 to 10 mol% BIS are displayed. It becomes apparent that the radii after polymerization are similar to their batch counterparts. However, the feeding microgels have higher swelling ratios $\alpha_{20°C}$ (Figure 4.6**b**) and therefore reach higher hydrodynamic radii at lower temperatures. In general, the trend that the swelling ratio decreases with increasing cross-linker content applies to feeding-microgels too. The VPTTs for feeding-microgels were determined from the first derivative of the hydrodynamic radius in reference to the temperature as well. While the values are comparable to those of batch-microgels, feeding microgels have a slightly higher VPTT ($\Delta T \approx 2°$) for the same initial molar fraction of cross-linker. However, DLS of the feeding-microgels with 2 mol% BIS did not result in spherical objects of radii in the same range. The relaxation rates of those microgels were graphed against Q^2 and Q^3 and are shown in Figure 4.7. This plot shows that the relaxation rates Γ of the lowly cross-linked feeding-microgels are better described by Q^3-dependent behavior. This indicates the observation of segmental Zimm-type dynamics. However, from a second order cumulant analysis we are able to obtain spherical structures with hydrodynamic radii of 30 to 40 nm. These findings will be discussed in more detail towards the closing of this chapter.

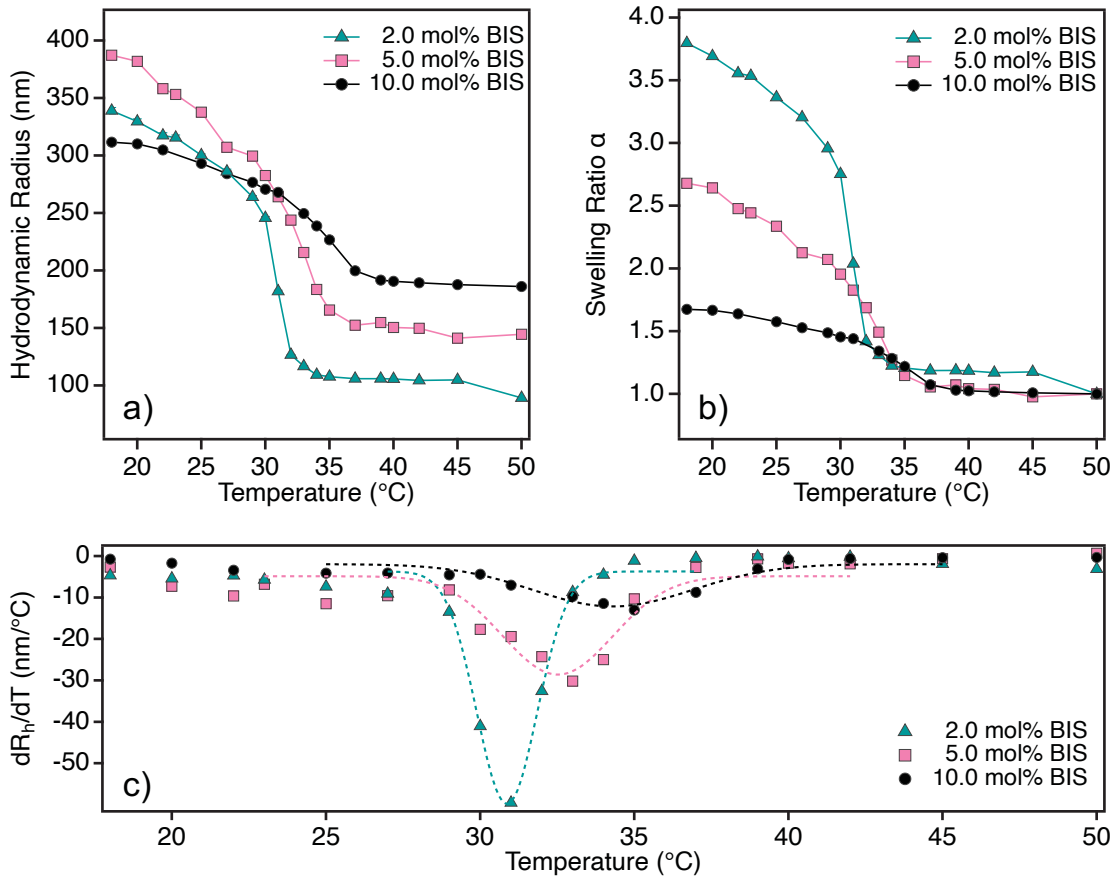

Figure 4.5.: Temperature-dependent properties of microgel particles prepared with different molar fractions of cross-linker between 18 and 50 °C synthesized with the **batch method**. a) hydrodynamic radius, b) swelling ratios, c) first derivative of the hydrodynamic radius in reference to the temperature.

Table 4.3.: VPTT of PNIPAM batch- and feeding-microgels.

Cross-linker (mol%)	**$VPTT_{batch}$ (°C)**	**$VPTT_{feeding}$ (°C)**
2.0	30.9±0.1	–
5.0	32.5±0.3	34.3±0.6
10.0	34.3±0.4	36.1±0.2

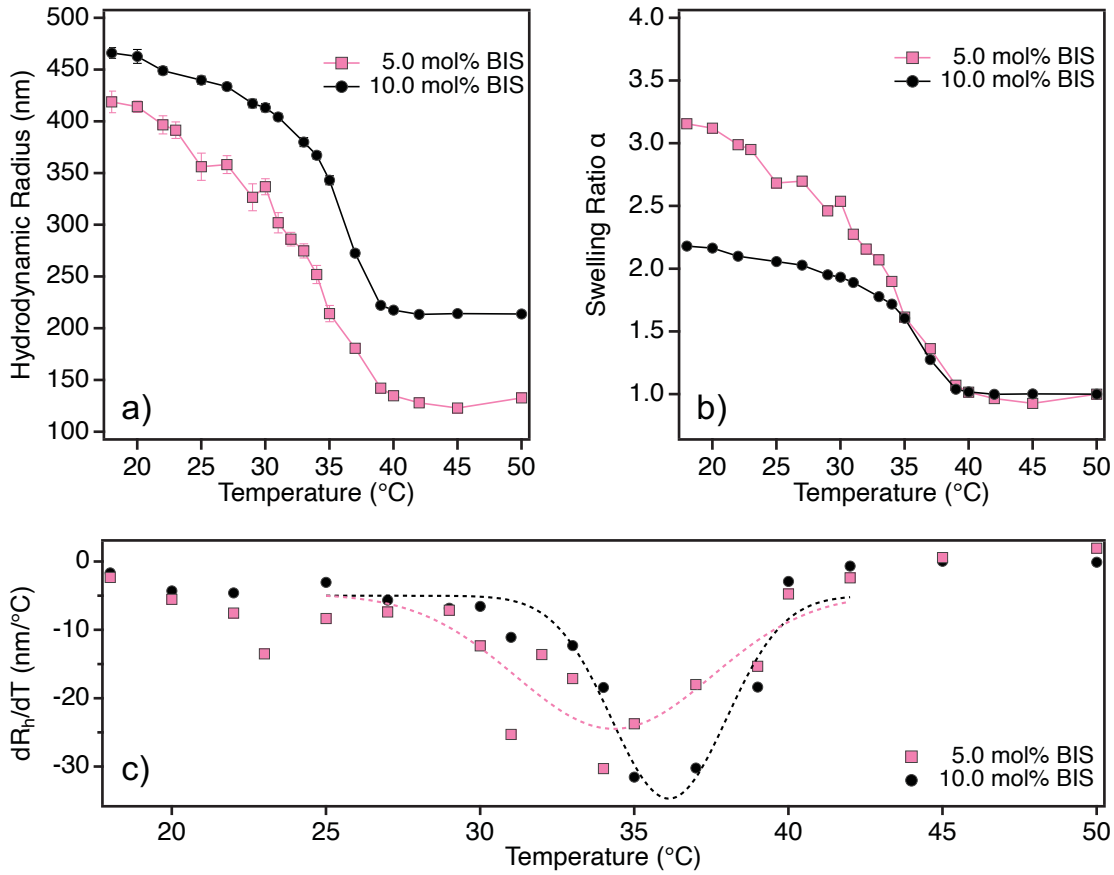

Figure 4.6.: Temperature-dependent properties of microgel particles with different cross-linker content between 18 and 50 °C synthesized with the **continuous monomer feeding method**. a) hydrodynamic radius, b) swelling ratios, c) first derivative of the hydrodynamic radius in reference to the temperature.

4.2.4. Properties of Adsorbed PNIPAM Microgels

In this section, AFM imaging of the previously investigated PNIPAM-based batch- and feeding-microgels is presented. Dilute dispersions of the investigated microgels were spin coated onto silicon wafers to investigate individual particles in the adsorbed state.
AFM topography images in air and in water at 20 °C show the different adsorption properties (s. Figures 4.8 and 4.9). All batch-microgels are shaped like spherical domes after adsorption to solid planar surfaces. However, they differ in their aspect ratios in the ambient and swollen state. In the ambient state, batch-microgels with 2 and 5 mol% BIS have relatively high aspect ratios (w/h) of 13.7 and 19.6, respectively. This means that they lie relatively flat on the solid planar surface. In case of 10 mol%, however, the aspect ratio is slightly lower with 4.6. Those particles therefore appear to contain their spherical shape better after adsorption. In the swollen state the aspect ratios of all batch-microgels decrease and particles swell both vertically and horizontally in relation to the surface.
The feeding-microgels have unusually high aspect ratios. This is due to their strong deformation upon adsorption to the solid surface. This results in very low height values and a comparatively high width. Again, in the swollen state the aspect ratios of the feeding-microgels decrease, but remain relatively high. The unusually high aspect ratios of feeding-microgels can be explained by their network structure. While batch-microgels have a highly-crosslinked core, in feeding-microgels the distribution of cross-links is more even. The core serves as a stabilizing structure for the microgels upon adsorption comparable to a scaffold.
The fact that lowly cross-linked feeding-microgels show no distinctly spherical objects in AFM topographies is in agreement with our findings from DLS. The spherical objects with a hydrodynamic radius of 30 - 40 nm are hardly recognizable in topographies in water. Those structures are too flat against the surface to distinctly visualize them with the AFM.

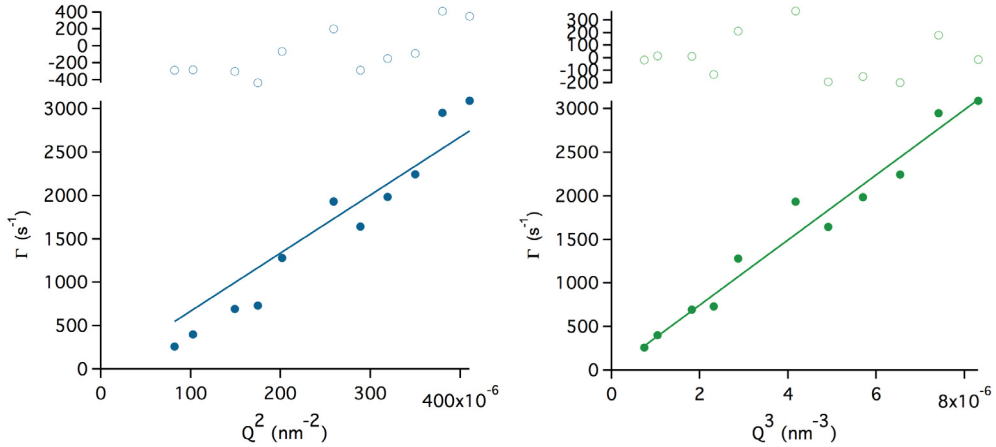

Figure 4.7.: Relaxation rate Γ of DLS measurements of a feeding-microgel prepared with 2 mol% BIS as a function of a) Q^2 and b) Q^3. The residuals show that a linear fit to Q^3 describes the data more accurately.

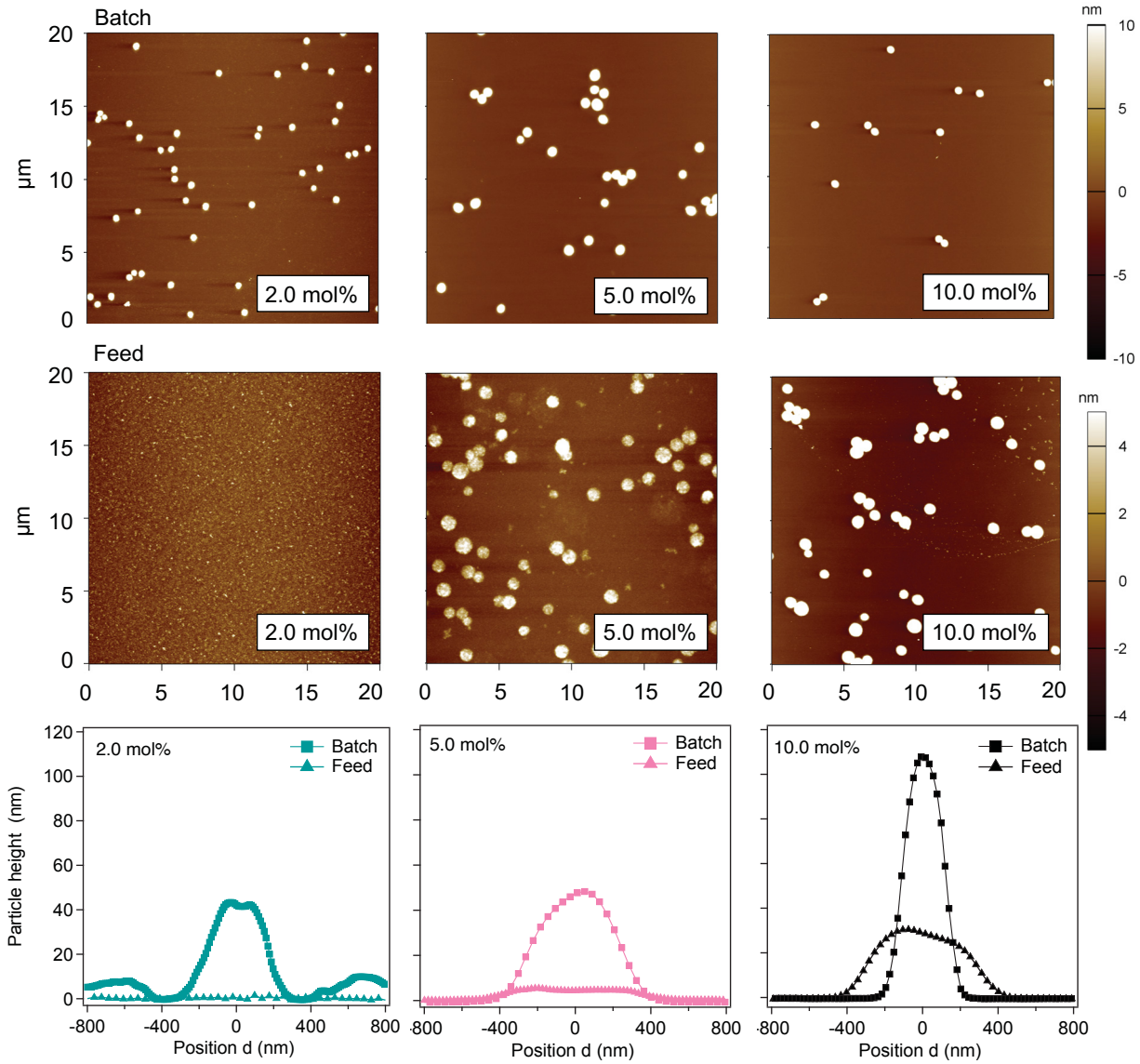

Figure 4.8.: Atomic force microscopy topography images (20x20 μm^2) of batch- and feeding-microgels with different amounts of cross-linker adsorbed on silicon substrates under ambient conditions (air, r.t.). Bottom: Height crosssections averaged over five individual particles.

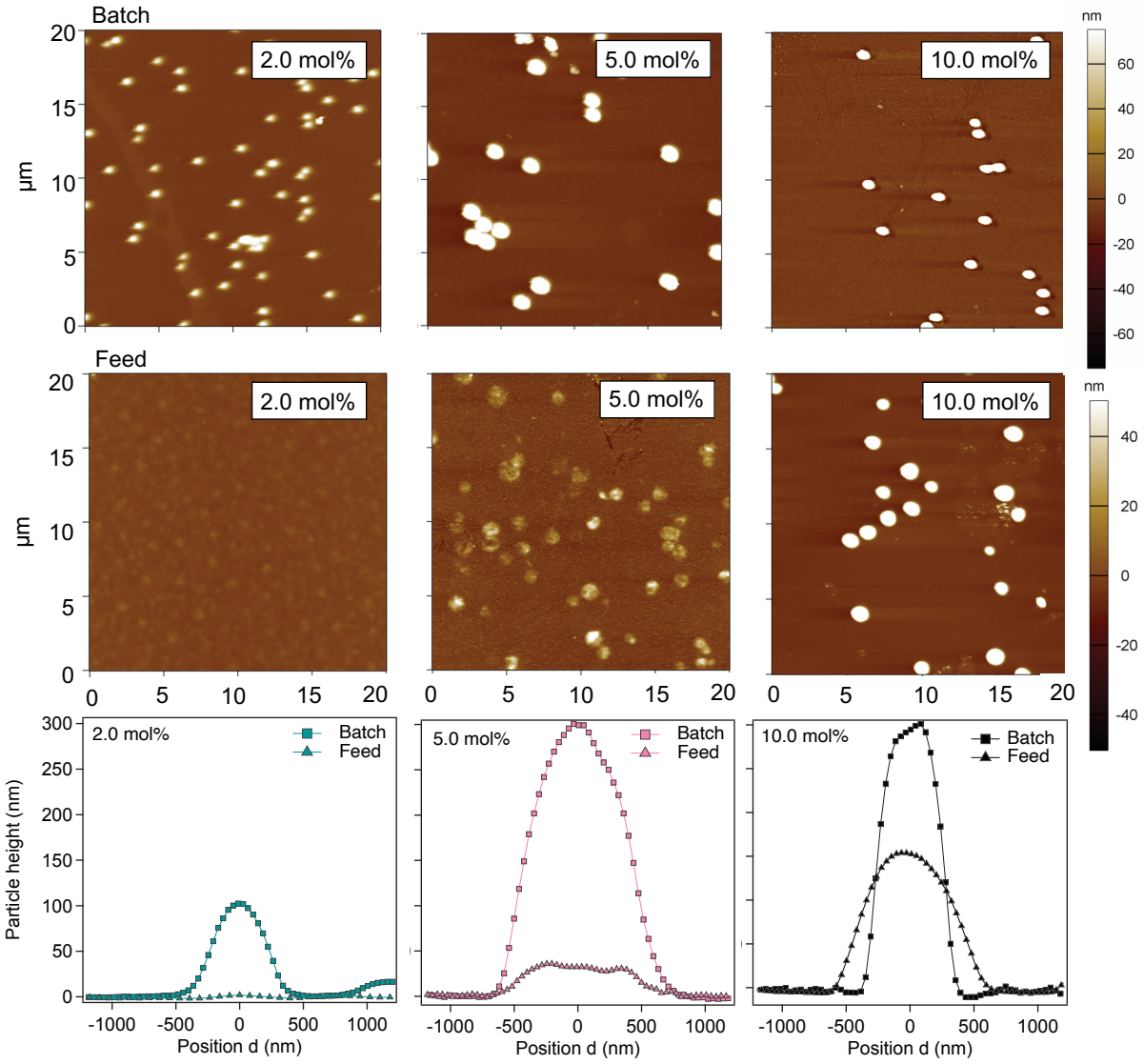

Figure 4.9.: Atomic force microscopy topography images (20x20 μm^2) of batch- and feeding-microgels with different amounts of cross-linker adsorbed on silicon substrates and swollen in water at 20 $°C$. Bottom: Height crosssections averaged over five individual particles.

4.3. Discussion

In summary, we found that microgels prepared by a conventional batch method and the continuous monomer feeding method show distinct differences in their optical properties and their adsorption to solid substrates.

The transmittance of feeding-microgels is significantly increased. This is in agreement with findings by Acciaro *et al.*, who prepared microgels in a similar manner. They argue that the change in transmittance is due to a smaller scattering contrast, which results from the more even distribution of polymer chains in the network.[23] In batch-microgels the dense core provides an optically denser material, which is absent in feeding-microgels.

The characteristic swelling behavior of PNIPAM microgels is preserved in microgels prepared by the continuous monomer feeding method. However, feeding-microgels have slightly higher swelling ratios and VPTTs.

The observation that batch-microgels prepared with a low molar fraction of cross-linker swell more strongly is in agreement with results by Kratz *et al.*[95] While the feeding-microgels with 2 mol% BIS could not be measured, we observe this tendency for feeding-microgels with 5 and 10 mol% BIS as well.

The continuous monomer feeding method yielded no spherical particles with a swollen hydrodynamic radius between 300 and 400 nm when attempted with a rather low cross-linker concentration of 2 mol%. The measured hydrodynamic radii are between 30 and 40 nm and the relaxation rate showed Q^3-dependency. This can lead to one of two conclusions. Either the polymerization was not successful and yielded a polymer network with embedded small particles or the scattering contrast of feeding-microgels prepared with 2 mol% cross-linker is too low to successfully measure spherical objects. This last conclusion is supported by the high transmittance of approximately 1. Furthermore, in the adsorbed state no distinct spherical objects of this sample were observed. A microgel with such a low amount of cross-linker and no dense core likely behaves as a polymer film upon adsorption and the particles just collapse onto the surface.

In general, the findings for the adsorbed PNIPAM microgels are in agreement with other studies. Burmistrova *et al.* for example, studied PNIPAM microgels prepared with a negatively charged comonomer and found that a higher content of cross-linker led to higher particle profiles.[96] Due to the usage of a charged comonomer in the study by Burmistrova *et al.* a direct comparison of the resulting heights is not valid, because of the Donnan potential's contribution to the osmotic pressure in ionic microgels. Finally, high aspect ratios of feeding-microgels indicate that the network collapses onto

the planar solid surface due to the lack of a dense core. The dense core provides stability to batch-microgels. Therefore, we are choosing batch- and feeding-microgels with 10 mol% BIS for further z-resolved studies of adsorbed microgel particles. With their lower aspect ratio, z-resolution will be feasible, which might be problematic in case of the rather flat feeding-microgels with 5 mol% cross-linker. The assumption is made that the near-surface fluctuations of those microgels will be damped more and a low amplitude of fluctuations will lead to a low signal in GINSES experiments.

4.4. Conclusion

In this chapter, the author reports the preparation of PNIPAM-based microgels with molar fractions of 2, 5 and 10 mol% of the cross-linker BIS by the batch and the continuous monomer feeding method. DLS, and AFM images indicate limitations to the usage of PNIPAM-based feeding-microgels prepared with molar fractions of cross-linker concentrations of 2 mol%.

Optical properties of microgel dispersions give first indications of the different network structures resulting from the preparation method. A lower scattering contrast from feeding-microgels is expressed in a high transmittance of visible light. Due to the similar temperature-dependent swelling behavior of both microgels in bulk, feeding-microgels might substitute batch-microgels for certain applications. However, the high aspect ratios of adsorbed feeding-microgel particles challenge the replacement of batch-microgels in surface applications. In conclusion, batch- and feeding-microgel particles with 10 mol% BIS are chosen for further analysis of surface dynamics with elaborate neutron scattering techniques.

5. Internal Structure and Dynamics of Highly Cross-Linked PNIPAM Microgels

Abstract

The internal structure and dynamics of poly(*N*-isopropylacrylamide) microgels with different degrees of cross-linking have been investigated for conventional batch-microgels. However, a detailed understanding of the internal structure and dynamics of recently developed feeding-microgels is still lacking. Furthermore, the question remains, how the proposed more even distribution of cross-links influences the internal structure and dynamics after adsorption on solid surfaces. In this chapter, we compare results from small angle neutron scattering and neutron spin echo spectroscopy of highly cross-linked batch- and feeding-microgels to results from surface-sensitive methods such as atomic force microscopy force mapping and neutron spin echo under grazing incidence. There is a limited number of techniques to investigate surface dynamics of thin microgel coatings. Neutron spin echo spectroscopy under grazing incidence allows to distinguish between dynamics from near-surface layers and the averaged dynamics over the entire adsorbed microgel coating in z-direction. Simulations of the intensity distribution of the evanescent field and the experimental background with BornAgain aid the analysis of grazing incidence scattering data.

Similar content is published in:

- Witte, J.; Kyrey, T.; Lutzki, J.; Dahl, A. M.; Houston, J.; Radulescu, A.; Pipich, V.; Stingaciu, L.; Kühnhammer, M.; Witt, M. U.; von Klitzing, R.; Holderer, O.; Wellert, S. A Comparison of the Network Structure of Homogeneously and Heterogeneously Crosslinked PNIPAM Microgels with High Crosslinker Content. *Soft Matter,* **2019,** *15,* 1053-1064.
- Witte, J.; Kyrey, T.; Lutzki, J.; Dahl, A. M.; Kühnhammer, M.; von Klitzing, R.; Holderer, O.; Wellert, S. Looking Inside Poly(*N*-isopropylacrylamide) Microgels:

Nanomechanics and Dynamics at Solid-Liquid Interfaces. *ACS Applied Polymer Materials,* **2021,** *3,* 976-985.

The author would like to thank M. Kühnhammer for nanoindentation measurements, and for scanning the fast force maps presented in this chapter.

5.1. Introduction

Responsive microgels are discussed for diverse applications in biomedicine,[97] wastewater treatment,[98] heterogeneous catalysis,[99] cell culturing[100] and sensors.[101] While many applications demand microgel particles in the bulk state, a number of applications demands for conformal microgel coatings to modify surface properties like wettability, friction coefficient or the elastic modulus of a surface. An extensive review of envisioned applications for microgels is given in Ref. 102.

In this chapter, highly cross-linked (10 mol% BIS) PNIPAM microgels were prepared with surfactant-free precipitation polymerization. First, microgels were prepared with a conventional batch method, and later with a continuous monomer feeding method (details can be found in Chapter 3.1.1). The main purpose of this chapter is the comparison of the internal structure and dynamics of both types of microgels. Furthermore, the chapter investigates how the different structural and dynamical properties translate to conformal microgel coatings on planar solid substrates.

This work will further the understanding of the surface properties of more homogeneously cross-linked PNIPAM microgel particles. It will also help to understand how the internal dynamics in near-surface layers of core-shell type microgels with a heterogeneous cross-link distribution are influenced differently from the internal dynamics of homogeneously cross-linked microgels. Finally, it will contribute to the understanding of whether perceived advantages of a homogenous cross-link distribution are transferable to surface applications.

In the past, the internal structure of PNIPAM microgels prepared with the batch method has been investigated in neutron scattering studies. Karg *et al.* and Kratz *et al.* studied the influence of the degree of cross-linking on the internal structure by addition of different molar fractions of BIS to the polymerization.[92,95] They investigated how the degree of cross-linking affects the correlation length and found that a higher degree of cross-linking led to a decreasing correlation length of the network. Reufer *et al.* investigated how the temperature influences the structure of PNIPAM microgels and drew conclusions on the models suitable for the analysis of scattering data.[103] Stieger

et al. developed the fuzzy sphere model taking into consideration the heterogeneous distribution of cross-links in the microgels prepared by a batch method.[18] Prior to that, Fernández-Barbero *et al.* had developed a core-shell model with specific correlation lengths for the shell (ξ_{shell}) and the core (ξ_{core}).[20] However, the fuzzy sphere model (for details see Chapter 3.2.5) has been used more frequently in recent literature and has even been applied by Fernández-Barbero in 2013.[21]

Another method for the investigation of the network morphology is super-resolution optical microscopy. Bergmann *et al.* used direct Stochastic Optical Reconstruction Microscopy (dSTORM) to investigate the localization density of freely diffusing fluorophores within PNIPAM microgel particles. They were able to describe the network morphology by a modified fuzzy sphere model.[104] Conley *et al.* labelled the co-monomer used during precipitation polymerization with a fluorescent dye to observe the polymer density profile during the volume phase transition of PNIPAM microgels.[105]

Acciaro *et al.* prepared monodisperse PNIPAM microgels with a homogeneous cross-link distribution using a feeding method. In their study, they focused on the polymerization kinetics, swelling properties and optical properties of the resulting microgel particles as evidence for a more homogeneous distribution of cross-links in the microgel particles.[23] Witt *et al.* adopted and modified this feeding method to compare the loading capacity of heterogeneously and homogeneously cross-linked PNIPAM-*co*-AAc microgels with magnetic nanoparticles (MNPs). Indeed, they found a more even distribution of MNPs in the network of the feeding-microgel with a higher overall loading using cryo-TEM. In case of batch-microgels they found that the MNPs could not diffuse into the more cross-linked particle core.[53] In another study, Mueller *et al.* accomplished a more homogeneous network structure *via* an aqueous self-assembly process based on hydrazide and aldehyde- functionalized PNIPAM oligomers. They were able to show this internal structure with a combination of surface force measurements, SANS and USANS.[106]

Furthermore, studies have investigated the internal dynamics of PNIPAM-based microgels with NSE in transmission mode. Hellweg *et al.* investigated PNIPAM microgels with 1, 2 and 5 mol% BIS. They observed a decreasing diffusion coefficient of the collective network motion with increasing cross-linker concentration.[93] Another set of studies investigated the cononsolveny effect on the dynamics of PNIPAM and PDEAAM-based microgels. They found that particles that collapsed due to the cononsolvency effect showed little to no internal dynamics, while those that remained swollen had a cross-over from collective diffusive motion at low Q-values to Zimm segmental dynamics above a

certain Q-value.[107,108] Maccarone *et al.* further investigated the structure and dynamics of different core-shell systems, namely Collapsed Core Swollen Shell (CCSS) and Swollen Core Collapsed Shell (SCCS) microgels. With NSE they found different dynamic signatures for both systems. While CCSS microgels displayed the cross-over region from collective diffusive motion to Zimm segment dynamics, the SCCS only showed collective diffusive motion over the observed Q-range. This was explained by the collapsed and aggregated parts of the shell that influenced the dynamics of the entire microgel particle.[109]

Incoherent elastic and quasielastic neutron scattering (IENS, IQNS) were used by Sierra Martin *et al.* to investigate the molecular motions in polymer segments of microgel particles.[21]

Kyrey *et al.* investigated the structure and dynamics of the microgels with 2 and 5 mol% BIS, discussed in Chapter 4 of this thesis, with SANS and NSE in transmission mode. They fitted SANS data with a model that takes into account static inhomogeneities usually used for macroscopic gels. For microgels this contribution is usually not resolved because of the influence of the form factor on the scattering data. Furthermore, they found a fit with a spheres- in spheres model best described the data of the collapsed microgel particles above the VPTT. From this, they could determine the number of smaller domains present in the microgel particles. While they found that Zimm segmental dynamics contributed to the dynamics of feeding-microgels at all degrees of cross-linking, no Zimm segmental dynamics were observed in the used Q-range for batch-microgels.[110]

Gawlitza *et al.* applied neutron spin echo spectroscopy in reflection mode to polyethylene glycol-based microgel particles with different amounts of the comonomer OEGMA to observe the near-surface dynamics. They observed a slowing down of the dynamics in near-surface layers as compared to the layers reaching toward the bulk. With their study, they were able to show the feasibility of such measurements.[87]

In this chapter, the author aims to thoroughly investigate the internal structure and dynamics of batch- and feeding-microgels in bulk and compare those results to microgel coatings. This will help to understand how adsorption to solid substrates influences microgel particles with different internal structures differently. Furthermore, the author shows the advancement of the method due to instrumental improvements and the application of simulations of the evanescent field intensity map.

5.2. Results

The first part of this chapter is concerned with the investigation of bulk properties of highly cross-linked PNIPAM-based microgels (10 mol% BIS). All experiments were conducted with a semidilute PNIPAM solution as a reference. SANS data is analyzed to learn more about the internal structure, like the correlation length (related to the mesh size) and the fuzziness parameter. In the second part, NSE data is analyzed to draw conclusions about the internal dynamics of the microgels' polymer network. Analysis over a wide Q-range allows the observation of different length scales and the thermal density fluctuations occurring on those length scales. Finally, microgel particles are spin coated onto solid planar substrates to investigate their nanomechanics and dynamics in the adsorbed state. AFM force mapping is used to determine and compare the elastic modulus E of the adsorbed microgel particles. Moreover, grazing incidence neutron spin echo spectroscopy (GINSES) is a useful tool to distinguish dynamics of near-surface layers, and the averaged dynamics over the entire vertical monolayer profile. BornAgain simulations are used to simulate the intensity map of the evanescent field. This facilitates the understanding of background contributions to the signal and the estimation of the penetration depth of the evanescent field. The nomenclature of the samples in this chapter will be MG_xP and MG_xF, where x is the molar fraction of cross-linker and P and F stand for batch- and feeding-microgel, respectively.

5.2.1. Bulk Properties

Internal Structure from Small Angle Neutron Scattering

Semidilute PNIPAM solution The correlation length in a semidilute solution of linear PNIPAM chains (M_W=30 kDa) was determined from SANS measurements in a Q-range between $2{\cdot}10^{-3}$ and 0.4 $Å^{-1}$ (s. Figure 5.1).

The data is described well by the correlation length model (Eq. 5.1).[111]

$$I(Q) = \frac{A}{Q^n} + \frac{C}{1 + (Q\xi)^m} + I_{inc} \tag{5.1}$$

The fit results in a correlation length ξ=2.8 nm and a low-Q exponent of n=2 from structural inhomogeneities in the solution on larger length scales. The high-Q exponent m was chosen as 1.7, which is a typical value for a polymer in a good solvent.[2]

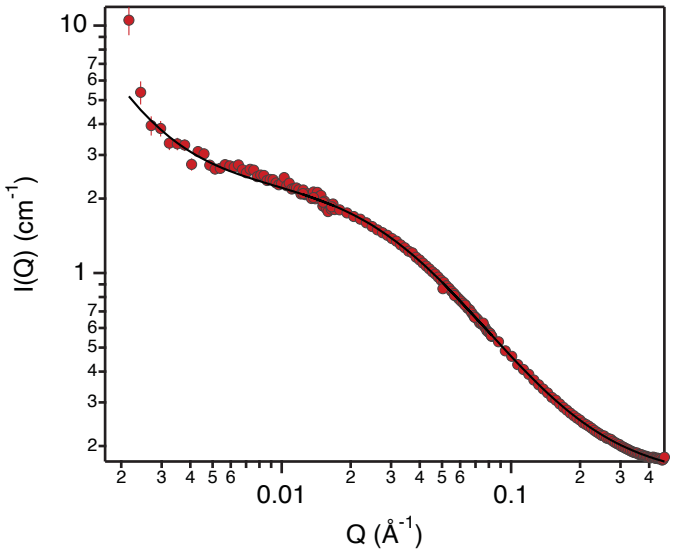

Figure 5.1.: SANS data of a semidilute solution of linear PNIPAM chains (M_W=30 kDa) at 20 °C in D_2O recorded on KWS-2. Experimental data were approximated with the correlation length model.[111]

PNIPAM microgels SANS data of highly dilute microgel dispersions (0.001 wt%) are displayed in Figures 5.2 and 5.3. Low-Q data (Fig. 5.2, $3{\cdot}10^{-4}$ Å$^{-1} \leq Q \leq 2 \cdot 10^{-3}$ Å^{-1}) describes the form factor of individual microgel particles. Both data sets could be approximated with a fuzzy sphere model according to Stieger *et al.*[18] The batch-microgel $MG_{10}P$ can be approximated with a fuzzy sphere with a radius R = 180 nm and a fuzziness parameter of σ_{surf} = 30 nm. According to equation 3.17, this yields an overall radius R_{SANS} = 240 nm. The radius R of the feeding-microgel $MG_{10}F$ was approximated to be 289 nm with a fuzziness parameter of σ_{surf} = 4.2 nm. Relating R_{SANS} to the fuzziness parameter suggests that the fuzziness only contributes 1.5 % to the overall radius in case of $MG_{10}F$, but 12.5 % to the overall radius of $MG_{10}P$. This indicates that the feeding-microgel indeed has a more homogeneous internal structure. Assuming a segment length of 8.12 Å for NIPAM[112] a fuzziness of 4.2 nm (42 Å) corresponds to approximately 5 segments. On the other hand, a fuzziness of 30 nm (300 Å) corresponds to 37 segments.

Intermediate- and high-Q data (Fig. 5.3) describe two distinct regions. In the intermediate region, often called the Porod region, the scattering signal can be described by a power law A/Q^{-n}. Typically, the Porod exponent is n = 4. However, our data deviate from the ideal Porod exponent. High-Q data was approximated with the Ornstein-

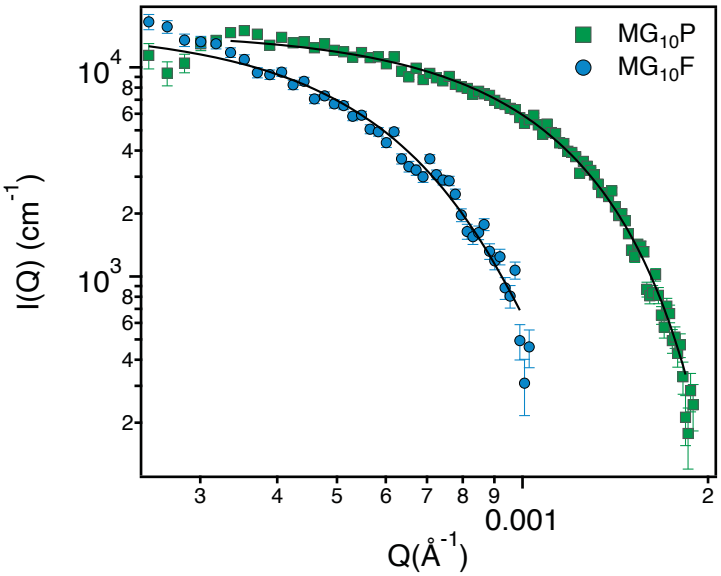

Figure 5.2.: Low-Q SANS data of PNIPAM microgels $MG_{10}P$ and $MG_{10}F$ at 20 °C in D_2O recorded on KWS-3. Experimental data were approximated with a fuzzy sphere model.

Zernike model. The intensity $I_L(0)$ describes the Ornstein-Zernike contribution and therefore the contribution of thermal density fluctuations to the scattering signal. We find a lower value of $I_L(0) = 0.09$ cm^{-1} for the batch-microgel, compared to $I_L(0) = 0.33$ cm^{-1} for the feeding-microgel. Furthermore, the correlation length, which in homogeneous networks is related to the mesh size, is higher in the feeding-microgel ($\xi = 3.2\ nm$) compared to the batch-microgel ($\xi = 2.0\ nm$). Karg *et al.* found for PNIPAM microgels, prepared by the batch method with different molar fractions of cross-linker that $I_L(0)$ and ξ decreased with increasing connectivity (*i.e.* increasing cross-link concentration). Therefore, our results can be interpreted as follows. The batch-microgel, as expected, has a dense core, with a smaller correlation length of dynamic fluctuations that contribute little to the scattering signal. This is futher supported by the higher fuzziness parameter of $MG_{10}P$. The feeding-microgel, on the other hand, does not have a dense core, but a network with more evenly distributed cross-links. As the cross-links are more evenly distributed over a wider radius the correlation length increases along with the contribution of the dynamic fluctuations to the scattering signal.

As the microgel particles collapse at elevated temperatures, the fuzziness and dynamic network fluctuations do not contribute to the scattering signal anymore. SANS data at 50 °C were therefore fitted with the empirical Guinier-Porod model[113]

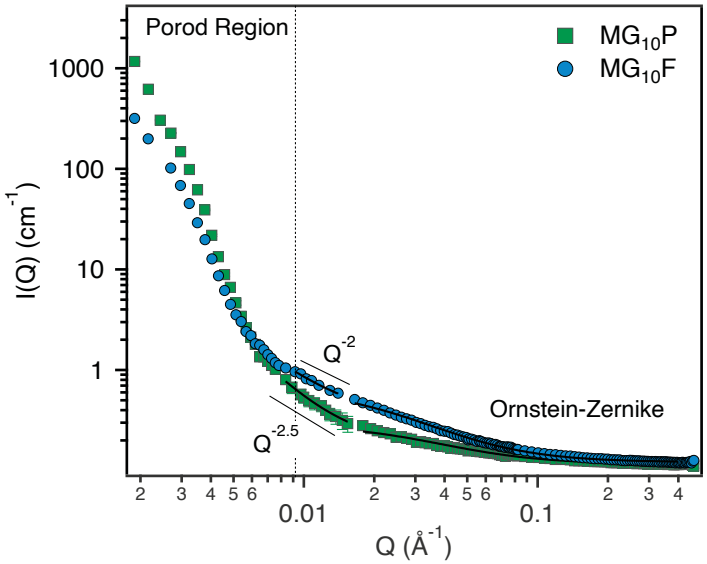

Figure 5.3.: Intermediate- and high-Q SANS data of PNIPAM microgels $MG_{10}P$ and $MG_{10}F$ at 20 °C in D_2O recorded on KWS-2. The high-Q region was approximated with an Ornstein-Zernike model to extract the correlation length ξ of thermal density fluctuations. The Porod region deviates from the classical Q^{-4} behavior.

$$I(Q) = Gexp\left(\frac{-Q^2R_g^2}{3}\right) \qquad for\ Q \leq Q_1 \tag{5.2}$$

$$I(Q) = \frac{D}{Q^m} \qquad for\ Q \geq Q_1 \tag{5.3}$$

with G the scaling factor for the Guinier term, R_g the radius of gyration, D the scaling factor for the Porod term and m the Porod-exponent. Q_1 is calculated internally according to

$$Q_1 = \frac{1}{R_g}\left(\frac{3m}{2}\right)^{1/2}. \tag{5.4}$$

The fit of the scattering curve of the collapsed feeding-microgel was extended by a term A/Q^{3+x} as suggested by Wong for porous solids.[114] The parameter x takes into account the roughness of the scattering interface and typically assumes values around x=1.3 for microgels. The Porod-exponent is 4 for both microgel systems. We find a value of x=1.4, which is close to the typical value for microgels of x=1.3.[92,95] However, for the batch-microgel the extension according to Wong did not lead to an improvement

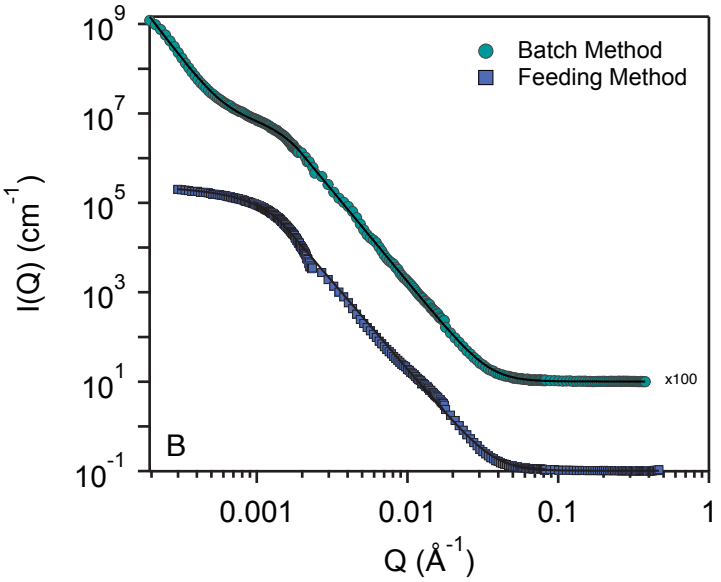

Figure 5.4.: SANS data for PNIPAM microgels $MG_{10}P$ and $MG_{10}F$ at 50 °C in D_2O. The intensities of the batch-microgel were multiplied by a factor 100 to better visualise the data.

of the fit. Although Karg *et al.* found $x = 1.16$ for a PNIPAM batch-microgel with 15 mol% BIS, we assume that in our case there is no substantial contribution of the surface roughness to the scattering signal.

A comparison of the obtained SANS radii R_{SANS} with the hydrodynamic radii R_h from DLS experiments shows significant differences. However, this is because SANS measures a radius closer to the radius of gyration R_g rather than the hydrodynamic radius R_h. As explained in Chapter 3.2.1, the hydrodynamic radius is the radius of a sphere that would experience a friction *f*, identical to the friction experienced by the scattering particle. Therefore, a porous object, such as a microgel, will experience a higher friction than a solid sphere and the radius determined by DLS will always be overestimated.[115] Other authors explain the difference with dangling ends on the particle surface with a concentration too low to be detected by SANS measurements.[18,116]

The parameter ρ can be calculated according to $\rho = R_g/R_h$ and is a measure for the softness of scatterers. The typical hard sphere value is 0.78.[117] Values below 0.78 where found for soft spheres. Assuming that $R_{SANS} \approx R_g$, in the case of our microgels we find ρ=0.59 and 0.62 at 20 °C for the feeding- and batch-microgel, respectively. Therefore, in bulk swollen microgels can be categorized as soft spheres. The ratio ρ between R_g and R_h for collapsed particles are 0.63 and 0.74 for feeding- and batch-microgels, respectively.

Table 5.1.: Microgel dimensions as determined by DLS and SANS.

Sample	T [°C]	R_{SANS} [nm]	R_h [nm]	ρ	R_{box} [nm]	σ_{surf} [nm]	ξ [nm]
$MG_{10}F$	20	298	463 ± 7	0.62	289 ± 2	4 ± 1	3.2±0.1
$MG_{10}P$	20	240	310 ± 2	0.58	180 ± 1	30 ± 1	2.0±0.1
$MG_{10}F$	50	135	214 ± 2	0.63	–	–	–
$MG_{10}P$	50	124	186 ± 1	0.67	–	–	–

Table 5.2.: Dynamic properties of batch- and feeding-microgels.

Sample	D_{coop}[10^{-11} m^2 s^{-1}]	ξ_{coop} [nm]	D_{Zimm}[10^{-11} m^2 s^{-1}]	η_{sp}
$MG_{10}F$	5.0 ± 0.1	3.4	43 ± 2	2.0
$MG_{10}P$	2.7 ± 0.1	6.4	-	-
PNIPAM solution	-	-	49 ± 2	1.2

Therefore, while no significant change is observed for the feeding-microgel, the batch-microgel particle approaches the value for hard spheres in the collapsed state. A detailed list of the resulting parameters can be found in Table 5.1.

Internal Dynamics of Highly Cross-Linked PNIPAM Microgels

Normalized intermediate scattering functions (ISF) from NSE experiments were fitted with a single exponential according to

$$\frac{S(Q,\tau_{NSE})}{S(Q,0} = (1-A) + A \cdot exp(-\Gamma\tau_{NSE})^{\beta}. \tag{5.5}$$

The two fitting parameters are the amplitude A and the relaxation rate Γ. The exponent β equals 1 for collective network diffusion and 0.85 in case of Zimm-dynamics.[80] The resulting relaxation rates were used to calculate the cooperative diffusion coefficient D_{coop} according to

$$D_{coop} = \frac{\Gamma_{coop}}{Q^2}. \tag{5.6}$$

D_{coop} describes the breathing motion of the polymer network, resulting from collective fluctuations from thermal excitation. D_{coop} is displayed against the entire Q-range in Figure 5.6.

$D_{coop} = \Gamma_{coop}/Q^2$ is plotted against the momentum transfer Q in Figure 5.6. The behavior of Γ_{coop}/Q^2 indicates whether purely cooperative network motions are observed

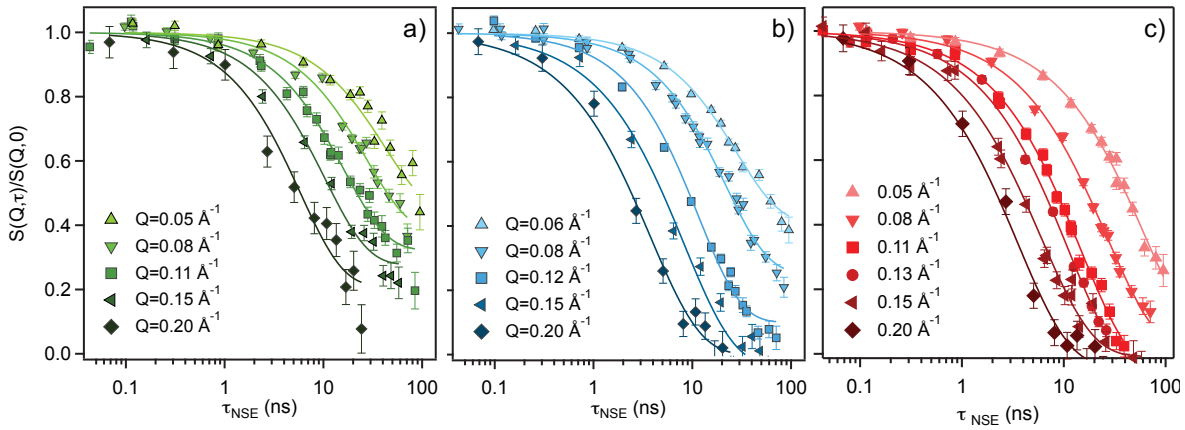

Figure 5.5.: Normalized ISFs for a highly cross-linked a) batch- and b) feeding-microgel. c) Normalized ISFs for a 30 kDa semidilute aqueous PNIPAM solution.

(constant value of D_{coop}). The results for a semidilute PNIPAM solution are plotted for comparison, because here a deviation from a constant value is expected (Zimm-type segmental polymer dynamics). Indeed we observe that Γ_{coop}/Q^2 increases with Q. D_{coop} of the feeding-microgel shows a constant value between $0.05 \leq Q \leq 0.12$ Å^{-1} (s. Figure 5.6). Therefore, cooperative network fluctuations with $D_{coop} = 5 \cdot 10^{-11}$ m^2 s^{-1} are observed in this Q-range.

The batch-microgel has a constant diffusion coefficient of $D_{coop} = 2.69 \cdot 10^{-11}$ m^2 s^{-1} over the entire Q-range. This suggests that the network fluctuations in the feeding-microgels are faster than those in the batch-microgel. Furthermore, they de-correlate over smaller distances as indicated by the dynamic correlation length ξ_{coop}. The diffusion coefficient of the feeding-microgel increases above $Q = 0.12$ Å^{-1} . This suggests that segmental Zimm-type polymer dynamics are observable at higher Q-values (*i.e.* smaller length scales), comparable to a semidilute solution. Therefore, ISFs of the feeding-microgel with $Q \leq 0.12$ Å^{-1} were fitted with $\beta = 0.85$ and the Zimm-type diffusion coefficient was determined. The diffusion coefficient of the Zimm-type dynamics is defined as

$$D_{Zimm} = \frac{\Gamma}{Q^3}. \tag{5.7}$$

A linear fit with a slope of zero to Γ/Q^3 yields D_{Zimm}.
D_{Zimm} can be used to calculate the specific viscosity η_{sp}. This dimensionless number measures the contribution of the polymer to the solution viscosity. First, the apparent viscosity η_{app} is calculated according to

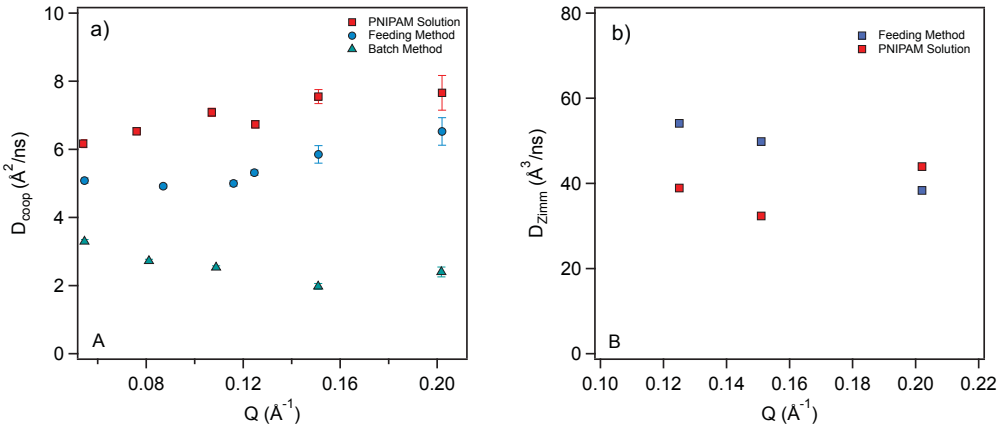

Figure 5.6.: a) Cooperative diffusion coefficient D_{coop} for microgels prepared with the batch and feeding method over a wide Q-range. For comparison D_{coop} of a semidilute PNIPAM solution is displayed. b) Diffusion coefficients of the Zimm-type dynamics D_{Zimm} for the microgel prepared by the feeding method and a semidilute PNIPAM solution.

$$\eta_{app} = \frac{k_B T}{6\pi D_{Zimm}} \frac{1}{1.354}, \tag{5.8}$$

where k_B is the Boltzmann constant, T the temperature in K, and D_{Zimm} the diffusion coefficient of the Zimm-type dynamics. The specific viscosity η_{sp} is then calculated according to

$$\eta_{sp} = \frac{\eta_{app} - \eta_s}{\eta_s}, \tag{5.9}$$

where η_s is the solvent viscosity. Results are displayed in Table 5.2. The feeding-microgel has a specific viscosity of 2. For comparison the value for a semidilute PNIPAM solution is 1.2. Therefore, the polymer has a non-negligible influence on the solution viscosity.

Another feature of the fit to the ISFs is expressed by the term (1-A), which expresses the contribution of elastic scattering to the signal. The batch-microgel shows relatively high elastic contributions. These contributions are present only up to $Q = 0.11$ Å^{-1} for the feeding microgel and the ISFs decay to zero above that Q-value. This is in agreement with the Q-range in which cooperative network motion is observed. This could suggest an elastic contribution to the signal, which is often explained with inhomogeneities in the

Table 5.3.: Elastic contributions (1-A) to the ISFs. Q-values that deviate for feeding-microgels in parentheses.

Q (Å^{-1})	**(1-A) Batch**	**Δ (1-A) Batch**	**(1-A) Feeding**	**Δ (1-A) Feeding**
0.05(0.06)	0.45907	0.0519	0.41097	0.0212
0.08	0.37785	0.0301	0.253	0.0146
0.11(0.12)	0.32318	0.0169	0.10061	0.0111
0.15	0.27728	0.0187	0	–
0.20	0.20948	0.0439	0	–

microgel network.[107] Those inhomogeneities' dynamics are slower than polymer segment dynamics and cannot be resolved within the time range of an NSE experiment.

5.2.2. Nanomechanics and Internal Dynamics of Adsorbed Microgel Particles

In the second part of this chapter, the above studied PNIPAM-based microgels with 10 mol% cross-linker were studied at the solid-liquid interface between silicon substrate and (deuterated) water.

Since silicon surfaces are negatively charged, we chose a positively charged thermal initiator (AAPH) for the polymerization to circumvent the use of an additional polyelectrolyte layer. Often, polyethylenimine (PEI) is applied to electrostatically stabilize adsorbed PNIPAM microgels synthesized with negatively charged initiators, such as potassium persulfate (KPS).[118,119] However, an additional polymer layer would change the composition of near-surface layers and therefore is not desirable for the following study of adsorbed microgels. Furthermore, no charged comonomer was used, since the contribution of the Donnan potential to the osmostic pressure would add another level of complexity to the observations.

Nanomechanical Properties by AFM Force Mapping

In the first step, nanomechanical properties of individual swollen microgel particles were probed with AFM nanoindentation. Elastic moduli E at 20 °C and 50 °C were measured in the center of 10 individual particles. The resulting force-distance curves of those measurements are displayed in Figure 5.7. The average E-modulus from 10 force-distance curves from different particles was calculated and the values are displayed in Table 5.4. The elastic moduli were calculated according to the Hertz-model for spherical indenters.

The fit was limited to 20% of maximum indentation to prevent substrate effects from influencing the results.[120]
Measurements in the center of swollen particles showed that the elastic modulus of the batch-microgels is twice as high as that of the feeding-microgels (312±38 kPa versus 166±24 kPa) in the swollen state. This means that the center of batch-microgels is stiffer, which is in agreement with the existence of a highly cross-linked core.
In the collapsed state, *i.e.* at 50 °C, the elastic modulus of both microgels increases to 1004±47 kPa and 1070±106 kPa for batch- and feeding microgels, respectively. Therefore, the elastic moduli of collapsed batch- and feeding-microgels are identical within the error of the experiment.

The core region can be illustrated with bimodal dual AC tapping mode on the AFM (Figure 5.7c + d). This method qualitatively shows contrast resulting from differences in the materials' stiffness and viscoelasticity. The batch-microgel shows a distinct core region in the center of the microgel (dark grey region), surrounded by a corona of differing stiffness (light grey region). The feeding-microgel displays no contrast within itself, indicating a homogeneous viscoelastic nature. However, the bimodal dual AC measurement of the feeding-microgels is influenced by substrate effects, resulting in a lack of contrast between the substrate and microgel particle.

A quantitative analysis of the lateral stiffness of the microgel particles can be achieved with fast force mapping on the AFM. Force maps of batch- and feeding-microgels with a high content of cross-linker reveal differences in the particles' nanomechanical properties in the adsorbed state (s. Figure 5.8). While the batch-microgel $MG_{10}P$ shows a gradient of its elastic modulus with a maximum of 626 kPa in the particle's center and a minimum elastic modulus of 131 kPa towards the particle edge, the feeding microgel $MG_{10}F$ has a mean elastic modulus of 79 kPa with a standard deviation of 16 kPa over the entire particle (s. Figure 5.9). It therefore is constant within the precision of the measurements. Therefore, the mechanical properties of the adsorbed microgels differ in the regions accessible by AFM fast force mapping. The maximum elastic modulus of the batch-microgel is almost 8-times as high as the average elastic modulus of the feeding-microgel. It is concluded that the batch-microgels can be regarded as “hard" microgel particels and the feeding-microgels as“soft" microgel particles. However, the usage of the terms “soft" and “hard" should be understood as relative to each other.

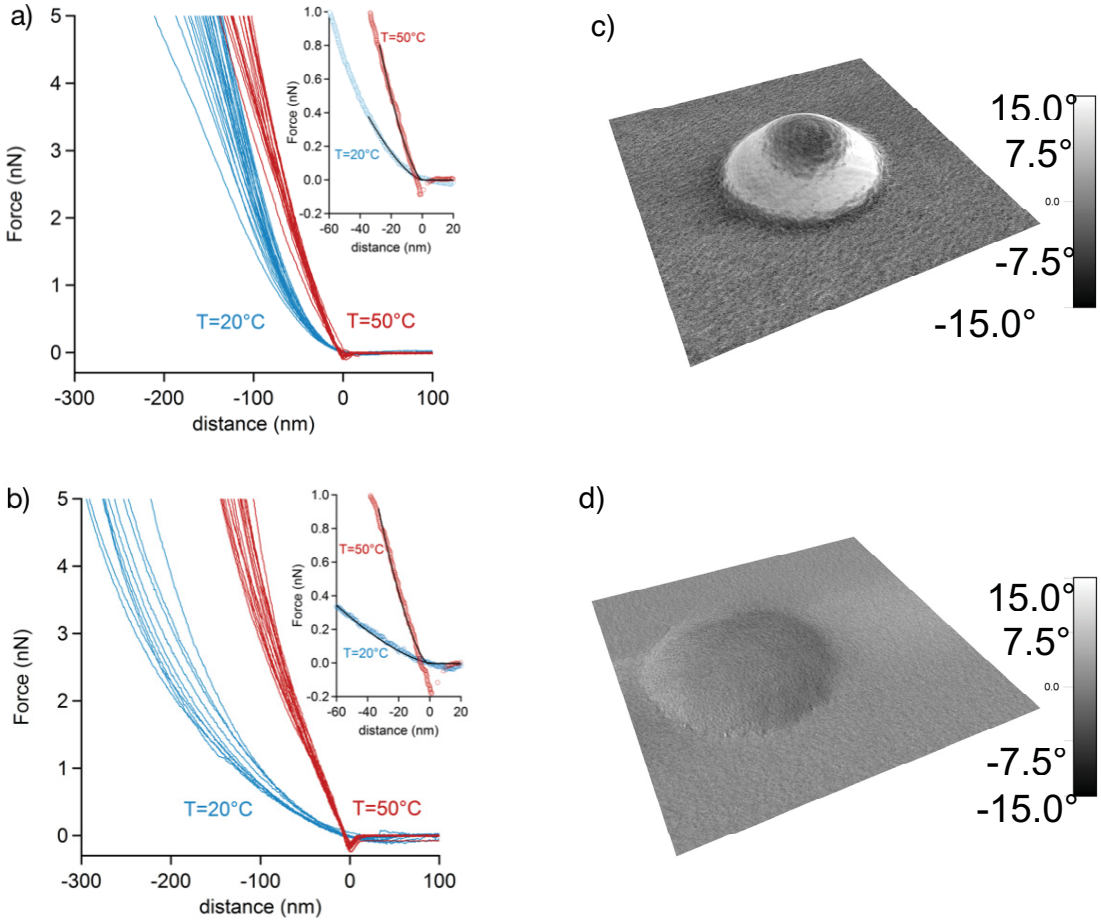

Figure 5.7.: Force-distance curves of a) $MG_{10}P$ and b) $MG_{10}F$ at 20 °C and 50 °C. Fits to the Hertz-model are shown in the insets. c) and d) are bimodal dual AC scans of c) $MG_{10}P$ and d) $MG_{10}F$ in the dry state. The core region of the batch-microgel can be clearly distinguished from the corona.

Table 5.4.: Elastic moduli of swollen (20 °C) and collapsed (50 °C) adsorbed batch- and feeding-microgels.

Sample	$E_{20°C}$ **[kPa]**	$E_{50°C}$ **[kPa]**
$MG_{10}P$	312 ± 38	1004 ± 47
$MG_{10}F$	166 ± 24	1070 ± 106

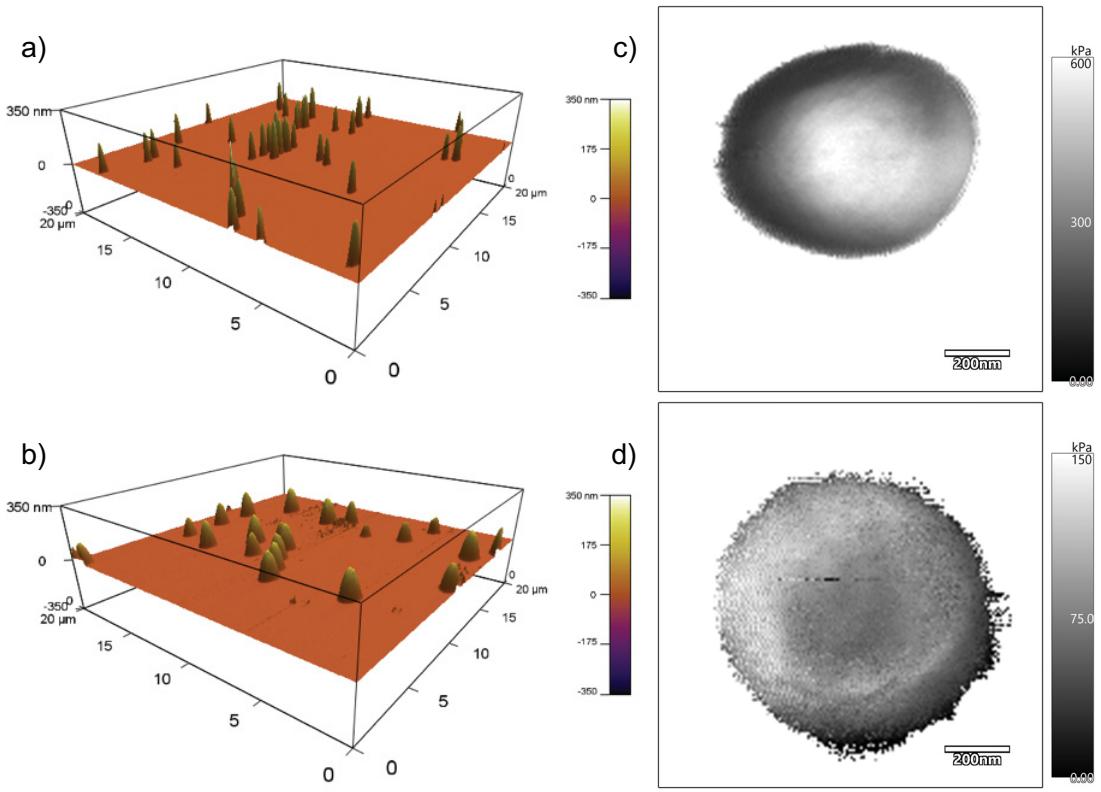

Figure 5.8.: a)+b) 3D topography images of $MG_{10}P$ and $MG_{10}F$ swollen in water at 20 °C. c)+d) Fast force maps of individual batch- (c) and feeding-(d) particles.

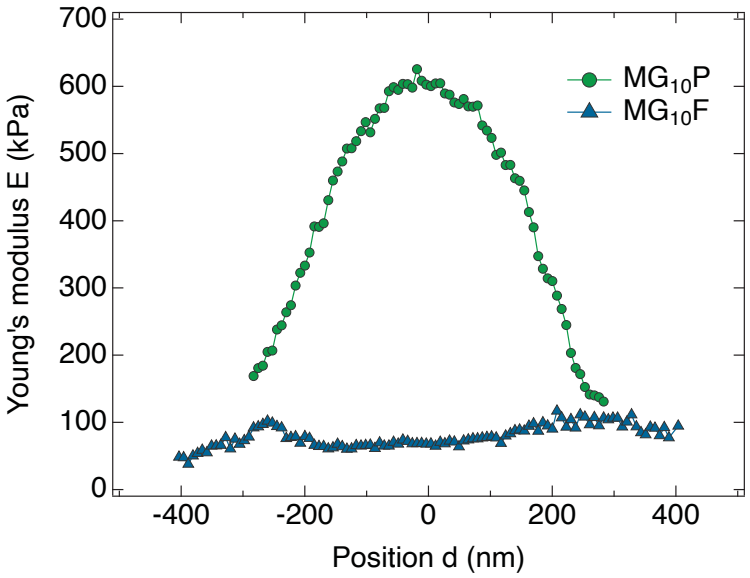

Figure 5.9.: Cross-sections from individual batch- and feeding-microgels displaying the distribution of elastic modulus over the entire particle in lateral direction.

GINSES Experiments

Monolayers of Adsorbed PNIPAM Microgels

Microgel coatings for neutron scattering experiments were prepared by spin coating onto large silicon substrates. We aimed at monolayers with a high surface coverage, but no lateral contact between particles in the dry state. Figure 5.10 shows monolayers of $MG_{10}P$ and $MG_{10}F$, respectively. For $MG_{10}P$ the surface coverage was 57% and 62% for $MG_{10}F$. Therefore, both samples meet the criteria.

Calculation of the Penetration Depth

The penetration depth of the evanescent field was determined according to two different methods.

First, the critical angle of total external reflection α_c was determined from the position of the critical edge of total reflection in neutron reflectograms. According to $\alpha_c = \Pi\sqrt{\Delta\rho}$ the critical angle was recalculated for the conditions of the GINSES experiment. The evolution of the penetration depth was then calculated according to equation 3.40.

Furthermore, the polymer volume fraction profile from neutron reflectivity data was used to simulate the intensity of the evanescent field map. Figure 5.11b exemplifies such a simulated map. The x-axis displays angles of incidence below α_c and the y-axis is the

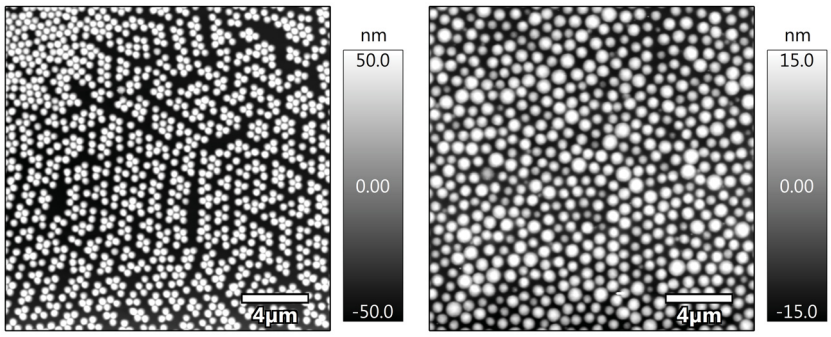

Figure 5.10.: AFM topography images (20 x 20 μm^2) of the batch microgel $MG_{10}B$ (left) and the feeding microgel $MG_{10}F$ (right) under ambient conditions. Monolayers were spin coated from aqueous dispersions (c_{MG}=0.25 wt%) at 1000 rpm for 100 s.

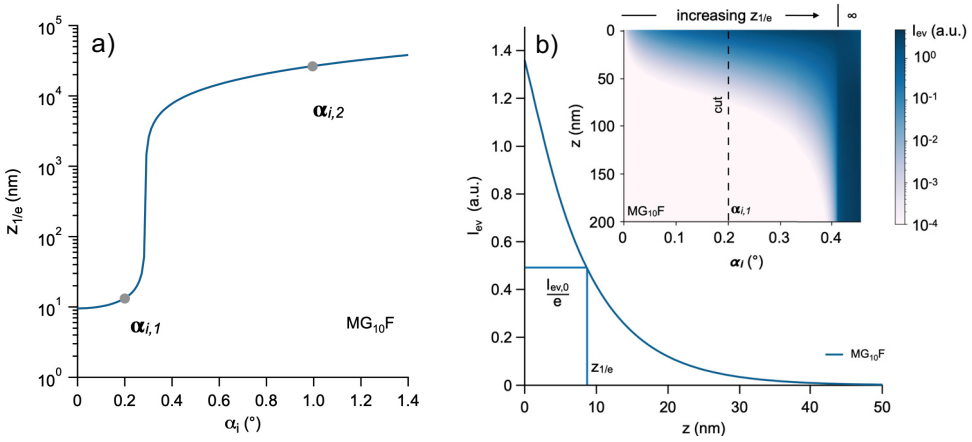

Figure 5.11.: a) The penetration depth of the evanescent field $z_{1/e}$ depends on the angle of incidence α_i and can be calculated according to equation 3.40. Exemplified for $MG_{10}F$. b) The inset shows the intensity map of the evanescent field as simulated with BornAgain. The graph is a line cut at $\alpha_{i,1}$.

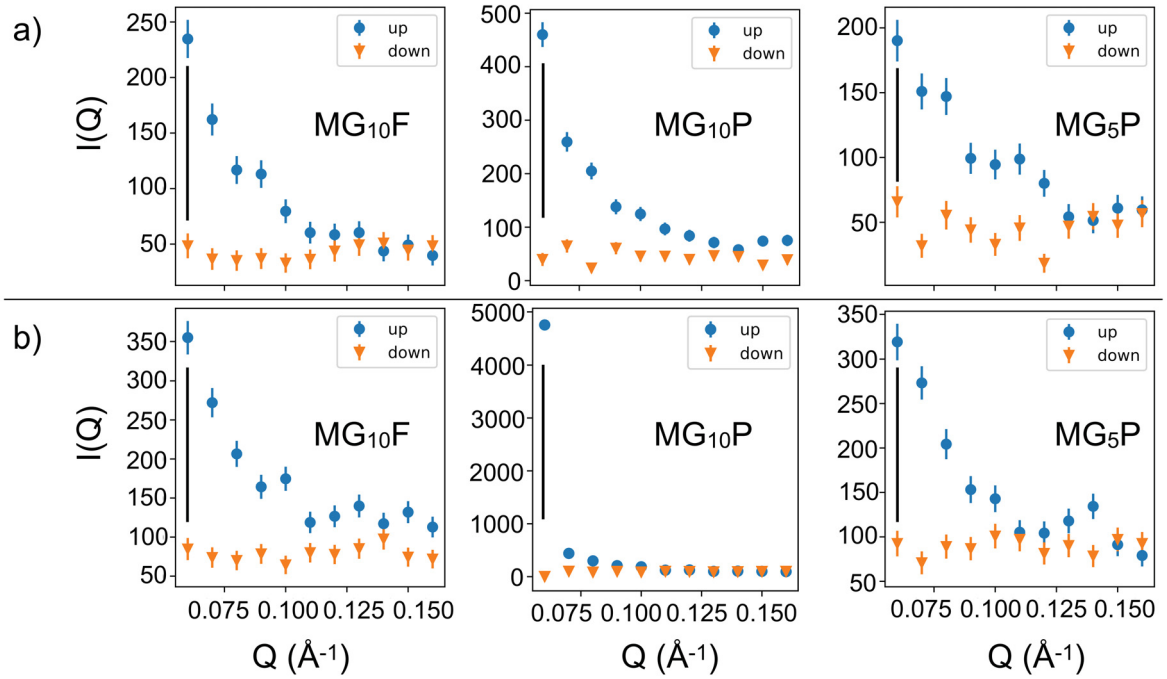

Figure 5.12.: Elastic diffraction scans for the determination of Q_{GINSES} for neutron spin echo experiments under grazing incidence. a) measured at α_i corresponding to $z_{1/e} \approx 10$ nm and b) to $z_{1/e} \to \infty$. (up $\widehat{=}$ coherent, down $\widehat{=}$ incoherent)

position perpendicular to the plane of incidence. Above the critical angle of total external reflection, the intensity has a dark blue value, because the entire volume is probed, and the surface sensitivity vanishes. A line cut at $\alpha_{i,1}$ was made and the evolution of the intensity of the evanescent field with the z-position plotted (s. Figure 5.11b). The penetration depth of the evanescent field is determined as the z-position where the intensity decreases to $I_{ev,0}/e$, with $I_{ev,0}$ the intensity at $z = 0$.
Both methods yield slightly different penetration depths (12 nm and 8.7 nm). However, as mentioned above the calculation lacks precision due to the wavelength distribution. Still, we could determine that at the selected angle of incidence $\alpha_{i,1}$ we are measuring near-surface layers at $z_{1/e} \approx 10\ nm$.

The scattering vector Q_{GINSES} was determined from elastic diffraction scans of the samples at both angles of incidence $\alpha_{i,1}$ and $\alpha_{i,2}$ (Fig. 5.12). A scattering vector of $Q_{GINSES} = 0.06$ Å^{-1} was identified to have a high ratio of coherent (up) and incoherent (down) scattering. This is important, because incoherent background lowers the signal-to-noise ratio.

ISFs between τ_{NSE} = 0.5 and 35 ns of adsorbed $MG_{10}P$ and $MG_{10}F$ are displayed in Figures 5.13 and 5.14. It should be mentioned again that the normalization of the scattering data with a reference sample is not feasible in the reflection geometry. This is because the scattering depends on the difference in SLDs at the interface. In Figures 5.13a and 5.14 a), the angle of incidence was chosen below α_c, which allows the observation of near-surface layers with a neutron penetration depth of approximately 10 nm. Meanwhile in Figures 5.13b and 5.14 b), the angle of incidence was above α_c, therefore probing the entire particle height. Near-surface layers of $MG_{10}P$ and $MG_{10}F$ display distinctly different dynamics. While the cooperative diffusion coefficient D_{coop} of the batch-microgel in the bulk and the adsorbed state is identical within the experimental precision, the dynamics of the feeding-microgel is surpressed in near-surface layers. This is expressed by a low D_{coop} of $0.8{\cdot}10^{-7} cm^2/s$ (Table 5.6). This difference is attributed to the presence of a highly cross-linked core in $MG_{10}P$, which acts as a scaffold to stabilize the network integrity in the adsorbed state. On the other hand, the feeding microgel lacks a dense core, leading to compression and ultimately a slowing down of near-surface dynamics. As the neutron penetration depth increases to virtual infinity, D_{coop} approaches the bulk value for both $MG_{10}P$ and $MG_{10}F$. Values for D_{coop} are summarized in Table 5.6.

The ISFs were fitted according to

$$S(Q, \tau_{NSE}) = (A_0 - A_{bgr}) \times e^{(-\Gamma_{coop}\tau_{NSE})} + A_{bgr}, \tag{5.10}$$

where A_0 is the overall amplitude, A_{bgr} the background, Γ_{coop} the relaxation rate of the cooperative network diffusion and τ_{NSE} the Fourier time in ns.

A_0 is the sum of contributions from density fluctuations in the sample A_s and the background A_{bgr}. We assume that the background amplitude A_{bgr} is the sum of two major contributions, namely the experimental background A_{bgr}^{ex} considering instrumental contributions to the background and a signal base level A_{bgr}^{el} from elastic scattering of frozen heterogeneities or rather slow dynamics. Table 5.5 sums up the fit values of those contributions. Simulations show that the contribution from experimental background A_{bgr}^{ex} is negligible (Fig. 5.15) and we therefore assume $A_{bgr} \approx A_{bgr}^{el}$.

Under these assumptions the relative contribution of segmental density fluctuations and of elastic scattering can be calculated with Table 5.5. The contribution of the elastic background $A_{bgr} \approx A_{bgr}^{el}$ and the segmental density fluctuations A_S to A_0 are 50% each

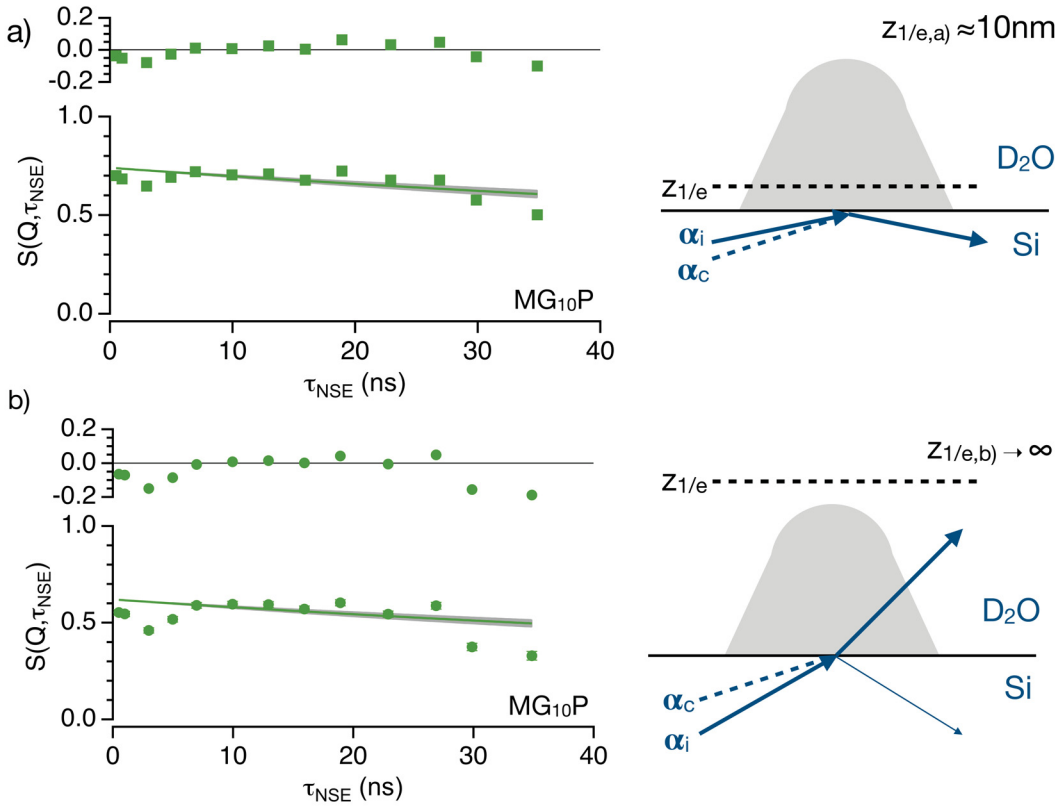

Figure 5.13.: ISFs with confidence interval and corresponding residuals of the batch-microgel $MG_{10}P$ at two different penetration depths. a) Low penetration depth of approximately 10 nm. b) The penetration depth is virtual infinity. For both graphs ISFs were fitted according to equation 5.10.

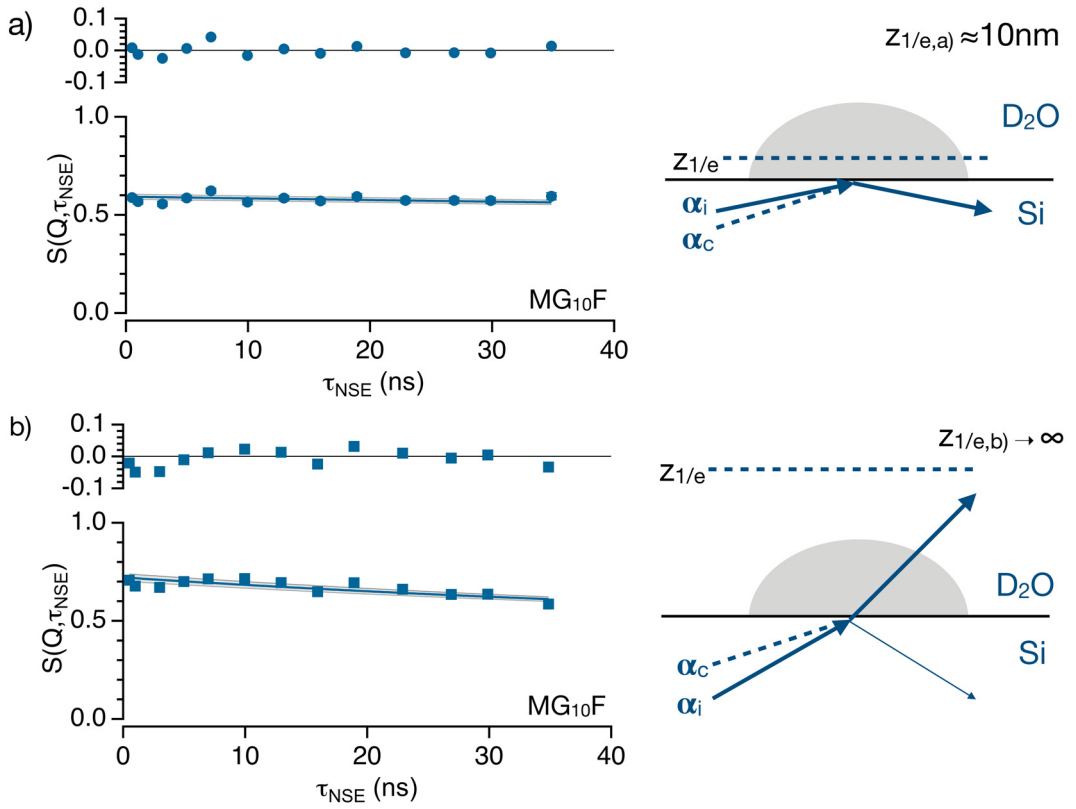

Figure 5.14.: ISFs with confidence interval and corresponding residuals of the feeding-microgel $MG_{10}F$ at two different penetration depths. a) Low penetration depth of approximately 10 nm. b) The penetration depth is virtual infinity. For both graphs ISFs were fitted according to equation 5.10.

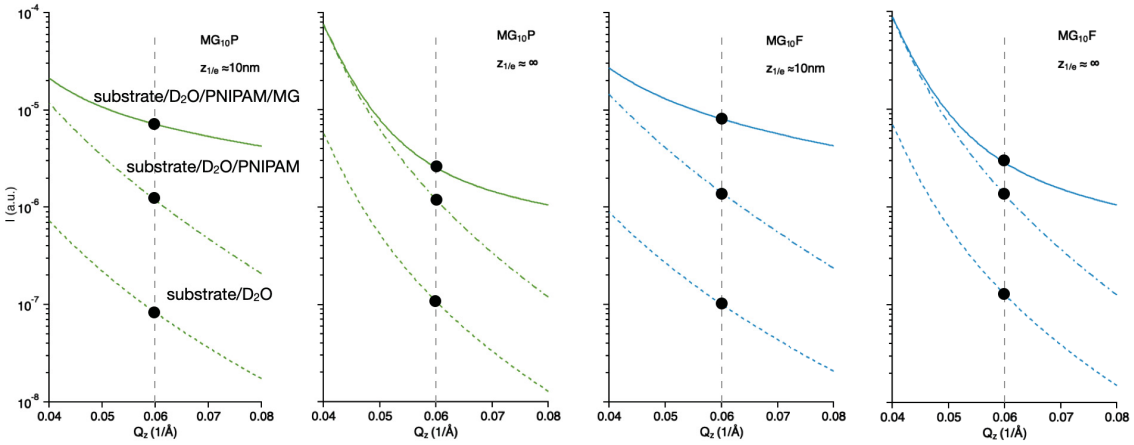

Figure 5.15.: Scattering intensities of different components between $Q = 0.04$ Å^{-1} and $Q = 0.08$ Å^{-1} were calculated with BornAgain. At $Q = 0.06$ Å^{-1} the scattering intensity from the substrate and solvent are two orders of magnitude smaller than the scattering from our samples and are therefore negligible.

Table 5.5.: Details of the fits to the GINSES data of adsorbed $MG_{10}F$ and $MG_{10}P$ microgel particles according to equation 5.10.

Sample	$\mathbf{z}_{1/e}$ **(nm)**	A_0	A_{bgr}	A_s	Γ_c **(ns^{-1})**	Γ_i**(ns^{-1})**
$MG_{10}F$	10	0.60±0.02	0.30±0.09	0.30±0.10	0.003±0.001	–
	∞	0.73±0.01	0.45±0.03	0.28±0.04	0.015±0.003	0.60±0.06
$MG_{10}P$	10	0.62±0.01	0.20±0.10	0.42±0.10	0.010±0.001	0.48±0.04
	∞	0.74±0.01	0.25±0.05	0.49±0.05	0.009±0.002	0.66±0.04

in near-surface layers of the feeding-microgel.

At infinite penetration depth the contribution from elastic scattering increases to 62% and the segmental density fluctuations decrease to 38%. The background of the batch-microgel $MG_{10}P$ behaves differently. Here, in near-surface layers the segmental density fluctuations contribute 68% to A_0, while elastic scattering contributes only 32%. As the entire vertical particle profile is probed these values do not change significantly. In conclusion, the analysis of the experimental background shows that the ISF of the feeding-microgel $MG_{10}F$ contains a higher contribution from elastic scattering where thermal energy does not excite detectable density fluctuations of the polymer network close to the substrate within the time window of the NSE experiment.

In addition, a batch-microgel with a lower cross-linker concentration MG_5P (batch-microgel with 5 mol% BIS) was investigated for comparison. The force map shows a

Table 5.6.: Summary of the diffusion coefficients $D_{coop}=\Gamma_{coop}/Q^2$ and the relative viscosity η_{eff}/η_0. [a] values were taken from Ref. 121

Sample	**measurement**	$\mathbf{z}_{1/e}$ **(nm)**	$\mathbf{D}_{coop}$ **(10^{-7}cm^2/s)**	η_{eff}/η_0
$MG_{10}F$	bulk	-	4.98±0.04[a]	1[a]
	adsorbed	10	0.8±0.2	10
	adsorbed	∞	4.2±0.3	1.2
$MG_{10}P$	bulk	-	2.69±0.02[a]	1[a]
	adsorbed	10	2.8±0.3	1.2
	adsorbed	∞	2.5±1.3	1.2

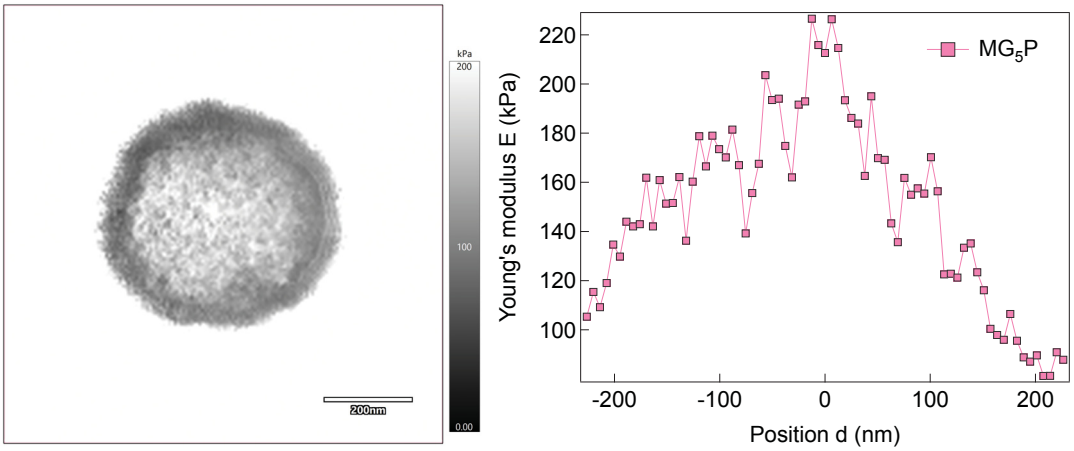

Figure 5.16.: a) Fast force map of MG_5P. b) Corresponding Young's modulus E as a function of the position in the particle.

lateral distribution of elastic moduli comparable with $MG_{10}P$, but with a lower maximum elastic modulus in the center (≈200 kPa) (s. Figure 5.16).

Similar results were found by Aufderhorst-Roberts *et al.*, who described the relation between the elastic modulus and the cross-linker amount with a power law.[122] However, the analysis of ISFs measured by GINSES shows similarities to $MG_{10}F$ (s. Figure 5.17). Near-surface layers show a flat ISF, indicative of suppressed dynamics as a result of interactions with the solid substrate. This indicates that a reduction of cross-linker in batch-microgels changes the structure of near-surface layers, but that the stiffness gradient is preserved regardless.

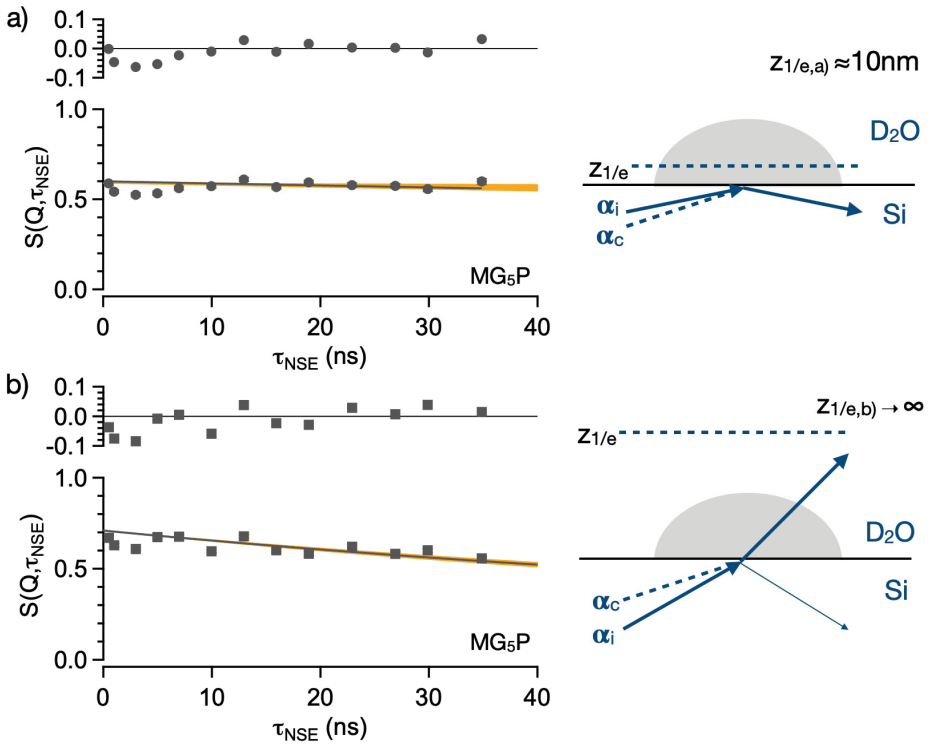

Figure 5.17.: ISFs with confidence interval and corresponding residuals of the batch microgel MG_5P at two different penetration depths. a) Low penetration depth of approximately 10 nm. b) The penetration depth is virtual infinity. For both graphs ISFs were fitted according to equation 5.10.

5.3. Discussion

In summary, we found that highly cross-linked PNIPAM-based microgel particles prepared with a batch and feeding method display differences in their internal structure and internal dynamics. While SANS data for both types of microgels could be fitted with a combination of the Fuzzy sphere model[18] and an Ornstein-Zernike model, fit results showed structural differences. First of all, the feeding-microgel displayed a lower contribution of 1.5% of fuzziness to the overall radius. In comparison, the fuzziness parameter of the batch-microgel contributed 12.5% to the total radius determined by SANS. This is in agreement with the expectation that the feeding method will lead to a more even distribution of cross-links throughout the microgels' polymer network. Furthermore, we found a slightly larger static correlation length ξ for the internal structure of the feeding-microgel. This means that in the feeding-microgel a larger mesh size is dominant. Again, this finding is reasonable. As the microgel core of the batch-microgel is highly cross-linked scattering from the Ornstein-Zernike region is expected to yield a smaller mesh size. When cross-links are distributed more evenly, the distance between them and therefore the mesh size increases. This is furthermore expressed in a higher contribution of the dynamic fluctuations to the scattering signal of the feeding-microgel. Furthermore, we were able to show that the different internal structure affects the internal dynamics in the microgel particles. A highly cross-linked batch-microgel displays cooperative network diffusion over the observed Q-range. In case of the highly cross-linked feeding-microgel above a Q-value of 0.12 Å^{-1}, Zimm-type polymer segment dynamics become observable. This could be related to the fact that for the batch-microgel the highest scattering intensity comes from the polymer dense core region with a smaller static correlation length, favoring this observation. However, in the feeding-microgel the scattering intensity (while lower) comes from a more spaced out distribution of cross-links, enabling the observation of the motion of polymer segments. It is thinkable that we would be able to observe Zimm-type dynamics at higher Q-values for the batch-microgel as well, as shorter lengths would be probed in that case. In fact, we found that we were able to observe Zimm-type dynamics for a batch-microgel with 5 mol% BIS at the Q-values of the NSE experiment. This is likely due to the bigger mesh size of those particles. A detailed analysis of MG_5P was part of the dissertation of Tetyana Kyrey, however the ISFs of this microgel can be found in Figure A.3 in the Appendix. The feeding-microgel furthermore has a higher cooperative diffusion coefficient. Looking at the relation D = E/f it is likely that the smaller fricition experienced by a less polymer

dense network would effectively lead to a higher diffusion coefficient. The dynamic correlation length is smaller for the feeding-microgel. This indicates that the length scale over which dynamic correlations decay in the network increases with increasing cross-linker density. A comparison of the Zimm dynamics observed in a semidilute PNIPAM solution and the feeding-microgel suggests that the influence on the local viscosity is non-negligible.

An elastic contribution to the NSE experiments indicates the presence of inhomogeneities in the network of the microgel particles. Our colaboration partner found evidence of static inhomogeneities in SANS data of PNIPAM microgels with 2 and 5 mol% (compare Chapter 4 of this thesis). They fitted a Gaussian to the data, which is usually used for frozen-in heterogeneities in macrogels. As the NSE data indicate the presence of inhomgeneities, we attempted to approximate the intermediate-Q SANS data with the same model (for details s. Fig. A.4 in the Appendix). For the feeding-microgel we find a static correlation length of $\Xi \approx 80$ nm. This value is 4x the value determined by Kyrey *et al.* for a feeding-mircogel with 5 mol% BIS. For the batch-microgel the static correlation length is much smaller with $\Xi \approx 10$ nm. These inhomogeneities might result from the precipitation polymerization. During the polymerization precursor particles coalesce into colloidally stable primary particles and newly formed precursor particles deposit on the primary particles. Therefore, the elastic contribution and the deviation from the ideal Porod exponent may result from scattering from precursor particles. Differences in the size of those precursor particles can be attributed to the synthesis methods, which differ in parameters such as initial monomer concentration, initial cross-linker concentration, ratio between initiator and monomer/cross-linker. However, a detailed analysis of the polymerization method is beyond the scope of this thesis, but would be interesting for future studies.

Adsorbed batch- and feeding-microgels with 10mol% BIS show clear differences in their nanomechanics and near-surface dynamics. The elastic modulus E of $MG_{10}P$ has a lateral gradient with a maximum value in the particle center. This has been observed by several researchers in the past.[53,118,122] The elastic properties of the feeding-microgel $MG_{10}F$ are more homogeneous and no lateral gradient is observed. This confirms the expectation, that feeding-microgels do not possess a densely cross-linked core, but are more homogeneously cross-linked. Overall, $MG_{10}F$ has a lower elastic modulus, indicative of an overall softer particle. In contrast, Witt *et al.* found that feeding microgels with 2.5 mol% BIS had a higher elastic modulus than equivalent batch-microgels.[53] How-

ever, Witt's study investigated particles prepared with a positively charged comonomer, which might influence the microgels' elastic properties.
Furthermore, the near-surface dynamics of the investigated microgel particles differed for batch- and feeding-microgels. While the batch-microgel appears to have a constant cooperative diffusion coefficient over the entire particle profile, which is identical to the bulk value, the feeding-microgel's near-surface dynamics are suppressed compared to the bulk. This could be explained by deformation upon adsorption, which was observed by Matsui *et al.* with high speed AFM imaging for soft microgels. Since the batch-microgel has a stiff particle core this deformation may not influence those particles upon adsorption.[123] Interestingly, a decrease in the cross-linker fraction of batch-microgels from 10 to 5 mol% leads to the observation of suppressed near-surface dynamics as well. However, the gradient in the elastic modulus measured with AFM force mapping is preserved.
As a result of this investigation, it is questionable whether perceived advantages of feeding-microgels such as a higher loading capacity due to a more homogeneous distribution of cross-links will translate to surface applications. Especially, in cases where a load is applied after adsorption of microgel particles to a solid substrate a fraction of the particle volume might be inaccessible to the load.
However, Matsui *et al.* found that soft deformable microgels attach faster to solid surfaces compared to hard spheres.[123] This can be an advantage in drug delivery where guest molecules are incorporated into the microgel in bulk and those microgels need to adsorb onto diseased sites such as carcinoma.
Our study shows that instrumental improvements such as the installation of super conducting coils at the J-NSE spectrometer facilitate grazing incidence measurements. GINSES measurements remain rather time consuming due to low scattering intensities, but extended measurement durations yield sufficient statistics at two distinct penetration depths. In the future, we recommend the reduction of incoherent background scattering to extend the accessible Q-range.
In general, the combination of AFM force mapping and GINSES provides a possibility to investigate the influence of a solid substrate on the structure and dynamics of even complex polymer architectures.

5.4. Conclusion

The inner structure and dynamics of highly cross-linked PNIPAM microgels in bulk and in the adsorbed state were investigated. In bulk, the network of batch-microgels is inhomogeneous and a high contribution of the fuzziness parameter to the overall radius is observed. In contrast, the network of the feeding-microgel shows a more homogeneous distribution of cross-links with a small fuzziness parameter. These structural differences are reflected in the observed internal dynamics. For the feeding-microgels Zimm-type segmental dynamics were observed in the Q-range of the experiment, while the dynamics of the batch-microgel was purely collective. AFM and GINSES of adsorbed microgel particle show that structural differences influence surface properties as well. While near-surface dynamics of stiff batch-microgels are not influenced by the solid substrate, the near-surface dynamics of feeding-microgels prepared with equivalent fractions of cross-linker are suppressed probably due to the deformation upon adsorption. In the future, an extension of the observable Q-range due to better statistics could yield a more detailed picture of the internal dynamics of adsorbed microgel particles.

6. PNIPAM Brush Dynamics

Abstract

Previously, molecular dynamics studies described the inner dynamics of planar surface-grafted polymer brushes over a wide time-range. Experimentally, slower dynamics (ms-μs) have been investigated by dynamic light scattering, but faster dynamics (ns) could not be accessed until recently. We use neutron spin echo spectroscopy under grazing incidence to investigate the fast inner dynamics of poly(N-isopropylacrylamide) brushes. BornAgain simulations yield intensity maps of the evanescent field and facilitate the calculation of the neutron penetration depth. Our results agree with the non-uniform blob model, meaning that the correlation length increases with the distance from the grafting surface. This trend is observed for polymer brushes with different grafting densities. At equal distance from the grafting-surface, the cooperative correlation length is higher in low density brushes as compared to more dense polymer brushes.

Similar content is published in:

- Witte, J.; Krause, P.; Kyrey, T.; Dahl, A. M.; Lutzki, J.; Schmidt, B. V. K. J.; Ganeva, M.; Kotsioubas, A.; Holderer, O.; Wellert, S. Grazing Incidence Neutron Spin Echo Study of Poly(N-isopropylacrylamide) Brushes. *Macromolecules,* **2020,** *53,* 1819-1830.

The author would like to point out that Patrick Krause prepared the samples presented in this chapter during his master thesis. Furthermore, Patrick Krause presented the initial data analysis in his thesis. The author, Judith Witte, co-advised the master thesis and has completed, extended and improved the data analysis and interpretation of the result. Specifically, Judith Witte contributed the size exclusion chromatography experiments, neutron reflectometry analysis of a diluted brush, and improved fitting procedure of the data from neutron spin echo spectroscopy under grazing incidence with the background contributions from BornAgain simulations.

6.1. Introduction

Polymer brushes are polymer chains that are end-tethered to a surface at a certain grafting density σ, so that the distance between the chains is smaller than the radius of gyration R_g. Alexander and de Gennes published detailed theoretical work on polymer brush structure.[39,124,125] Later, the theoretical picture was extended to the non-uniform blob model.[42,126]
Polymer brush dynamics can be described by thermal fluctuations of the segment density profile.[127] Polymer brush dynamics were first analyzed on spherical polymer brushes using micelle-like aggregation of A-B diblock copolymers.[128] Flat polymer brushes were investigated with evanescent field under total internal reflection, atomic force microscopy and surface force measurements.[129–135] Our focus is the z-resolution of flat polymer brush dynamics with grazing incidence neutron spin echo spectroscopy. This allows a comparison of near-surface dynamics with those toward the bulk phase of the brush.

We synthesized flat polymer brushes on Si-substrates *via* surface initiated ATRP (SI ATRP). The main focus is on the influence of the grafting density on polymer dynamics perpendicular to the grafting surface. The grafting density was varied by initiation of SI ATRP from a self-assembled monolayer (SAM) consisting of different ratios of initiator and unreactive "dummy" molecules. A detailed description of the SI ATRP procedure is given in Chapter 3.1.2 of this thesis. The polymer volume fraction (PVF) was determined by neutron reflectometry. As in the previous chapter, BornAgain was used to model the intensity map of the evanescent field and to simulate the contribution of the substrate to the background.

Changing the grafting density leads to a change of the brush conformation (detailed discussion in Chapter 2.4.2). The experimental determination of the grafting density, however, is challenging. The three most frequently used techniques are determination from dry thickness, gravimetric determination and swelling measurements. None of these techniques is without its faults.[136] We determine the grafting density by dry thickness measurements. This technique requires knowledge of the molecular weight of the polymer chains. Since the "grafting from" approach does not provide bulk polymer, we cleaved polymer brushes and determined their average molecular weight with size exclusion chromatography (SEC) (s. Chapter 3.1.2).

The blob model is frequently used in the theoretical study of polymer brushes.[137] For the analysis of our data we tested whether a uniform or non-uniform blob model applied to the investigated brushes. The shape of the PVF profile and the dynamic correlation length calculated from GINSES experiments support a non-uniform blob size, as the blob size increases with increasing distance from the grafting surface. We further found an influence of the grafting density on the blob-size. The blob size increases with decreasing grafting density.

Attempts to investigate the internal dynamics in polymer brushes were undertaken by Fytas and coworkers as early as 1996.[127] They used evanescent field dynamic light scattering (EW DLS) to probe the collective dynamics in polymer brushes. In early works, they investigated preformed PEO-PS copolymers that were merely adsorbed onto a high-refractive index prism on the PEO end and formed a semidilute brush. EW DLS covers a time scale of 10^{-7} - 10^{3} s. They then fitted the resulting time autocorrelation functions with single exponentials. In a later work, his student Michailidou used EW DLS to investigate PS brushes with different grafting densities (0.02 - 0.2 nm^{-2}), which were now grafted-from the high refractive index prism. Michailidou found that an increase in grafting density led to faster dynamics in the brush.[133] EW DLS was also used to investigate colloids near a wall and the effective drag forces.[138,139] Those investigations showed that a higher concentration of colloids decreased the hydrodynamic interaction between particle and wall, because the particle-particle hydrodynamic interactions increased.[139] These finding might be interesting if related to the interactions of surface blobs with a solid surface.

Another technique that has been used to investigate surface dynamics is X-ray photo correlation spectroscopy (XPCS). Surface XPCS is used to probe surface capillary waves of complex fluids and thin polymer films. Tolan *et al.* used glycerol as a model system. This technique is limited by the small-wave vectors accessible and therefore the lateral resolution cannot go down to the nm-range.[140] Sun *et al.* used XPCS measurements on PS brushes of different grafting densities (0.04 - 0.6 nm^{-2}), but couldn't observe surface fluctuations in the time and length scale accessible with XPCS.[141] X-ray scattering within a film suffers from low contrast. However, the application of nanoparticles and the investigation of their mobility within a thin polymer film have been used to indirectly study the internal film viscosity.[142]

Frielinghaus used GINSES to investigate tribological effects in microemulsions on the molecular level.[88] In his study on the dynamics in microemulsions, as an example for a complex fluid, he stresses the possibility of depth profiling with grazing incidence scattering techniques. He found faster dynamics at the solid surface than toward the bulk phase. Wellert *et al.* applied GINSES conditions to PEG copolymer brushes.[86] They found that measurements at a Q-value of 0.05 Å^{-1} showed the relaxation of the system, while at $Q = 0.08$ Å^{-1} the incoherent background scattering was too dominant and a flat line was recorded. The data was fitted with a stretched exponential to take into consideration Zimm-type segmental dynamics. Due to the scattering geometry they were able to investigate two neutron penetration depth namely 35 nm and infinity. They observed a slowing down of the dynamics with increasing penetration depth. In conclusion they argue that the relaxation time of the thermal fluctuations is proportional to the blob size.

In this work, the author aims at studying the internal dynamics in polymer brushes with neutron spin echo spectroscopy under grazing incidence conditions. The advantages are the observability of ns-time and nm-length scales. In contrast to EW DLS, GINSES allows to measure in a more surface sensitive manner. Furthermore, using deuterated water as a solvent for the polymer brushes creates high contrast between silicon, polymer brush and solvent. This allows the investigation of dynamics within the polymer film, which is problematic for X-ray scattering due to low contrast.

6.2. Results

First, ellipsometry measurements in air were conducted to investigate the reaction kinetics of the chosen SI ATRP conditions by tracking the brush growth over time. Figure 6.1 shows that while the SI ATRP of NIPAM is generally fast, a reduction of the amount of monomer by half significantly decreases brush growth.

6.2.1. Determination of the Grafting Density

From SEC measurements of cleaved polymer brushes we obtain the number average (M_n), weight average (M_w) and peak (M_p) molecular weight of the polymer chains. Furthermore, we can calculate the molecular dispersity $Đ$ according to

$$= \frac{M_w}{M_n}. \tag{6.1}$$

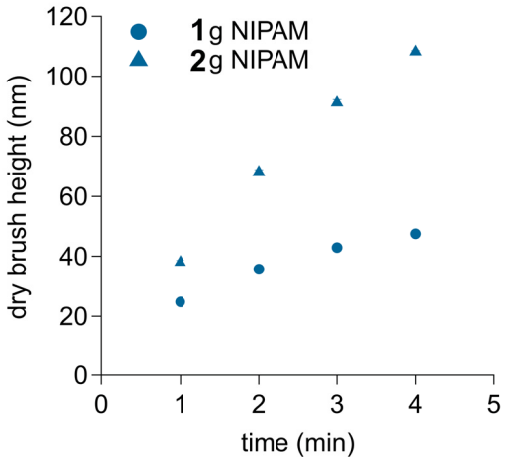

Figure 6.1.: Polymer brush growth with different amounts of monomer.

Table 6.1.: Number average M_n, weight average M_w, peak M_p molecular weigth and molar dispersity $Đ$ resulting from SEC measurements.

Sample	**Peak**	M_n **[g/mol]**	M_w **[g/mol]**	M_p **[g/mol]**	$Đ$
PNIPAM 1:0	1	1300	1500	1100	1.2
PNIPAM 1:0	2	40500	58800	52000	1.5
PNIPAM 1:0.2	1	2700	3700	1900	1.4
PNIPAM 1:0.2	2	46500	69000	61800	1.5

The UV detector shows higher intensities than the RI detector (s. Figures A.8 and A.9 in the Appendix). The SEC results are listed in Table 6.1. The bimodal molar mass distribution indicates polymer chains of different lengths present at the grafting surfaces, namely shorter and longer ones. Such a distribution can indicate two phenomena during SI ATRP: (1) shielding of reaction sides by growing chains and (2) termination by disproportionation. We assume that only the longer chains contribute to the brush confirmation as they mainly contribute to the dry thickness of the brush and neglect the shorter chains during the determination of the grafting density. With the dry film thickness from ellipsometry, we can therefore determine the grafting density according to

$$\sigma = \frac{\rho_M N_A h_{dry}}{M_n}, \tag{6.2}$$

with ρ_M the density of the monomer, N_A Avogadro's constant and h_{dry} the height of the dry polymer brush.

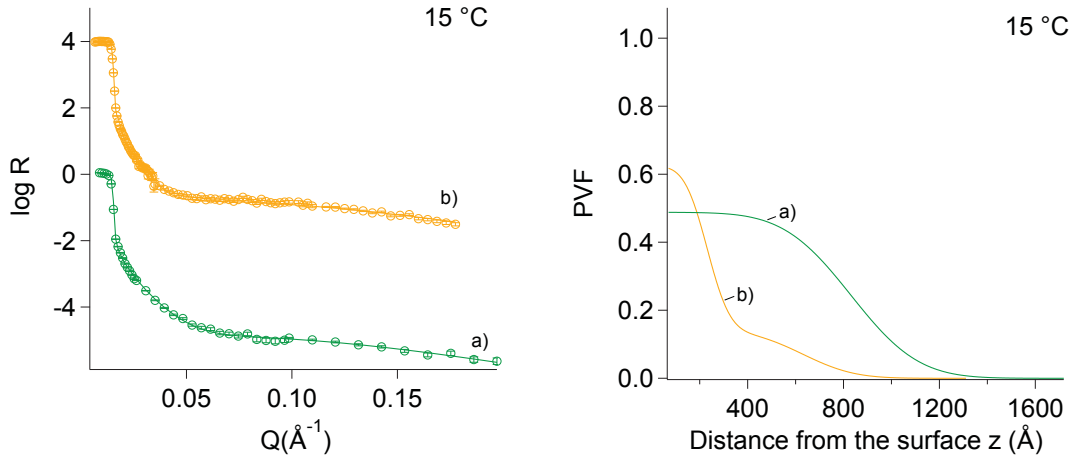

Figure 6.2.: Neutron reflectivity curves and PVF of PNIPAM brushes at 15 °C. a) is the maximum grafting density ($\sigma \approx 1.0$ nm^{-2}), b) is the low grafting density ($\sigma \approx 0.6$ nm^{-2}).

The samples that were used for SEC measurements had an average thickness of 61 nm (PNIPAM 1:0) and 42 nm(PNIPAM 1:0.2). Therefore, the average grafting densities are $\sigma_{1:0}$=1.0 nm^{-2} and $\sigma_{1:0.2}$=0.6 nm^{-2}. While the low detector signal and the bimodal mass distribution pose a challenge, the calculated grafting densities are in good agreement with theoretical calculations.

6.2.2. Polymer Volume Fraction Profiles

Polymer volume fraction profiles were calculated from neutron reflectivity data. Fits to the data provide three parameters: layer thickness, solvent content and roughness. Assumption of a single brush layer sufficed for data analysis of the densest brush. The layer thickness was 81 nm with a solvent content of 51% v/v.

However, for the less dense brush fit quality profited from the assumption of two distinctive brush layers. Examples of the fit to the data with one layer can be found in Figure A.6 in the Appendix. The assumption of two distinct layers is in agreement with quantitative *in situ* ellipsometry studies by Kooij *et al.* in Reference 143. One layer close to the surface was 20 nm thick and contained 38% v/v solvent. On top of that the second layer was 40 nm thick and contained 86% v/v solvent. Furthermore, this result can be explained in the context of theoretical considerations by Descas *et al.* The polymer chains feel attraction to the surface. If the grafting density is sufficiently

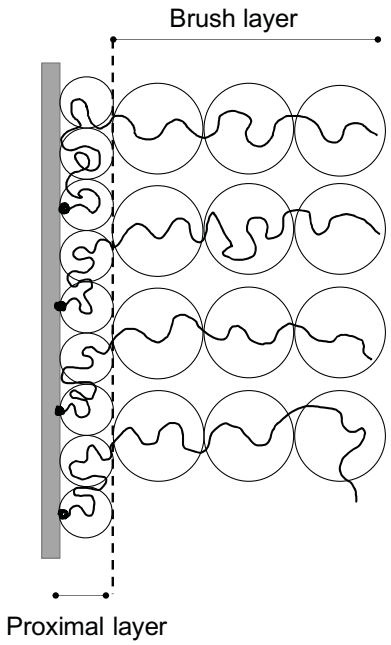

Figure 6.3.: Sketch of the oversaturated brush regime as envisioned by Descas *et al.* in Ref. 144. Chain segments from the proximal layer adsorb onto the substrate, followed by the brush layer.

low, the surface isn't as crowded and segments of the growing polymer chain can adsorb onto the surface. However, the grafting density is still sufficiently high and therefore the growing polymer chains are in a brush conformation. The polymer rich layer closer to the substrate is called the proximal layer, and all together Descas calls this regime the oversaturated brush regime (OSB). A sketch of the OSB is shown in Figure 6.3. In case of the denser brush, due to the higher osmotic pressure, the chains can not adsorb to the surface and the proximal layer is not observed.[144]

The reflectivity curves do not display distinct Kiessig fringes due to the smooth transition between the brush layer and the solvent. This smooth transition is taken into account by the layer roughness. The layer towards the solvent phase has a similar roughness of about 20 nm for both brushes.

As the brushes collapse with increasing temperature, Kiessig fringes appear in the reflectivity curves of both samples (s. Figure A.7 in the Appendix). In the collapsed state both curves can be fitted with a three layer model. This can be explained as

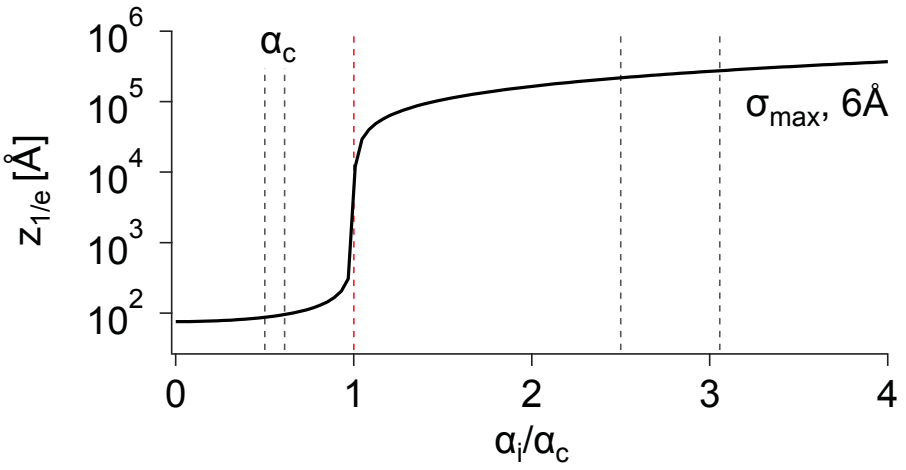

Figure 6.4.: Neutron penetration depth $z_{1/e}$ at a neutron wavelength of 6 Å as calculated by equation 3.40.

follows. As the polymer brush expels water, the outer layer collapses onto the inner layer. Now fit results indicate a thickness of the polymer brush of 28 nm and a water content of 35 % v/v. Therefore, most of the water is expelled from the outer layer and the additional 8 nm in brush thickness can be accounted to the outer layer which collapsed on top. The denser brush collapses to a thickness of 54 nm and expels water until a solvent content of 38 % v/v remains in the brush layer.

6.2.3. Internal Dynamics

Calculation of the Neutron Penetration Depth

Figure 6.4 displays the neutron penetration depth calculated according to equation 3.40 in relation to the angle of incidence α_i normalized by the critical angle α_c for different wavelength. The vertical dashed lines indicate the distribution of 20% that is dealt with on the J-NSE instrument. It becomes apparent that the distribution increases with increasing wavelength. It is noteworthy that this distribution does not affect the measurements as strongly if the angle of incidence is sufficiently different from the critical angle. However, the closer the angle of incidence gets to the critical angle, the less accurately the penetration depth $z_{1/e}$ can be determined. Therefore, measurements around the critical angle are difficult to interpret.

Modern computer simulation with BornAgain allow us to draw a more accurate pic-

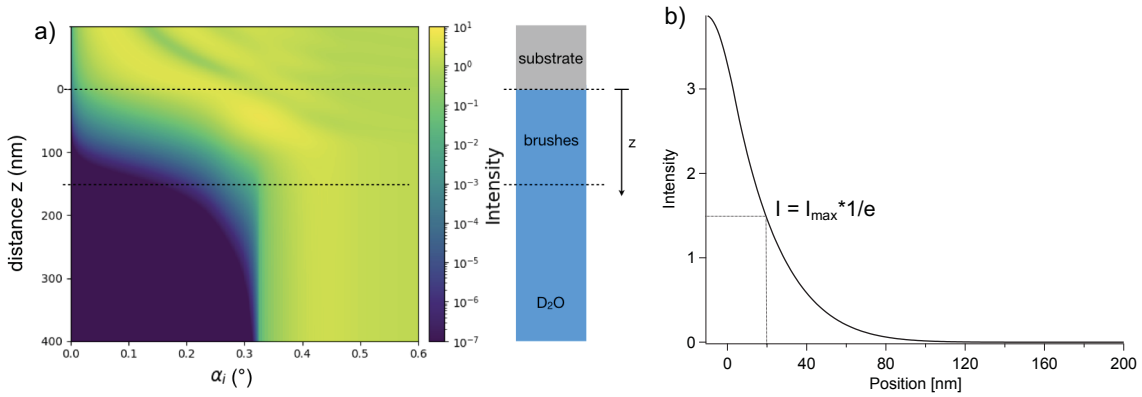

Figure 6.5.: Simulated map of the evanescent field intensity (a) and line-cut thereof (b). BornAgain simulations by Tetyana Kyrey.

ture of the intensity distribution of the evanescent field. Figure 6.5 a displays a two-dimensional map of the intensity distribution of the evanescent field. This is based on the PVF profile obtained from neutron reflectometry measurements. The variation of the intensity of the evanescent field is displayed against the angle of incidence and the distance from the scattering plane. If we now make a cut through this map at our chosen angle of incidence, we obtain the graph shown in Figure 6.5 b. This graph displays the intensity of the evanescent field against the position in the brush. The position that corresponds to the intensity value where the intensity has decreased to 1/e is called the neutron penetration depth $z_{1/e}$.

A comparison between the results from the calculation according equation 3.40, and the BornAgain simulations yields higher values for the neutron penetration depth from BornAgain simulations, namely 25 and 16 nm, respectively. However, the measurements would still are within the first 20-30% of the brush layer coming from the planar solid substrate. As we have learned from reflectivity measurements the dense layer has a thickness of 20 nm, which means that we are still measuring within that layer, but rather towards its outer edge.

Background Subtraction

As was mentioned before, background subtraction for grazing incidence experiments is not as straight forward as in transmission geometry. As the neutron penetration depth depends on the SLD setup of the sample under investigation this will change if we have

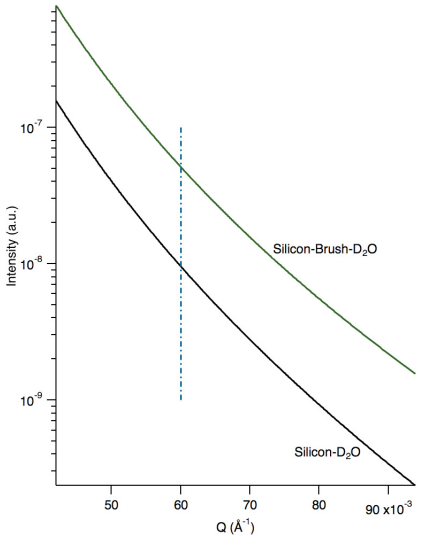

Figure 6.6.: Simulation of the background intensity versus the scattering intensity of the sample.

the substrate-brush-solvent versus the substrate-solvent. In this instance the simulation of the scattering intensity with BornAgain for the brush-silicon interface and the D_2O can help to estimate the contribution of the substrate to the elastic background in the scattering signal.

Figure 6.6 compares the simulated background intensities of the silicon-D_2O interface and the silicon-brush-D_2O interface as a function of the momentum transfer. At $Q = 0.06$ Å^{-1} the ratio is approximately 1:0.2. Therefore, 20% of the elastic background baseline is due to instrumental background and 80% can be attributed to slow or frozen dynamics in the sample.

Intermediate Scattering Functions

ISFs of two brush samples are displayed in Figures 6.7 and 6.8. Fits to the ISFs reveal that the relaxation rate Γ_c depends on the grafting density and the neutron penetration depth. Figure 6.9 displays the cooperative correlation length ξ_{coop} as a function of the neutron penetration depth for both brush samples. For the dense brush the correlation length of the layer close to the substrate is 2.8 nm and increases to 5.2 nm towards the bulk phase. For the less dense brush we were able to measure at three angles of incidence. However, because of the wavelength resolution of 20%, the angle of incidence

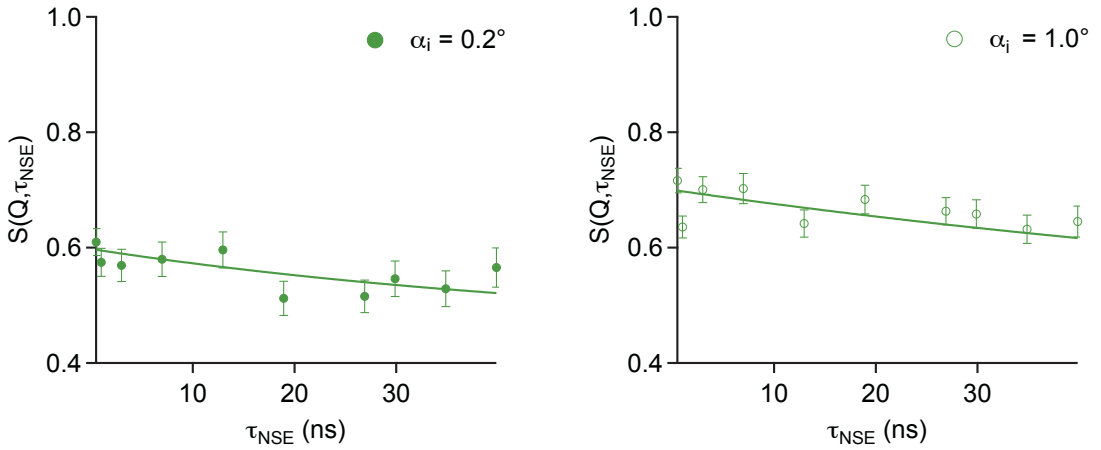

Figure 6.7.: Intermediate scattering function for the densest brush at two angles of incidence, measured during the first beam time.

close to the critical angle needs to be treated with caution. The cooperative correlation length ξ_{coop} increases with the neutron penetration depth from 6.4 to 16 to 26 nm.

These findings are in agreement with the structural considerations that arose from neutron reflectivity curves. As the correlation length is proportional to the blob size and the adsorbed blob size in the proximal layer is expected to be smaller than the blob size in the brush layer. The difference is less pronounced for the denser brush, because there is no distinctive proximal layer. We observe a correlation length of 2.8 nm in the near-surface layer and 5.2 nm toward the bulk of the brush.

The ISF of the low grafting density brush close to the surface displays an initial incline up to a Fourier time of 4 ns. This feature can be attributed to incoherent scattering from hydrogen atoms. The single exponential decay can be extended to the following

$$S(Q, \tau_{NSE}) = (A - A_{bgr})(1 - e^{-\Gamma_i \tau_{NSE}})e^{-\Gamma_c \tau_{NSE}} + A_{bgr}. \tag{6.3}$$

From the incoherent part we obtain a diffusion coefficient of 4 x 10^{-9} m^2/s. This is in agreement with a simulation study by Longhi *et al.*, who found values between 3.8 x 10^{-9} m^2/s and 6.6 x 10^{-9} m^2/s for first-shell water molecules surrounding PNIPAM chains.[145] Therefore, one explanation for the incoherent contribution to the scattering signal is the formation of hydrogen bonds between PNIPAM and water molecules. As was shown by the neutron reflectivity curves, more PNIPAM is present in closer vicinity to the substrate and therefore the contribution of first-shell protonated water would be

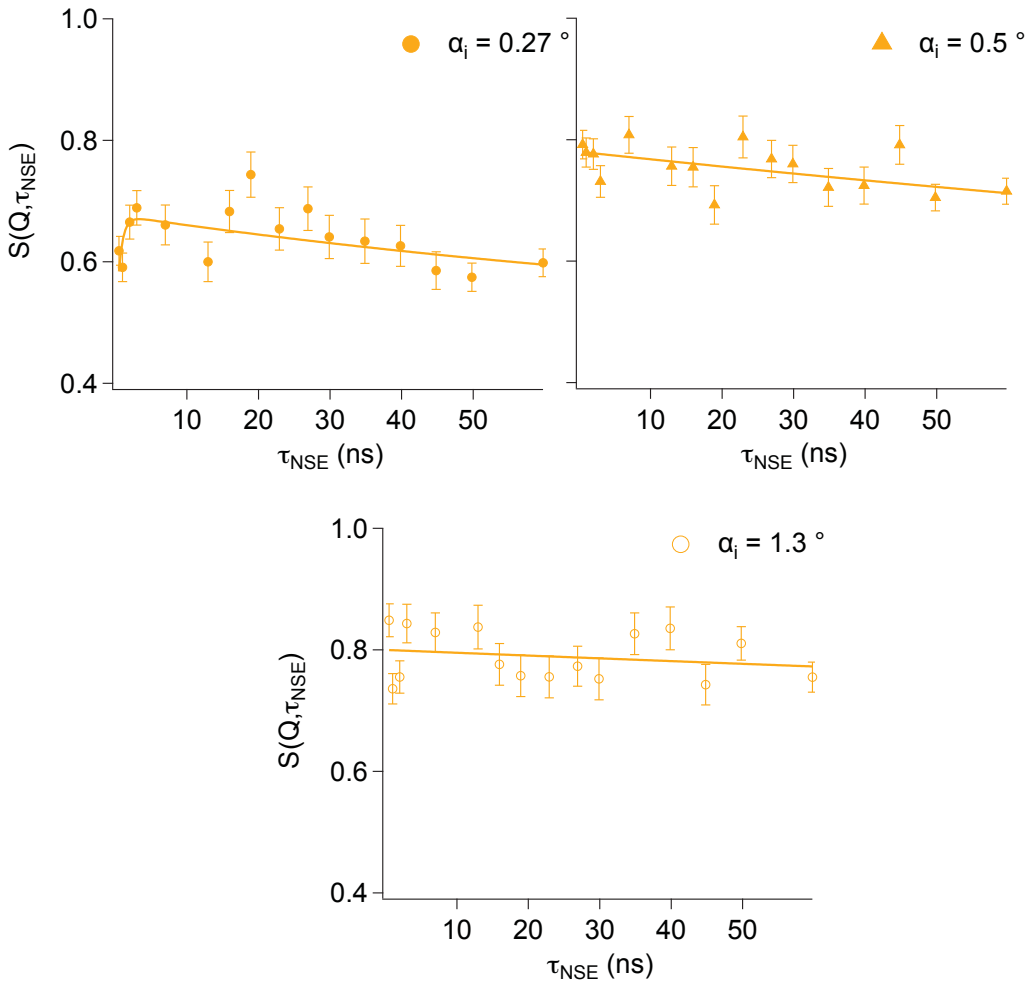

Figure 6.8.: Intermediate scattering function for the least dense brush at three angles of incidence, measured during the second beam time.

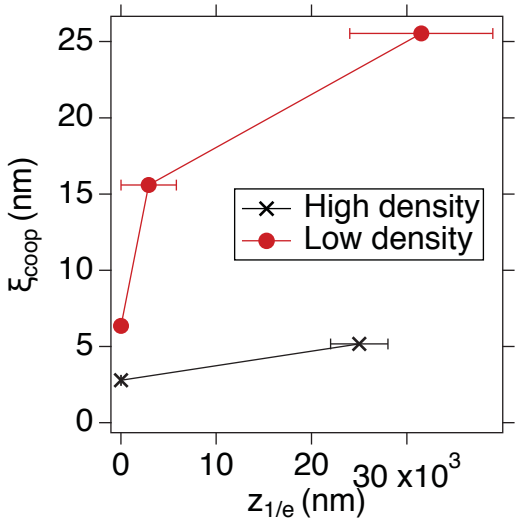

Figure 6.9.: Cooperative correlation length ξ_{coop} as a function of the neutron penetration depth $z_{1/e}$ for both brushes. The y-error represents the uncertainty in neutron penetration depth due to the instrument resolution.

the highest in a lower grafting density at small angles of incidence. The data supports this suggestion.

6.3. Discussion

Prior studies have investigated the inner dynamics of polymer brushes using techniques such as EW DLS, surface XPCS and even GINSES. Wellert *et al.* were able to show the feasibility of GINSES measurements in PEG copolymer brushes. However, GINSES is still a relatively young field and not many systems have been investigated with this technique. Due to constant instrumental improvements this field is promising.

In this study, we investigated inner dynamics of PNIPAM brushes in two different density regimes and used BornAgain simulations to understand better (i) the penetration of the evanescent field into our sample and (ii) the contribution of the background to the data.

First, we investigated the dynamics of a dense polymer brush at two different neutron penetration depths and found that the relaxation rate decreases further away from the grafting surface. This is in agreement with the previous feasibility study on PEG copoly-

mer brushes.[86] However, we extended our study to a brush with a lower grafting density to better understand the influence of the grafting density on the surface dynamics. For the investigated neutron penetration depths we found a lower relaxation rate in polymer brushes with lower grafting densities. This is in agreement with EW DLS experiments by Michailidou of PS brushes. Our correlation length compare well to those found by Michailidou.[133]

In contrast to GINSES data for PEG copolymer brushes, we observed an incoherent contribution to the scattering signal at low Fourier times. A fitting of the data revealed diffusion coefficients that compare well to simulated values found for first-shell protonated water.[145] This can be explained by the formation of hydrogen bonds within PNIPAM networks. In a KF titration we determined 15% residual water in microgel particles of different cross-linker content (2 - 10 mol%). However, this incoherent contribution is only relevant at lower Fourier times and does not influence our results.

One aspect that distinguishes our work from previous GINSES studies on polymer brushes is the simulation of the intensity map of the evanescent field. This allows us a better evaluation of the penetration depth of the evanescent field into our sample. Since these simulations are based on actual NR data from the sample, the adsorption of the sample is taken into account. Furthermore, we can simulate the contribution of the experimental background. This is highly challenging in GINSES experiments due to the different SLD profile of a coated and a bare silicon block against D_2O, which influences the penetration depth of the measurement.

An interesting perspective for future studies is the use of a resonator block to increase the intensity of the signal. We have successfully grafted PNIPAM brushes from such resonator substrates and ellipsometry measurements of the grafted chains on the wafers suggest a similar growth as on silicon substrates (compare Fig. A.10 in the Appendix). Ideally, in the future a higher signal intensity allows the reduction of the wavelength distribution and therefore the measurement of incidence angles closer to the critical angle of total external reflection. Another possibility that occurs with increased signal intensity is the option to measure at different Q-values. Currently, this is not feasible due to the ratio of coherent and incoherent scattering approaching 1 at higher Q-values. Although there is the option of separating the detector image into several Q-values and analyze them separately, this is not feasible yet, because of poor statics. One has to

average over the entire detector to receive sufficient signal. As neutron beam time is valuable, it is not realistic to count longer and an improvement in signal intensity is the only viable option.

6.4. Conclusion

In this chapter, GINSES measurements were successfully conducted on PNIPAM brushes with different grafting densities. Dynamics of near-surface and bulk layers were observed and it was shown that the dynamics change with the grafting density. BornAgain simulations allowed the estimation of the penetration depth and the contributions to the background. From NR and GINSES measurements it is concluded that a non-uniform blob model describes the polymer brushes. The excluded volume increases with increasing distance to the grafting surface.

7. Conclusion and Future Perspective

This thesis investigated the structure-dynamics relations of cross-linked (microgels) and non-cross-linked (polymer brushes) soft matter systems. All investigated systems were based on *N*-isopropylacrylamide. Structural features were thoroughly investigated with laboratory scale methods (dynamic light scattering, ellipsometry, atomic force microscopy) and at large-scale research facilities (neutron scattering methods such as neutron reflectometry and small angle neutron scattering). Furthermore, dynamics investigations were conducted with neutron spin echo spectroscopy in transmission mode and under grazing incidence. The focus lay on the investigation of the influence of the solid planar surface on the dynamics in soft matter systems.

Influence of the preparation method of PNIPAM microgels (batch vs. continuous) on bulk and surface properties

The first study was concerned with the preparation of batch- and feeding-microgels with molar fractions of cross-linker between 2 and 10 mol%. Microgels were prepared with a positively charged thermal initiator (AAPH), but without an additional charged co-monomer to prepare a simple model system. The preparation by surfactant-free precipitation polymerization in a continuous monomer feeding method showed limitations for a low molar fraction of cross-linker of 2 mol%. Here, no colloidal particles could be observed with the common methods such as DLS and AFM. However, this limitation was not observed for batch-microgels.

Feeding-microgels with a degree of cross-linking of 5 and 10 mol% showed swelling behavior, hydrodynamic radius and volume phase transition temperature comparable with those of batch-microgels. However, feeding-microgels displayed slightly higher swelling ratios and higher VPTTs. Major differences between feeding- and batch microgels were observed in the adsorbed state. Feeding-microgels collapsed stronger onto the surface, which resulted in extremely high aspect ratios (w/h) in the dry state. The aspect ratios remained rather high after reswelling in water. Feeding-microgels with 10 mol% cross-linker had the lowest aspect ratios and hence were deemed most suitable to resolve the difference between near-surface layers and the averaged particle properties. Hence,

microgel particles with 10 mol% cross-linker were chosen for further studies.

Influence of the preparation method on internal structure and dynamics in highly cross-linked microgels

The second study was subdivided into two substudies. In the first substudy, the internal structure and dynamics of highly cross-linked microgels were investigated in bulk. Small angle neutron scattering revealed differences in the internal structure. It was shown that feeding-microgels possess a significantly lower fuzziness parameter and a slightly larger correlation length. Since the correlation length is related to the mesh size of the polymer network, a larger mesh size is dominant in the feeding-microgels. Those results nicely fit to the more even distribution of cross-links. Neutron spin echo spectroscopy in transmission mode revealed the differences in internal dynamics. While the batch-microgels showed cooperative diffusion over the entire Q-range of the experiment, the feeding-microgels showed a transition to Zimm-type dynamics at $Q = 0.12$ Å^{-1}. Therefore, the motion of polymer segments could be observed for feeding-microgels, but not for batch-microgels. Further, feeding-microgels have a higher cooperative diffusion coefficient. This was explained by the lower friction experienced by a less dense polymer network compared to the batch-microgels. A comparison of the Zimm-type dynamics of a semidilute PNIPAM solution and the feeding-microgels showed that the influence of the polymer network on the local viscosity is non-negligible.
In the second substudy, nanomechanics and internal dynamics of PNIPAM microgels in the adsorbed state were investigated. Nanoindentation measurements with the AFM below the VPTT showed that the elastic modulus in the center of feeding-microgels is much lower than in the center of batch-microgels. However, above the VPTT, hence in the collapsed state, the elastic moduli are the same. The lateral distribution of the elastic modulus was further investigated with fast force mapping. As expected, batch-microgels displayed a stiffness gradient, which was absent in feeding-microgels. GINSES experiments revealed that the near-surface dynamics (approximately 10 nm into the monolayer) were not influenced by interactions with the surface. Calculated diffusion coefficients compared well to the bulk value. However, the near-surface dynamics of feeding-microgels were severely damped by the interactions with the solid substrate. This finding has implications on the suitability of feeding-microgels for certain surface applications.

Influence of the grafting density on the blob size in polymer brushes

The third study investigated the influence of the grafting density on the structure and dynamics of PNIPAM brushes. Polymer volume fraction profiles of a brush in the concentrated regime (σ=1.0 nm^{-2}) and in the semidilute regime (σ=0.6 nm^{-2}) were extracted from neutron reflectivity curves. The concentrated brush was best described by a model with one brush layer, while the semidilute brush demanded two distinct brush layers. This was explained by the osmotic pressure between the polymer chains. In a concentrated brush the osmotic pressure is sufficiently high to counterbalance the attraction of near-surface layers to the surface. As the grafting-density is decreased, so is the osmotic pressure and a so-called proximal layer is formed. It was shown that the determination of the grafting density by degrafting and subsequent SEC is mainly challenged by low sample volumes and hence low signal intensity. A GINSES study similar to the one in the second study of this thesis was conducted on both polymer brushes. It was shown that the correlation length, which is related to the blob size, increases with increasing distance to the grafting surface. The decrease of the grafting density resulted in increased correlation length (hence blob sizes). Therefore, this study provides experimental evidence in favor of the non-uniform blob model.

Future perspective

As mentioned in the introduction, neutron spin echo spectroscopy under grazing incidence is a valuable addition to the toolbox for the characterization of the dynamics of adsorbed soft matter samples. The results of this thesis contribute to the field. While the method is able to provide interesting results, there is room for improvement. First and foremost, research efforts should be put toward the improvement of the signal-to-noise ratio in GINSES experiments. This allows access to larger Q-values and therefore extended information about a system's dynamics on more local length scales could be gained. The improvement of the sample cell (decrease of experimental background), instrumental improvements or the use of a resonator block should be considered. Further, future developments in the realm of computer simulations with BornAgain will contribute to better background subtraction and calculation of the penetration depth. Furthermore, the simulations can aid the z-resolution of the dynamics profile, because they contain information on the contribution to the signal by different layers.
However, it is not only instrumental changes that should be considered. The measurement of other, more complex, adsorbed soft matter systems or even hybrid systems would yield interesting information on the dynamics in such systems. In the future, we plan on publishing work on zwitterionic polymer brushes, a class of polymer brushes that is

interesting in biological applications such as cell cultivation and antifouling coatings. In general, biocompatible and biodegradable polymers are becoming more important due to health and environmental concerns. The author hopes that the fundamental understanding of those systems can be extended in the future with the methods used in this thesis.

Bibliography

[1] S. R. Nagel. Experimental Soft-Matter Science. *Rev. Mod. Phys.*, 89:025002, 2017.

[2] M. Rubinstein and R. H. Colby. *Polymer Physics*. Oxford University Press, 2003.

[3] A. Halperin, M. Kröger, and F. M. Winnik. Poly(N-isopropylacrylamide) Phase Diagrams: Fifty Years of Research. *Angew. Chem. Int. Ed.*, 54:15342–15367, 2015.

[4] P. E. Rouse Jr. A Theory of the Linear Viscoelastic Properties of Dilute Solutions of Coiling Polymers. *The Journal of Chemical Physics*, 21:1272–1280, 1953.

[5] B. H. Zimm. Dynamics of Polymer Molecules in Dilute Solution: Viscoelasticity, Flow Birefringence and Dieelectric Loss. *The Journal of Chemical Physics*, 24:269–278, 1956.

[6] J. Brijitta and P. Schurtenberger. Responsive Hydrogel Colloids: Structure, Interactions, Phase Behaviours, and Equilibrium and Non-Equilibrium Transitions of Microgel Dispersions. *Curr. Opin. Colloid Interface Sci.*, 40:87–103, 2019.

[7] B. R. Saunders and B. Vincent. Microgel Particles as Model Colloids: Theory, Properties and Applications. *Adv. Colloid Interface Sci.*, 80:1–25, 1999.

[8] A. Fernández-Nieves, H. M. Wyss, J. Mattsson, and D. A. Weitz, editors. *Microgel Suspensions: Fundamentals and Applications*. Wiley-VCH Verlag GmbH & Co. KGaA, 2011.

[9] G. M. Conley, P. Aebischer, S. Nöjd, P. Schurtenberger, and F. Scheffold. Jamming and Overpacking Fuzzy Microgels: Deformation, Interpenetration, and Compression. *Sci. Adv.*, 3:1700969, 2017.

[10] G. M. Conley, C. Zhang, P. Aebischer, J. L. Harden, and F. Scheffold. Relationship between Rheology and Structure of Interpenetrating, Deforming and Compressing Microgels. *Nat. Commun.*, 10:1–8, 2019.

[11] C. Royall, W. Poon, and E. Weeks. In Search of Colloidal Hard Spheres. *Soft Matter*, 9:17–27, 2013.

[12] M. Stieger, J. S. Pedersen, P. Lindner, and W. Richtering. Are Thermoresponsive Microgels Model Systems for Concentrated Colloidal Suspensions? A Rheology and Small-Angle Neutron Scattering Study. *Langmuir*, 20:7283–7292, 2004.

[13] T. Eckert and W. Richtering. Thermodynamics and Hydrodynamic Interaction in Concentrated Microgel Suspensions: Hard or Soft Sphere Behavior? *The Journal of Chemical Physics*, 129:124902, 2008.

[14] R. H. Pelton and P. Chibante. Preparation of Aqueous Latices with *N*-isopropylacrylamide. *Colloids and Surfaces*, 20:247–256, 1986.

[15] R. Pelton. Temperature-Sensitive Aqueous Microgels. *Advances in Colloid and Interface Science*, 85:1–33, 2000.

[16] E. Kutnyanszky, A. Embrechts, M. A. Hempenius, and G. J. Vansco. Is There a Molecular Signature of the LCST of Single PNIPAM Chains as Measured by AFM Force Spectroscopy. *Chem. Phys. Lett.*, 535:126–130, 2012.

[17] X. Wu, R. H. Pelton, A. E. Hamielec, D. R. Woods, and W. McPhee. The Kinetics of Poly(*N*-isopropylacrylamide) Microgel Latex Formation. *Colloid Polym. Sci.*, 272:467–477, 1994.

[18] M. Stieger, W. Richtering, J. S. Pedersen, and P. Lindner. Small-Angle Neutron Scattering Study of Structural Changes in Temperature Sensitive Microgel Colloids. *The Journal of Chemical Physics*, 120:6197–6206, 2004.

[19] B. R. Saunders. On the Structure of Poly (*N*-isopropylacrylamide) Microgel Particles. *Langmuir*, 20(10):3925–3932, 2004.

[20] A. Fernández-Barbero, A. Fernández-Nieves, I. Grillo, and E. López-Cabarcos. Structural Modifications in the Swelling of Inhomogeneous Microgels by Light and Neutron Scattering. *Physical Review E*, 66:051803, 2002.

[21] B. Sierra-Martin, J. R. Retama, M. Laurenti, A. Fernández-Barbero, and E. López Cabarcos. Structure and Polymer Dynamics within PNIPAM-Based Microgel Particles. *Adv. Colloid Interface Sci.*, 205:113–123, 2014.

[22] S. Meyer and W. Richtering. Influence of Polymerization Conditions on the Structure of Temperature-Sensitive Poly(*N*-isopropylacrylamide Microgels. *Macromolecules*, 38:1517–1519, 2005.

[23] R. Acciaro, T. Gilányi, and I. Varga. Preparation of Monodisperse Poly(*N*-isopropylacrylamide) Microgel Particles with Homogeneous Cross-Link Density Distribution. *Langmuir*, 27:7917–7925, 2011.

[24] H. Wolff, M. Kather, H. Breisig, W. Richtering, A. Pich, and M. Wessling. From Batch to Continuous Precipitation Polymerization of Thermoresponsive Microgels. *ACS Appl. Mater. Interfaces*, 10:24799–24806, 2018.

[25] R. C. Advincula, W. J. Brittain, and K. C. Caster. *Polymer Brushes*. John Wiley & Sons, 2004.

[26] A. A. Brown, O. Azzaroni, L. M. Fidalgo, and W. T. S. Huck. Polymer Brush Resist For Responsive Wettability. *Soft Matter*, 5:2738–2745, 2009.

[27] L. Wen, Y. Tian, and L. Jiang. Bioinspired Super-Wettability from Fundamental Research to Practical Applications. *Angew. Chem. Int. Ed.*, 54:3387–3399, 2015.

[28] Y. Higaki, M. Kobayashi, D. Murakami, and A. Takahara. Anti-Fouling Behavior of Polymer Brush Immobilized Surfaces. *Polym. J.*, 48:325–331, 2016.

[29] C. Rodriguez-Emmenegger, E. Brynda, T. Riedel, M. Houska, V. Subr, A. B. Alles, E. Hasan, J. E. Gautrot, and W. T. S. Huck. Polymer Brushes Showing Non-Fouling in Blood Plasma Challenge the Currently Accepted Design of Protein Resistant Surfaces. *Macromol. Rapid Commun.*, 32:952–957, 2011.

[30] R. A. E. Wright, K. K. Wang, J. Qu, and B. Zhao. Oil-Soluble Polymer Brush Grafted Nanoparticles as Effective Lubricant Additives for Friction and Wear Reduction. *Angewandte Chemie*, 128:8798–8802, 2016.

[31] H. Sakata, M. Kobayashi, H. Otsuka, and A. Takahara. Tribological Properties of Poly(methyl methacrylate) Brushes Prepared by Surface-Initiated Atom Transfer Radical Polymerization. *Polym. J.*, 37:767–775, 2005.

[32] R. Tadmor, J. Janik, J. Klein, and L. J. Fetters. Sliding Friction with Polymer Brushes. *Phys. Rev. Lett.*, 91:115503, 2003.

[33] W. J. Brittain and S. Minko. A Structural Definition of Polymer Brushes. *J. Polym. Sci., Part A: Polym. Chem.*, 45:3505–3512, 2007.

[34] S. T. Milner. Polymer Brushes. *Science*, 251:905–914, 1991.

[35] P. Krys and K. Matyjaszewski. Kinetics of Atom Transfer Radical Polymerization. *Eur. Polym. J.*, 89:482–523, 2017.

[36] S. Minko. *Polymer Surfaces and Interfaces*, chapter Grafting on Solid Surfaces: "Grafting to" and "Grafting from" Methods, pages 215–235. Springer, Berlin Heidelberg, 2008.

[37] X. Gao, W. Feng, S. Zhu, H. Sheardown, and J. L. Brash. Kinetic Modeling of Surface-Initiated Atom Transfer Radical Polymerization. *Macromol. React. Eng.*, 4:235–250, 2010.

[38] S. Alexander. Adsorption of Chain Molecules with a Polar Head. A Scaling Description. *Le Journal de Physique*, 38:983–987, 1977.

[39] P. G. de Gennes. Conformation of Polymers Attached to an Interface. *Macromolecules*, 13:1069–1075, 1980.

[40] K. Binder. Scaling Concepts for Polymer Brushes and their Test with Computer Simulations. *The European Physical Journal E*, 9:293–298, 2002.

[41] K. Binder and A. Milchev. Polymer Brushes on Flat and Curved Surfaces: How Computer Simulations Can Help to Test Theories and to Interpret Experiments. *Journal of Polymer Science - Polymer Physics*, 50:1515–1555, 2012.

[42] S. T. Milner, T. A. Witten, and M. E. Cates. Theory of the Grafted Polymer Brush. *Macromolecules*, 21(8):2610–2619, 1988.

[43] S. T. Milner, T. A. Witten, and M. E. Cates. A Parabolic Density Profile for Grafted Polymers. *Europhys. Lett.*, 5:413–418, 1988.

[44] A. N. Semenov, J. Bonet-Avalos, A. Johner, and J. F. Joanny. Adsorption of Polymer Solutions onto a Flat Surface. *Macromolecules*, 29:2179–2196, 1996.

[45] Y. Rabin and S. Alexander. Stretching of Grafted Polymer Layers. *Europhys. Lett.*, 13:49–54, 1990.

[46] J. Wittmer, A. Johner, J. F. Joanny, and K. Binder. Chain Desorption from a Semidilute Polymer Brush: A Monte Carlo Simulation. *The Journal of Chemical Physics*, 101:4379–4390, 1994.

[47] G. He, H. Merlitz, J. Sommer, and C. Wu. Static and Dynamic Properties of Polymer Brushes at Moderate and High Grafting Densities: A Molecular Dynamics Study. *Macromolecules*, 40:6721–6730, 2007.

[48] T. Kreer, S. Metzger, M. Müller, K. Binder, and J. Baschnagel. Static Properties of End-Tethered Polymers in Good Solution: A Comparison between Different Models. *The Journal of Chemical Physics*, 120:4012–4023, 2004.

[49] P. Lai and K. Binder. Structure and Dynamics of Grafted Polymer Layers:A Monte Carlo Simulation. *J. Chem. Phys.*, 95:9288–9299, 1991.

[50] I. Coluzza and J. Hansen. Transition from Highly to Fully Stretched Polymer Brushes in Good Solvent. *Phys. Rev. Lett.*, 100:016104, 2008.

[51] D. L. Price and K. Sköld. *Neutron Scattering*, volume 23 of *Methods of Experimental Physics*, chapter Introduction to Neutron Scattering, pages 1–97. Academic Press, Orlando, 1986.

[52] D. S. Sivia. *Elementary Scattering Theory*. Oxford University Press, 2011.

[53] M. U. Witt, S. Hinrichs, N. Möller, S. Backes, B. Fischer, and R. von Klitzing. Distribution of $CoFe_2O_4$ Nanoparticles Inside PNIPAM-Based Microgels of Different Cross-Linker Distributions. *The Journal of Physical Chemistry B*, 123:2405–2413, 2019.

[54] `https://www.ossila.com/pages/spin-coating`, 02.01.2021.

[55] S. Christau, T. Möller, J. Genzer, R. Koehler, and R. von Klitzing. Salt-Induced Aggregation of Negatively Charged Gold Nanoparticles Confined in a Polymer Brush Matrix. *Macromolecules*, 50:7333–7343, 2017.

[56] S. Christau, T. Möller, Z. Yenice, J. Genzer, and R. von Klitzing. Brush/Gold Nanoparticle Hybrids: Effect of Grafting Density on the Particle Uptake and Distribution within Weak Polyelectrolyte Brushes. *Langmuir*, 30:13033–13041, 2014.

[57] R. R. Patil, S. Turhman-Cohen, J. Srogl, D. Kiserow, and J. Genzer. On-Demand Degrafting and the Study of Molecular Weight and Grafting Density of Poly(methyl methacrylate) Brushes of Flat Silica Substrates. *Langmuir*, 31:2372–2381, 2015.

[58] R. R. Patil, S. Turgman-Cohen, J. Srogl, D. Kiserow, and J. Genzer. Direct Measurement of Molecular Weight and Grafting Density by Controlled and Quantitative Degrafting of Surface-Anchored Poly(methyl methacrylate). *ACS Macro Lett.*, 4:251–254, 2015.

[59] B. J. Berne and R. Pecora. *Dynamic Light Scattering: With Applications to Chemistry, Biology, and Physics*. Dover Publications, Mineola, 2000.

[60] S. Bhattacharjee. DLS and Zeta Potential - What They are and What They are not? *J. Controlled Release*, 235:337–351, 2016.

[61] C. Bellmann, A. Caspari, C. Moitzi, and F. Babick, editors. *Dynamische und Elektrophoretische Lichtstreuung*, volume 1. Anton Paar GmbH, Österreich, 2018.

[62] S. Park and M. Seo, editors. *Interface Science and Composites*, volume 18 of *Interface Science and Technology*, chapter Chapter 1 - Intermolecular Forces, pages 1–57. Elsevier, Oxford, 2011.

[63] P. Eaton and P. West. *Atomic Force Microscopy*. Oxford University Press, Great Clarendon Street, Oxford, 2010.

[64] S. Benaglia, V. G. Gisbert, A. P. Perrino, C. A. Amo, and R. Garcia. Fast and High-Resolution Mapping of Elastic Properties of Biomolecules and Polymers with Bimodal AFM. *Nat. Protoc.*, 13:2890–2907, 2018.

[65] D. Hu, A. J. Rosenberg, H. Chouaib, N. Malkova, and Z. Tan. Tracking the Defects and the Band Gap of Ultra-Thin HfO_2 Using a Multi-Oscillator Coby Lorentz Model. *Proceedings of SPIE*, 10585:1, 2018.

[66] H. G. Tompkins and E. A. Irene, editors. *Handbook of Ellipsometry*, volume 30. William Andrew Publishing, Norwich, NY, 2005.

[67] H. Fujiwara. *Spectroscopic Ellipsometry*. Wiley, Hoboken, NJ, 2007.

[68] M. Morita, T. Ohmi, E. Hasegawa, and M. Ohwada. Growth of Native Oxide on a Silicon Surface. *Journal of Applied Physics*, 68:1272–1281, 1990.

[69] `https://refractiveindex.info/`, 24.01.2021.

[70] *38th IFF Spring School - Probing the Nanoworld*. Forschungszentrum Jülich, 2007.

[71] M. Shibayama. Spatial Inhomogeneities and Dynamic Fluctuations of Polymer Gels. *Macromol. Chem. Phys.*, 199:1–30, 1998.

[72] J. Als-Nielsen, D. Jacquemain, K. Kjaer, F. Leveiller, M. Lahav, and L. Leiserowitz. Principles and Applications of Grazing Incidence X-ray and Neutron Scattering from Ordered Molecular Monolayers at the Air-Water Interface. *Phys. Rep.*, 246:251–313, 1994.

[73] H. Schnablegger and Y. Singh. The SAXS Guide - Getting Acquainted with the Principles. Anton Paar GmbH, Austria.

[74] T. Imae, T. Kanaya, M. Furusaka, and N. Torikai, editors. *Neutrons in Soft Matter*. John Wiley & Sons, Hoboken, NJ, 2011.

[75] J. Daillant and A. Gibaud, editors. *X-ray and Neutron Reflectivity*. Number 770 in Lecture Notes in Physics. Springer-Verlag, Berlin Heidelberg, 2009.

[76] A. Gibaud and G. Vignaud. *X-ray and Neutron Reflectivity*, chapter Specular Reflectivity from Smooth and Rough Surfaces, pages 85–133. Number 770 in Lecture Notes in Physics. Springer, Berlin, Heidelberg, 2009.

[77] C. Fermon, F. Ott, and A. Menelle. *X-ray and Neutron Reflectivity*, chapter Neutron Reflectometry, pages 183–235. Number 770 in Lecture Notes in Physics. Springer, Berlin, Heidelberg, 2009.

[78] M. Brugnoni, A. C. Nickel, L. C. Kröger, A. Scotti, A. Pich, K. Leonhard, and W. Richtering. Synthesis and Structure of Deuterated Ultra-Low Cross-Linked Poly(*N*-isopropylacrylamide Microgels. *Polym. Chem.*, 10:2397–2405, 2019.

[79] B. Ewen and D. Richter. Neutron Spin Echo Spectroscopy Viscoelaticity Rheology. volume 134 of *Advances in Polymer Science*, pages 3–129. Springer-Verlag Berlin Heidelberg NewYork, 1997.

[80] D. Richter, M. Monkenbusch, A. Arbe, and J. Colmenero. *Neutron Spin Echo in Polymer Systems*, volume 174 of *Advances in Polymer Science*. Springer Verlag, Berlin Heidelberg New York, 2005.

[81] S. Pasini, O. Holderer, T. Kozielewski, D. Richter, and M. Monkenbusch. J-NSE-Phoenix, a Neutron Spin-Echo Spectrometer with Optimized Superconducting Precession Coils at the MLZ in Garching. *Rev. Sci. Instrum.*, 90:043107, 2019.

[82] O. Holderer and O. Ivanova. J-NSE: Neutron Spin Echo Spectrometer. *Journal of Large-Scale Research Facilities*, 1:1–4, 2015.

[83] O. Holderer, P. Zolnierczuk, S. Pasini, L. Stingaciu, and M. Monkenbusch. A Better View Through New Glasses: Developments at the Jülich Neutron Spin Echo Spectrometers. *Physica B: Condensed Matter*, 562:9–12, 2019.

[84] P. Müller-Buschbaum. Grazing Incidence Small-Angle Neutron Scattering: Challenges and Possibilities. *Polym. J.*, 45:34–42, 2013.

[85] P. Müller-Buschbaum. GISAXS and GISANS as Metrology Technique for Understanding the 3D Morphology of Block Copolymer Thin Films. *Eur. Polym. J.*, 81:470–493, 2016.

[86] S. Wellert, J. Hübner, D. Boyaciyan, O. Ivanova, R. von Klitzing, O. Soltwedel, and O. Holderer. A Grazing Incidence Neutron Spin Echo Study of Near Surface Dynamics in P(MEO_2MA-*co*-OEGMA) Copolymer Brushes. *Colloid Polym. Sci.*, 296:2005–2014, 2018.

[87] K. Gawlitza, O. Ivanova, A. Radulescu, O. Holderer, R. von Klitzing, and S. Wellert. Bulk Phase and Surface Dynamics of PEG Microgel Particles. *Macromolecules*, 48:5807–5815, 2015.

[88] H. Frielinghaus, M. Gvaramia, G. Mangiapia, S. Jaksch, M. Ganeva, A. Koutsioubas, S. Mattauch, M. Ohl, M. Monkenbusch, and O. Holderer. New Tools for Grazing Incidence Neutron Scattering Experiments Open Perspectives to Study Nano-Scale Tribology Mechanisms. *Nuclear Inst. and Methods in Physics Research, A*, 871:72–76, 2017.

[89] O. Holderer, H. Frielinghaus, S. Wellert, F. Lipfert, M. Monkenbusch, R. von Klitzing, and D. Richter. Grazing Incidence Neutron Spin Echo Spectroscopy: Instrumentation Aspects and Scientific Opportunities. *J. Phys. Conf. Ser.*, 528:012025, 2014.

[90] G. Pospelov, W. van Herck, J. Burle, J. M. Carmona Loaiza, C. Durniak, J.M. Fisher, M. Ganeva, D. Yurov, and J. Wuttke. BornAgain: Software for Simulating and Fitting Grazing-Incidence Small-Angle Scattering. *Journal of Applied Chrystallography*, 53:262–276, 2020.

[91] K. Gawlitza, R. Georgieva, N. Tavraz, J. Keller, and R. von Klitzing. Immobilization of Water-Soluble HRP within Poly-*N*-isopropylacrylamide Microgel Particles for Use in Organic Media. *Langmuir*, 29:16002–16009, 2013.

[92] M. Karg, S. Prévost, A. Brandt, D. Wallacher, R. von Klitzing, and T. Hellweg. Poly-NIPAM Microgels with Different Cross-Linker Densities. *Prog. Colloid Polym. Sci.*, 140:63–76, 2013.

[93] T. Hellweg, K. Kratz, S. Pouget, and W. Eimer. Internal Dynamics in Colloidal PNIPAM Microgel Particles Immobilised in Mesoscopic Crystals. *Colloids Surf., A*, 202(2-3):223–232, 2002.

[94] T. Tanaka and D. J. Fillmore. Kinetics of Swelling of Gels. *The Journal of Chemical Physics*, 70:1214–1218, 1979.

[95] K. Kratz, T. Hellweg, and W. Eimer. Structural Changes in PNIPAM Microgel Particles as Seen by SANS, DLS, and EM Techniques. *Polymer*, 42:6631–6639, 2001.

[96] A. Burmistrova, M. Richter, C. Uzum, and R. von Klitzing. Effect of Cross-Linker Density of P(NIPAM-*co*-AAc) Microgels at Solid Surfaces on the Swelling/Shrinking Behaviour and the Young's Modulus. *Colloid Polym. Sci.*, 289:613–624, 2011.

[97] K. Uhlig, T. Wegener, Y. Hertle, J. Bookhold, M. Jaeger, T. Hellweg, A. Fery, and C. Duschl. Thermoresponsive Microgel Coatings as Versatile Functional Compounds for Novel Cell Manipulation Tools. *Polymers*, 10:656, 2018.

[98] G. E. Morris, B. Vincent, and M. J. Snowden. The Interaction of Thermosensitive, Anionic Microgels with Metal Ion Solution Species. In *Progress in Colloid & Polymer Science*, volume 105, pages 16–22. Springer, 2007.

[99] Z. Chen, L. Xu, Y. Liang, and M. Zhao. pH-Sensitive Water-Soluble Nanospheric Imprinted Hydrogels Prepared as Horseradish Peroxidase Mimetic Enzymes. *Adv. Mater.*, 22:1488–1492, 2010.

[100] A. S. Caldwell, B. A. Aguadi, and K. S. Anseth. Designing Microgels for Cell Culture and Controlled Assembly of Tissue Microenvironments. *Adv. Funct. Mater.*, 30:1–15, 2020.

[101] Z. Gu, T. T. Dang, M. Ma, B. C. Tang, H. Cheng, S. Jiang, Y. Dong, Y. Zhang, and D. G. Anderson. Glucose-Responsive Microgels Integrated with Enzyme Nanocapsules for Closed-Loop Insulin Delivery. *ACS Nano*, 7:2758–6766, 2013.

[102] J. Thorne, G. Vine, and M. Snowden. Microgel Appliactions and Commercial Considerations. *Colloid Polym. Sci.*, 289:625–646, 2011.

[103] M. Reufer, P. Díaz-Leyva, L. Lynch, and F. Scheffold. Temperature-Sensitive Poly(*N*-isopropyl-acrylamide) Microgel Particles: A Light Scattering Study. *The European Physical Journal E*, 28:165–171, 2009.

[104] S. Bergmann, O. Wrede, T. Huser, and T. Hellweg. Super-Resolution Optical Microscopy Resolves Network Morphology of Smart Colloidal Microgels. *Phys. Chem. Chem. Phys.*, 20:5974–5083, 2018.

[105] G. M. Conley, S. Nöjd, M. Braibanti, and P. Schurtenberger. Superresolution Microscopy of the Volume Phase Transition of PNIPAM Microgels. *Colloids Surf., A*, 2016.

[106] E. Mueller, R. J. Alsop, A. Scotti, M. Bleuel, M. C. Rheinstädter, W. Richtering, and T. Hoare. Dynamically Cross-Linked Self-Assembled Thermoresponsive Microgels with Homogeneous Internal Structures. *Langmuir*, 34:1601–1612, 2018.

[107] C. Scherzinger, O. Holderer, D. Richter, and W. Richtering. Polymer Dynamics in Responsive Microgels: Influence of Cononsolvency and Microgel Architecture. *Phys. Chem. Chem. Phys.*, 14:2762–2768, 2012.

[108] S. Maccarrone, C. Scherzinger, O. Holderer, P. Lindner, M. Sharp, W. Richtering, and D. Richter. Cononsolveny Effects on the Structure and Dynamics of Microgels. *Macromolecules*, 47:5982–5988, 2014.

[109] S. Maccarrone, A. Ghavami, O. Holderer, C. Scherzinger, P. Lindner, W. Richtering, D. Richter, and R. G. Winkler. Dynamic Structure Factor of Core-Shell Microgels: A Neutron Scattering and Mesoscale Hydrodynamic Simultion Study. *Macromolecules*, 49:3608–3618, 2016.

[110] T. Kyrey, J. Witte, A. Feoktystov, V. Pipich, B. Wu, S. Pasini, A. Radulescu, M. U. Witt, M. Kruteva, R. von Klitzing, S. Wellert, and O. Holderer. Inner

Structure and Dynamics of Microgels with Low and Medium Crosslinker Content Prepared *via* Surfactant-Free Precipitaion Polymerization and Continuous Monomer Feeding Approach. *Soft Matter*, 15:6536–6546, 2019.

[111] B. Hammouda, D. L. Ho, and S. Kline. Insight into Clustering in Poly (ethylene oxide) Solutions. *Macromolecules*, 37(18):6932–6937, 2004.

[112] M. Shibayama, K. Kawakubo, and T. Norisuye. Comparison of the Experimental and Theoretical Structure Factors of Temperature Sensitive Polymer Gels. *Macromolecules*, 31:1608–1614, 1998.

[113] B. Hammouda. A New Guinier-Porod Model. *J. Appl. Crystallogr.*, 43:716–719, 2010.

[114] P. Wong. Scattering by Inhomogeneous Systems with Rough Internal Surfaces: Porous Solids and Random-Field Ising Systems. *Phys. Rev. B*, 32:7417–7424, 1985.

[115] A. J. Howe, A. M. Howe, and A. F. Routh. The Viscosity of Dilute Poly(*N*-isopropylacrylamide) Dispersions. *J. Colloid Interface Sci.*, 357:300–307, 2011.

[116] N. Boon and P. Schurtenberger. Swelling of Micro-Hydrogels with a Crosslinker Gradient. *Phys. Chem. Chem. Phys.*, 19:23740–23746, 2017.

[117] D. Kunz, A. Thurn, and W. Burchard. Dynamic Light Scattering from Spherical Particles. *Colloid & Polymer Science*, 261:635–644, 1983.

[118] S. Schmidt, M. Zeiser, T. Hellweg, C. Duschl, A. Fery, and H. Möhwald. Adhesion and Mechanical Properties of PNIPAM Microgel Films and their Potential Use as Switchable Cell Culture Substrates. *Adv. Funct. Mater.*, 20:3235–3243, 2010.

[119] L. Pérez-Fuentes, C. Drummond, J. Faraudo, and D. Bastos-González. Anions Make the Difference: Insights from the Interaction of Big Cations and Anions with Poly (*N*-isopropylacrylamide) Chains and Microgels. *Soft Matter*, 11:5077–5086, 2015.

[120] R. Saha and W. D. Nix. Effects of the Substrate on the Determination of Thin Film Mechanical Properties by Nanoindentation. *Acta Mater.*, 50:23–38, 2002.

[121] J. Witte, T. Kyrey, J. Lutzki, A. M. Dahl, J. Houston, A. Radulescu, V. Pipich, L. Stingaciu, M. Kühnhammer, M. U. Witt, R. von Klitzing, O. Holderer, and S. Wellert. A Comparison of the Network Structure and Inner Dynamics of Homogeneously and Heterogeneously Crosslinked PNIPAM Microgels with High Crosslinker Content. *Soft Matter*, 15:1053–1064, 2019.

[122] A. Aufderhorst-Roberts, D. Baker, R. J. Foster, O. Cayre, J. Mattsson, and S. D. Connell. Nanoscale Mechanics of Microgel Particles. *Nanoscale*, 10:16050–16061, 2018.

[123] S. Matsui, T. Kureha, S. Hiroshige, M. Shibata, T. Uchihashi, and D. Suzuki. Fast Adsorption of Soft Hydrogel Microspheres on Solid Surfaces in Aqueous Solution. *Angew. Chem. Int. Ed.*, 56:12146–12149, 2017.

[124] P. G. de Gennes. Scaling Theory of Polymer Adsorption. *J. Phys.*, 37:1445–1452, 1976.

[125] S. Alexander. Polymer Adsorption on Small Spheres. A Scaling Approach. *J. Phys.*, 38:977–981, 1977.

[126] S. T. Milner, T. A. Witten, and M. E. Cates. Effects of Polydispersity in the End-Grafted Polymer Brush. *Macromoleculues*, 22:853–861, 1989.

[127] G. Fytas, S. H. Anastasiadis, R. Seghrouchnie, D. Vlassopoulos, J. Li, B. J. Factor, W. Theobald, and C. Toprakcioglu. Probing Collective Motions of Terminally Anchored Polymers. *Science*, 274:2041–2044, 1996.

[128] B. Farago, M. Monkenbusch, D. Richter, J. S. Huang, L. J. Fetters, and A. P. Gast. Collective Dynamics of Tethered Chains: Breathing Modes. *Phys. Rev. Lett.*, 71:1015, 1993.

[129] J. Pyun, T. Kowalewski, and K. Matyjaszewski. Synthesis of Polymer Brushes Using Atom Transfer Radical Polymerization. *Macromol. Rapid Commun.*, 24:1043–1059, 2003.

[130] D. M. Jones, A. A. Brown, and W. T. S. Huck. Surface-Initiated Polymerizations in Aqueous Media: Effect of Initiator Density. *Langmuir*, 18:1265–1269, 2002.

[131] K. N. Plunkett, X. Zhu, J. S. Moore, and D. E. Leckband. PNIPAM Chain Collapse Depends on the Molecular Weight and Grafting Density. *Langmuir*, 22:4259–4266, 2006.

[132] Y. Zou, J. N. Kizhakkedathu, and D. E. Brooks. Surface Modification of Polyvinyl Chloride Sheets via Growth of Hydrophilic Polymer Brushes. *Macromolecules*, 42:3258–3268, 2009.

[133] V. N. Michailidou, B. Loppinet, O. Prucker, J. Rühe, and G. Fytas. Cooperativ Diffusion of End-Grafted Polymer Brushes in Good Solvents. *Macromolecules*, 38:8960–8962, 2005.

[134] G. E. Yakubov, B. Loppinet, H. Zhang, J. Rühe, R. Sigel, and G. Fytas. Collective Dynamics of an End-Grafted Polymer Brush in Solvent of Varying Quality. *Phys. Rev. Lett.*, 92:115501, 2004.

[135] Y. Yu, B. D. Kieviet, F. Liu, I. Siretanu, E. Kutnyánszyk, G. J. Vansco, and S. de Beer. Stretching of Collapsed Polymers Causes an Enhanced Dissipative Response of PNIPAM Brushes Near their LCST. *Soft Matter*, 11:8508–8516, 2015.

[136] L. Michalek, L. Barner, and C. Barner-Kowollik. Polymer on Top: Current Limits and Future Perspectives of Quantitatively Evaluating Surface Grafting. *Adv. Mater.*, 30:1706321, 2018.

[137] A. Halperin. *Soft Order in Physical Systems*, chapter On Polymer Brushes and Blobology: An Introduction, pages 33–56. Plenum Press, New York, 1994.

[138] P. Holmqvist, J. K. H. Dhont, and P. R. Lang. Colloidal Dynamics Near a Wall Studied by Evanescent Wave Light Scattering: Experimental and Theoretical Improvements and Methodological Limitations. *J. Chem. Phys.*, 126:044707, 2007.

[139] V. Michailidou, G. Petekidis, J. Swan, and J. F. Brady. Dynamics of Concentrated Hard-Sphere Colloids Near a Wall. *Phys. Rev. Lett.*, 102:1–4, 2009.

[140] M. Tolan, T. Seydel, A. Madsen, G. Grübel, W. Press, and S. K. Sinha. Investigation of Surface Dynamics on Micro- and Nanometer Scales. *Appl. Surf. Sci.*, 182:236–243, 2001.

[141] L. Sun, B. Akgun, S. Narayanan, Z. Jiang, and M. D. Foster. Surface Fluctuations of Polymer Brushes Swollen in Good Solvent Vapor. *Macromolecules*, 49:7308–7313, 2016.

[142] T. Koga, C. Li, M. K. Endoh, J. Koo, M. Rafailovich, S. Narayanna, D. R. Lee, L. B. Lurio, and S. K. Sinha. Reduced Viscosity of the Free Surface in Entangled Polymer Melt Films. *Phys. Rev. Lett.*, 104:066101, 2010.

[143] E. S. Kooij, X. Sui, M. A. Hempenius, H. J. W. Zandvliet, and G. J. Vansco. Probing the Thermal Collapse of Poly(*N*-isopropylacrylamide) Grafts by Quantitative *in Situ* Ellipsometry. *J. Phys. Chem. B*, 116:9261–9268, 2012.

[144] R. Descas, J. Sommer, and A. Blumen. Grafted Polymer Chains Interacting with Substrates: Computer Simulations and Scaling. *Macromol. Theory Simul.*, 17:429–453, 2008.

[145] G. Longhi, F. Lebon S. Abbate, and S. L. Fornili. Molecular Dynamics Simulations of a Model Oligomer for Poly(*N*-isopropylacrylamide) in Water. *Chem. Phys. Lett.*, 386:123–127, 2004.

Appendix A.

Additional Information

Surfactant-free Precipitation Polymerization

Table A.1.: Recipe for the surfactant-free precipitation polymerization of PNIPAM batch- and feeding microgels.

Sample	c_{NIPAM}**[mM]**	c_{BIS}**[mM]**	c_{BIS}**[mol%]**	c_{AAPH}**[mM]**	t_p**[min]**
MG_2P	122	2.5	≈ 2.0	2.1	10
MG_5P	119	6.3	≈ 5.0	2.1	10
$MG_{10}P$	112	12.5	≈ 10.0	2.1	10
MG_2F	122	2.5	≈ 2.0	2.1	11.3
MG_5F	119	6.3	≈ 5.0	2.1	11.3
$MG_{10}F$	112	12.5	≈ 10.0	2.1	11.3

Calibration curves for LC-MS

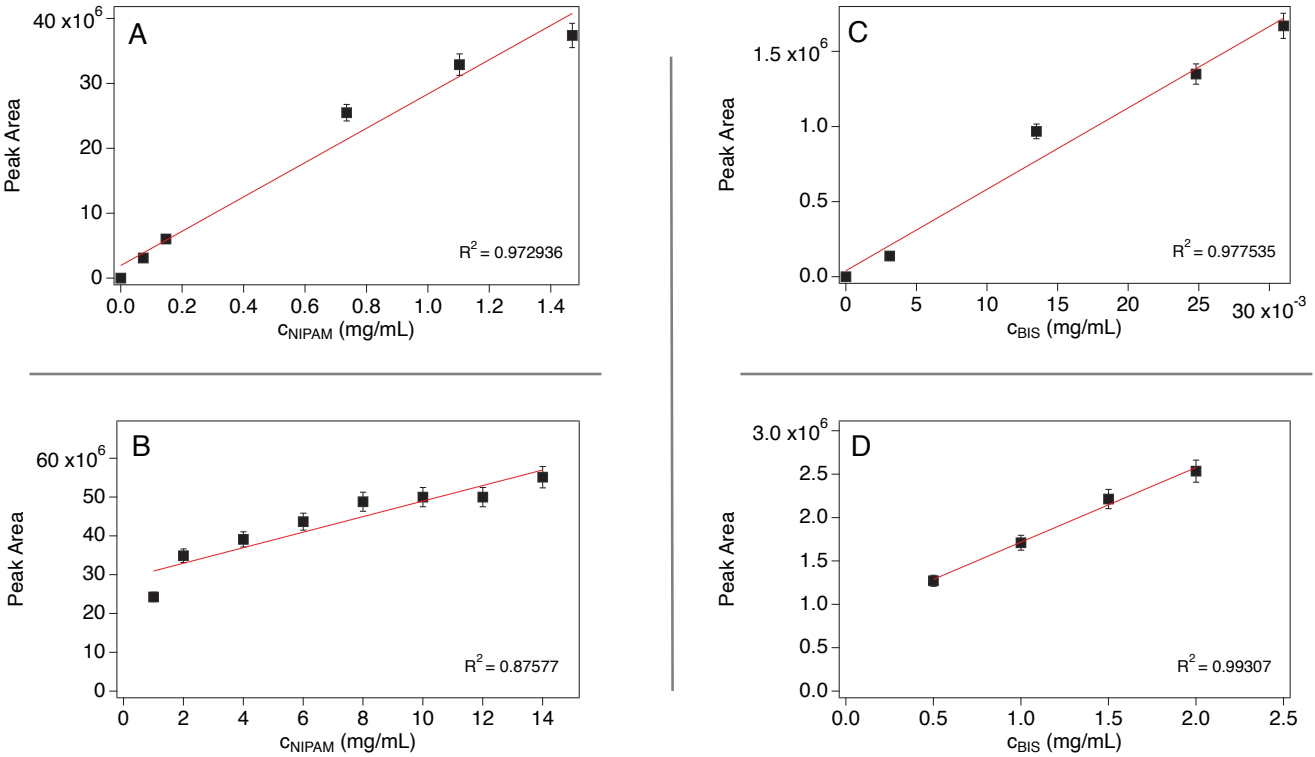

Figure A.1.: Calibration curves for LC-MS measurements of NIPAM and BIS within the concentration ranges relevant for batch and continuous monomer feeding polymerization. The R^2 values indicate varying qualities of the linear fit to the data.

HPLC conditions for LC-MS

HPLC measuring conditions were

- Column: Grom-Sil-120-ODS-4-HE (Grace), length 50 mm, internal diameter 2 mm, 3 μm

Gradient:

- Eluent 1: H_2O + 0.1% HCOOH
- Eluent 2: MeCN + 0.1% HCOOH

- 0 - 10 min: Eluent 2: from 5% to 100%
- 10 - 13 min: Eluent 2: hold 100%
- 13 - 18 min: Eluent 2: hold 5%
- flow: 0.3 mL/min

DAD spectrum scan range 205 - 850 nm; Step 2 nm
UV/Vis Channel:

- Channel A - 215 nm, 4 nm Bandwidth
- Channel B - 280 nm, 40 nm Bandwidth
- Channel C - 350 nm, 100 nm Bandwidth

Zetapotential

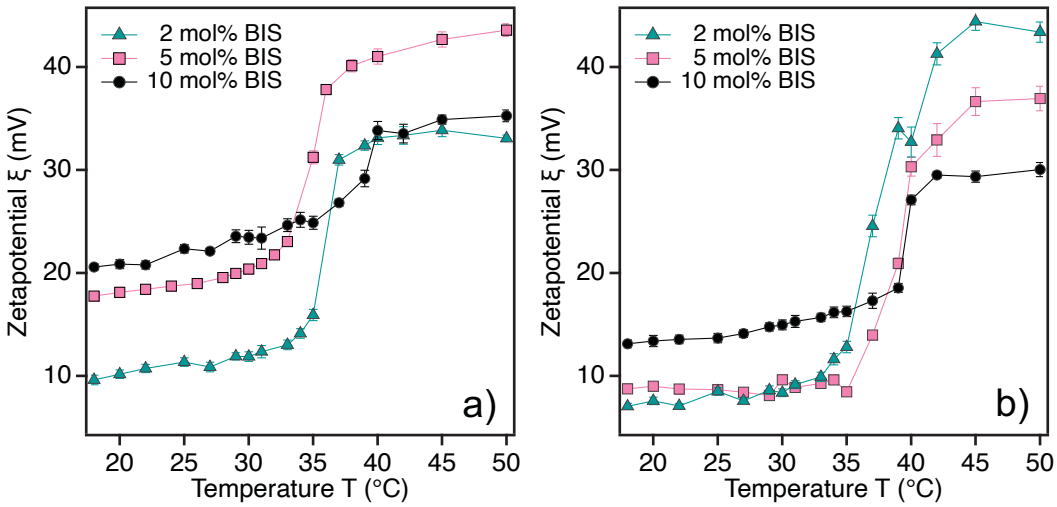

Figure A.2.: Temperature-dependent zetapotential measurements of a) batch- and b) feeding-microgels. The zetapotential increases with increasing temperatures as the positive charge of the initiator comes closer to the interface as the particles collapse.

NSE of MG_5P

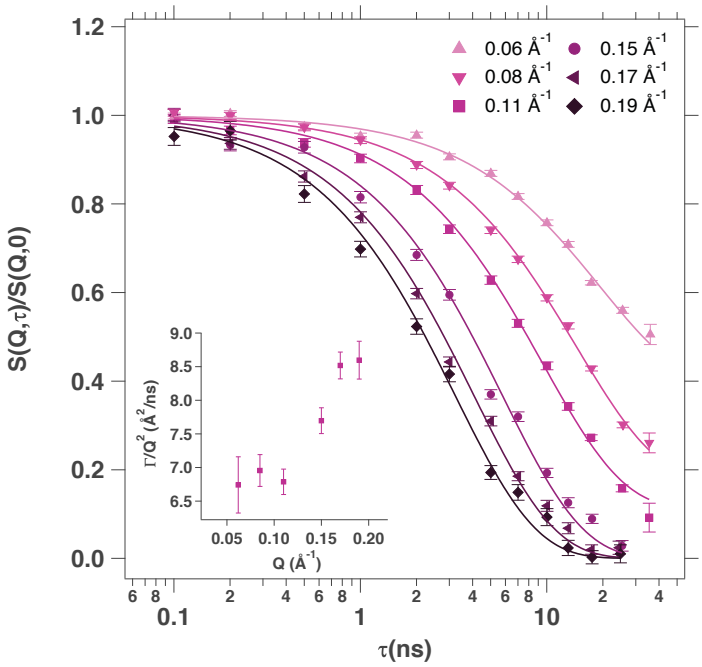

Figure A.3.: Normalized ISFs of MG_5P at different Q-values. The inset shows the Q-dependence of the cooperative diffusion coefficient. The cooperative diffusion coefficient has a constant value between 0.06 and 0.11 Å^{-1}, followed by an increase at higher Qs.

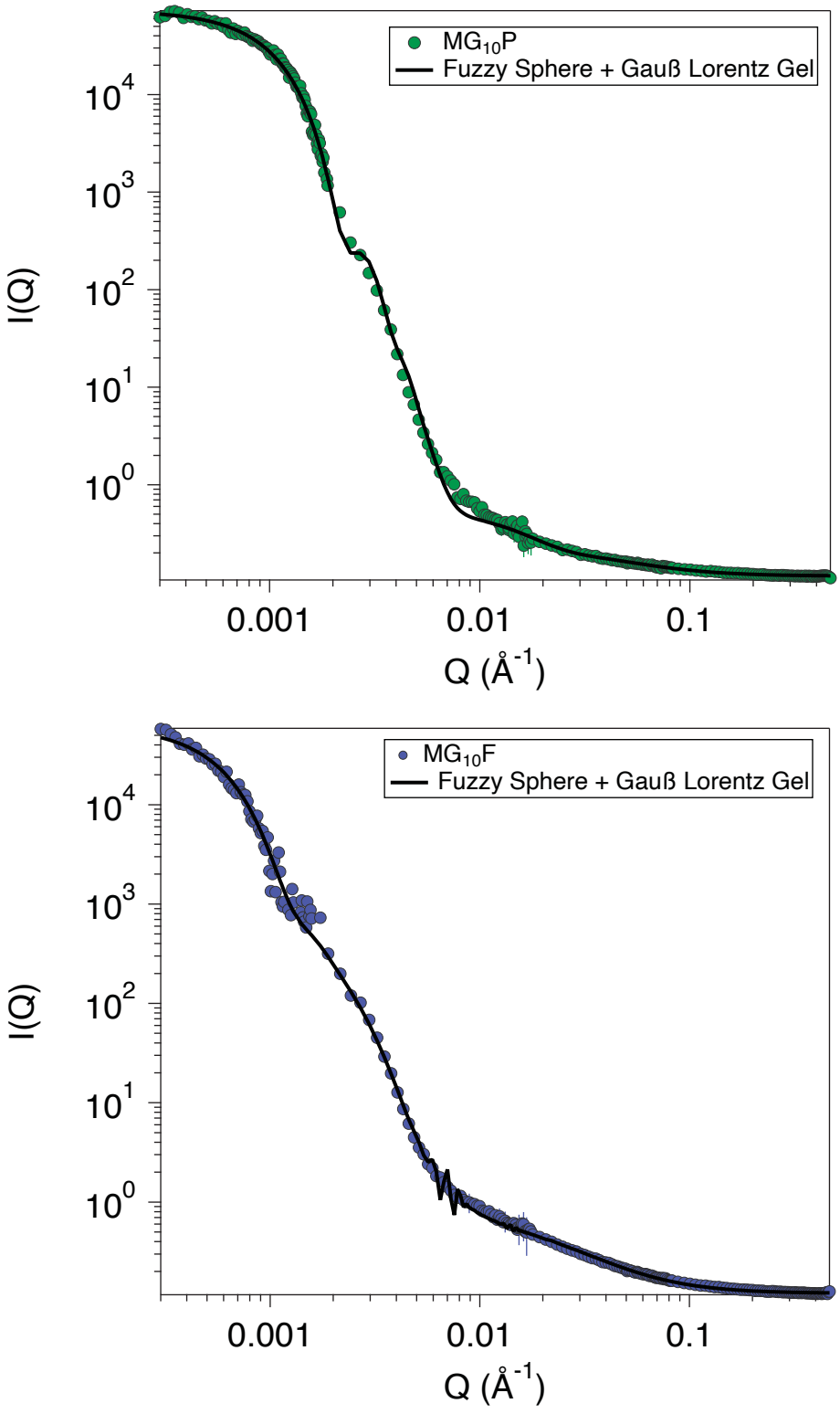

Figure A.4.: SANS data of $MG_{10}P$ and $MG_{10}F$ fit with a combination of the fuzzy sphere model and a model of a Gauss Lorentz Gel.

SANS alternative fits

Neutron Spin Echo

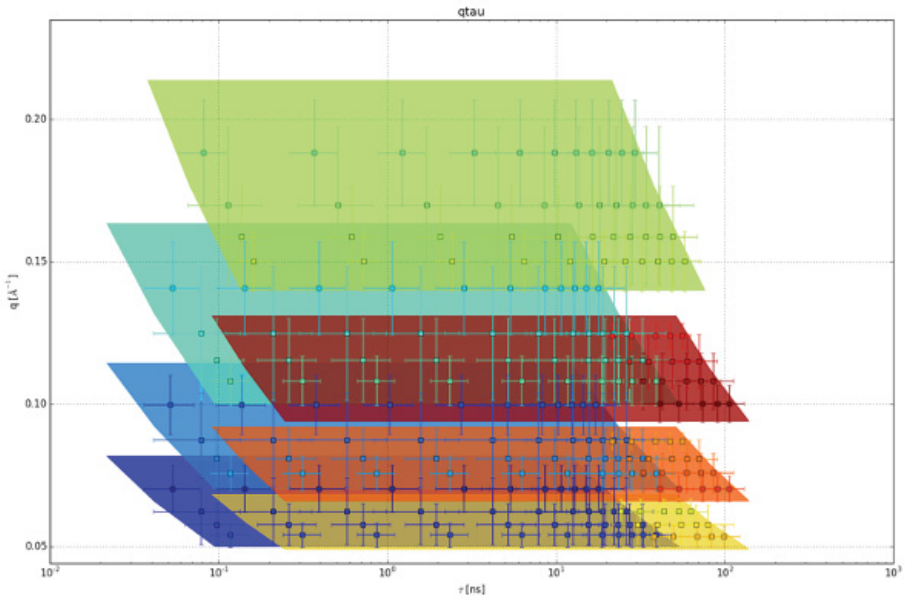

Figure A.5.: Q-τ-map for NSE experiments at the SNS-NSE at Oak Ridge National Laboratory.

Neutron reflectivity alternative fits

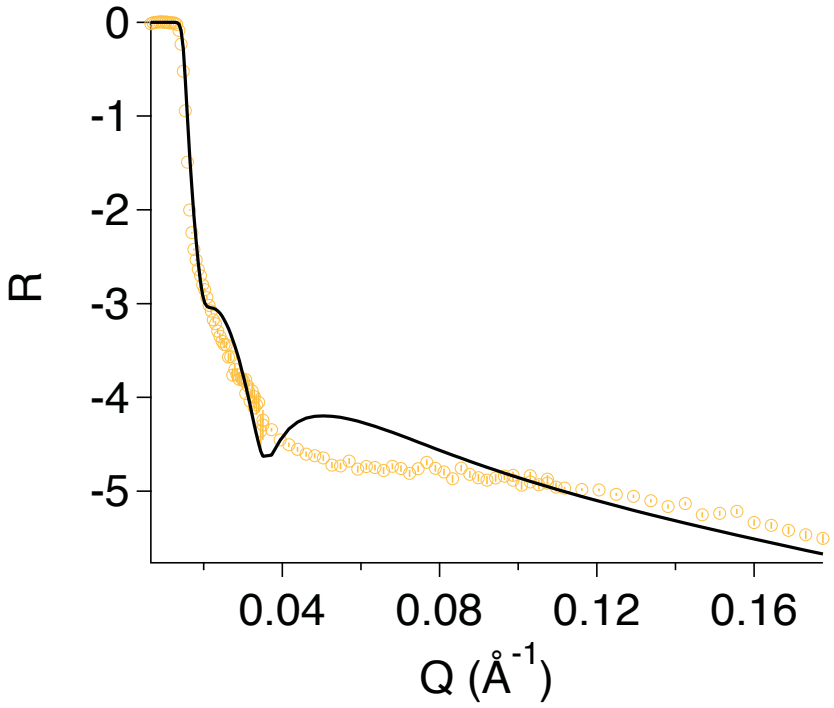

Figure A.6.: Neutron reflectivity curve of the low density brush ($\sigma \approx 0.6\ nm^{-2}$) fit with only one brush layer. The data cannot be described sufficiently well with this fit.

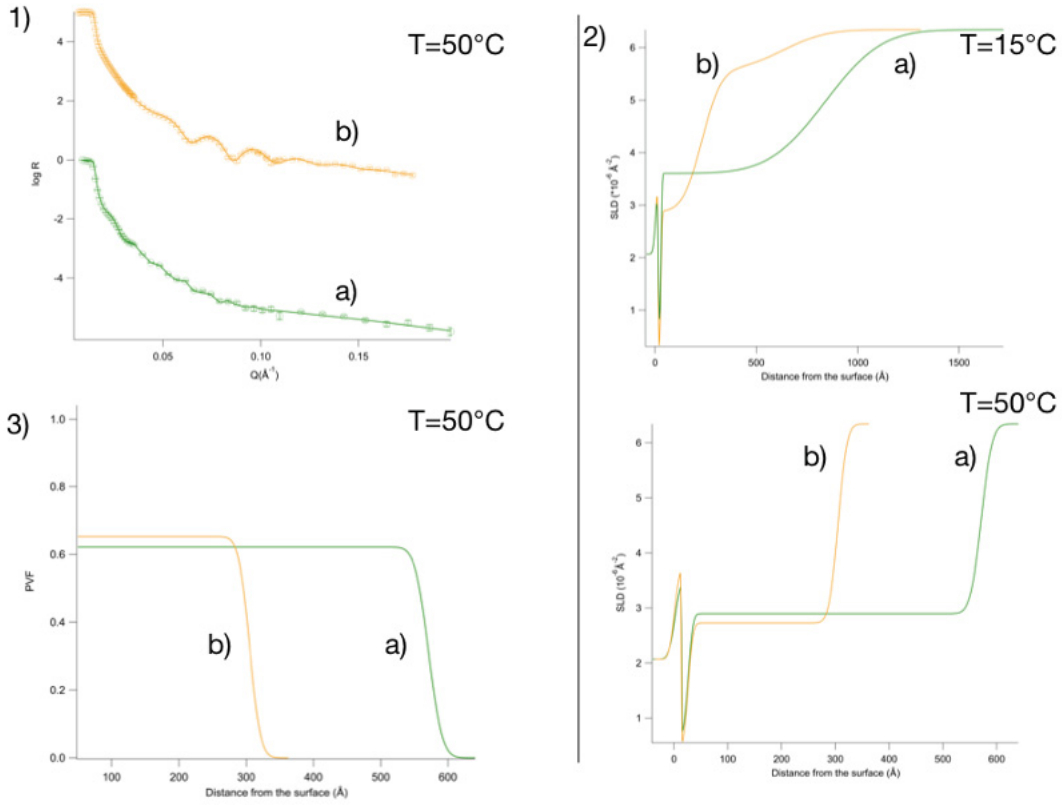

Figure A.7.: 1) Neutron reflectivity curves of a) the high density brush ($\sigma \approx 1.0\ nm^{-2}$) and b) the low density brush ($\sigma \approx 0.6\ nm^{-2}$) at 50 °C. 2) SLD profiles of the brushes at 15 °C and 50 °C. 3) PVF resulting from 1).

SEC elugrams

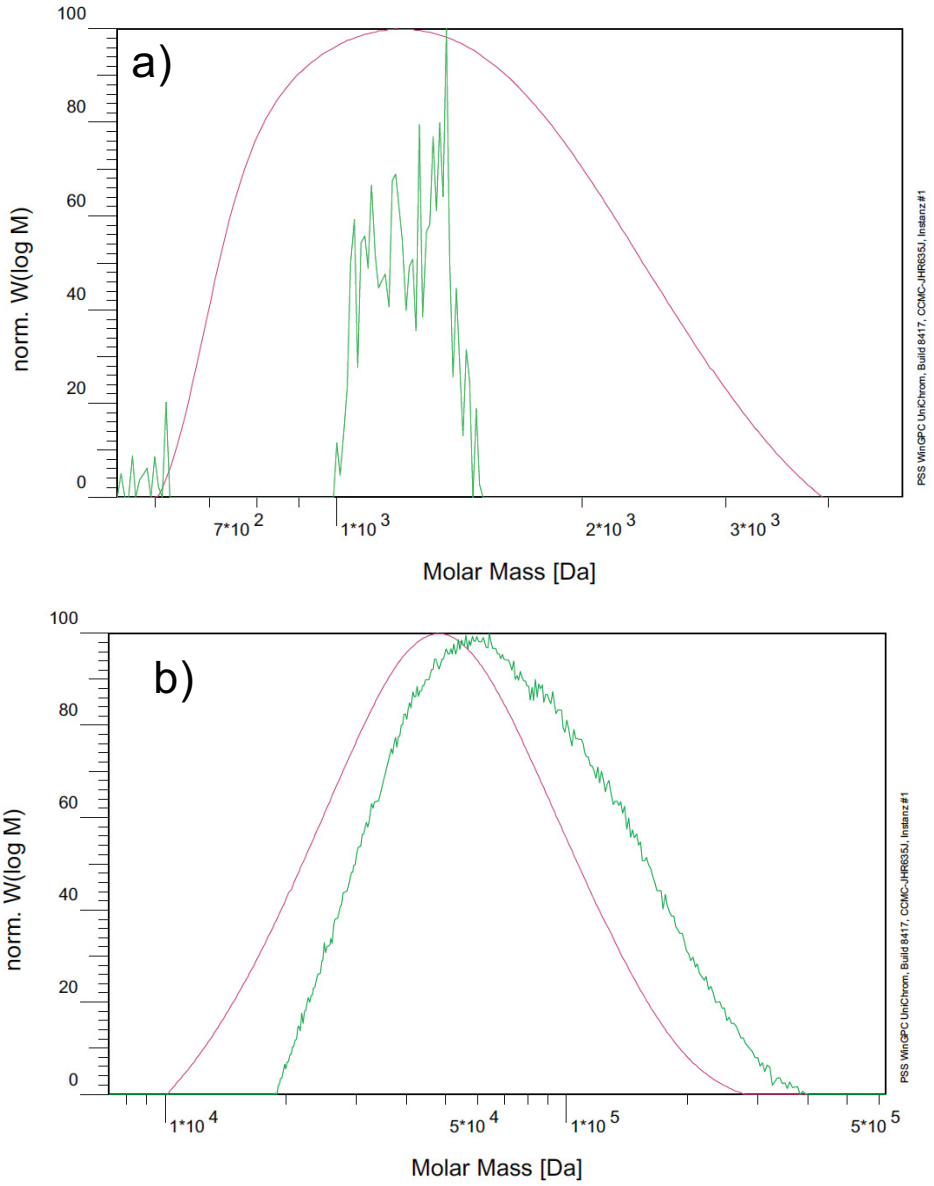

Figure A.8.: SEC eluting peaks for the high grafting density brush ($\sigma \approx 1.0\ nm^{-2}$) measured by RI (green) and UV-detection (pink). a) and b) show that there is a lower and higher molecular mass present in the degrafted brush.

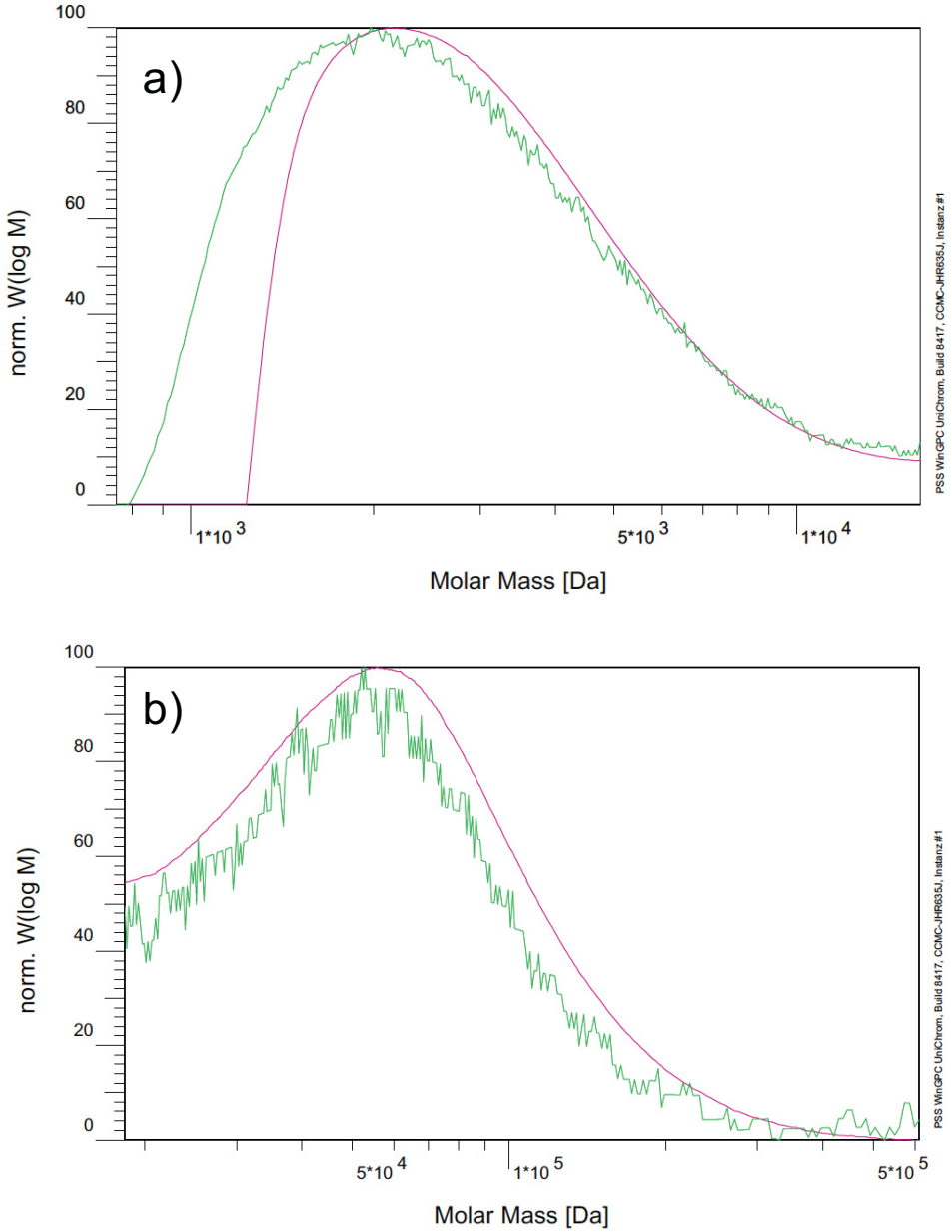

Figure A.9.: SEC eluting peaks for the low grafting density brush ($\sigma \approx 0.6\ nm^{-2}$) measured by RI (green) and UV-detection (pink). a) and b) show that there is a lower and higher molecular mass present in the degrafted brush.

Growth of PNIPAM brushes on Ti-wafers

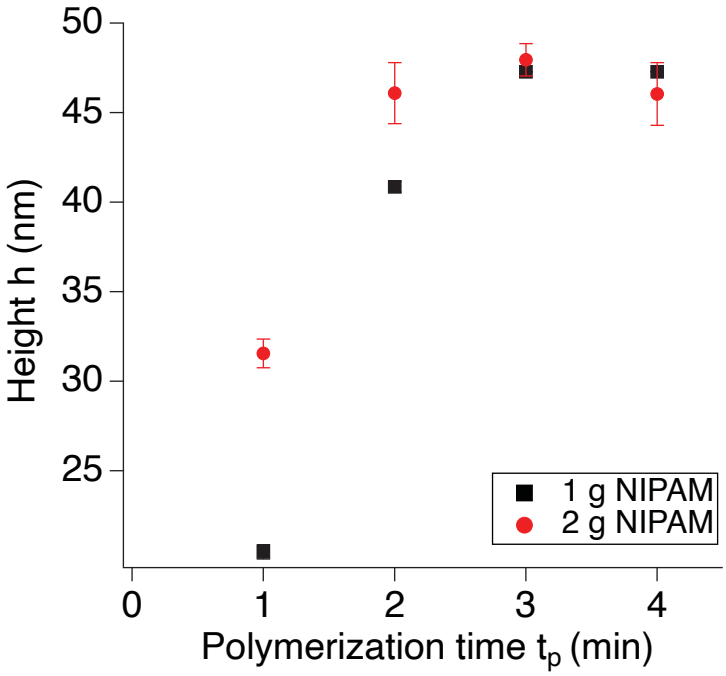

Figure A.10.: Growth of PNIPAM brushes on Ti-coated Si-wafers with different amounts of monomer. The growth appears to be limited to approximately 48 nm.